Charles University in Prague

Faculty of Mathematics and Physics

DOCTORAL THESIS

Petr Čermák

Magnetic properties of $R_2T\mathrm{In}_8$ and related tetragonal compounds

Department of Condensed Matter Physics

Supervisor of the doctoral thesis: doc. Mgr. Pavel Javorský, Dr.

Study programme: Physics
Specialization: 4F3 Physics of Condensed Matter and Materials Research

Prague 2014

The completion of my dissertation and whole Ph.D. study has been a long journey. During these 4 years, I met a lot of true friends and enjoyed a plenty of nice time with them. I started as a young student in Prague, and then due to help of my chiefs, I moved to Grenoble in France. There I had opportunity to work for one year in the most powerful neutron source in the world, 300 m above sea level surrounded by 10 times higher mountains. After this, again with help of a lot of people, I moved closer to my homeland, to Garching in Germany. And now I am not such a young student. I am married to the marvellous woman and we are expecting a baby.

My dissertation has always been a priority, but as most know, there are several priorities in a person’s life at any one time. Unfortunately due to life’s challenges and the changes that followed, my dissertation could not always be the number one priority. At any rate, I have finished, but not alone, and am elated. I could not have succeeded without the invaluable support of a several.

I’d like to begin with Dr. Pavel Javorský from Charles University who was my supervisor since the beginning. His flexibility in scheduling, gentle encouragement and relaxed demeanour made for a good working relationship and the impetus for me to finish. If I look back in time, his support was THE important thing, why I stayed in science and did not left the faculty after my master. Thank you, Pavel.

I am grateful to all members of the Prague SCES group, who participated in a formation of such an inspiring working atmosphere. I especially thank to Prof. Vladimír Sechovský, leader of the group, big organizer and enthusiast. He was able to create something, which was for me unimaginable before 10 years – a scientific university group in Czech Republic, which can fully compete with the best science groups in the world. I also thank to my friends and colleagues: Milan Klicpera, Michal Vališka, Klára Uhlířová, Jirka Pospíšil, Jirka Kaštil, Jirka Prchal, Honza Prokleška and Honza Fikáček for a plenty of valuable discussions and help. Last one who I want to pick up from the whole condensed matter team in Prague is Marie Kratochvílová. She is not only a diligent hard working scientist, but also a great person and always my first choice for having a chat with beer or some mounting trip. Marie was also my big help during my abroad missions, she helped me to manage all university paperwork and she also printed and bound this thesis. Thank you, Marie.

I am grateful to Dr. Martin Diviš who did all first principle calculations and Dr. Alexander Andreev for performing the high field experiments.

I’d also like to give a heartfelt, special thanks to Martin Boehm from ILL. He was not only my Chair during my stay in Grenoble, but my mentor and friend. The second person who made my stay in France possible was Jiří Kulda. He helped me with almost everything: changing to winter tires, drinking good wine and cheeses, filling up the tax declaration... Discussion with Martin and Jiří about instrument development and hidden aspects of spectroscopy were always valuable and energizing. For this, I cannot thank them enough. I am forever grateful. Thank You Martin and Jiří!

I would also like to thank Juan Rodriguez-Carvajal for his assistance and guidance in my understanding of the diffraction and crystallography. He was always able to answer my questions quickly and in understandable form. Especially all problems with FullProf were solved with Juan like a charm. Together with Luis Fuentes-Montero, they taught me how to write clean Fortran code, and how develop software in the team. Thank you, Juan and Luiso!

Additionally, I am very grateful for the friendship of lot of colleagues at ILL, especially Anton, Dario, Diane, Eron, Eva, Giacomo, Ida, Ingo, Paul, Simon, Yuri... And big gratitude is addressed to the director of ILL Andrew Harrison for wonderful skiing time with students.

Next I’d like to thank all the people from PANDA team at MLZ Garching who helped me during my last year. Thanks to Florin Stoica for being a great friend and showing me how to maintain spectrometer. Thanks to Enrico Faulhaber for introducing me Python as a best language for science ever. Thanks Philipp Geselbracht for valuable discussions and comments. Special thanks belong also to Joshua Lim for careful reading of the whole thesis and improving my English.

The biggest thanks are devoted to the head of PANDA team, Astrid Schneidewind. She provided me enough time and space to finish my Ph.D. study as well as always good mood and open atmosphere. Her enthusiasm for friendly team and cooperation among departments are making PANDA instrument special and I am grateful to her for doing it. I also thanks to Astrid’s husband Jörg for plenty of advices regarding our tax declaration.

I thank my parents, Jan and Alena, for their endless support in all my plans and ideas.

Finally, and most importantly, I would like to thank my wife Veronika. Her support, quiet patience and unwavering love were undeniably the bedrock upon which the past seven years of my life have been built. Her tolerance of my occasional bad moods and problems is a testament in itself of her unyielding devotion and love. Thank you Veronika!

I declare that I carried out this doctoral thesis independently, and only with the cited sources, literature and other professional sources.

I understand that my work relates to the rights and obligations under the Act No. 121/2000 Coll., the Copyright Act, as amended, in particular the fact that the Charles University in Prague has the right to conclude a license agreement on the use of this work as a school work pursuant to Section 60 paragraph 1 of the Copyright Act.

In…...... date........... signature

Název práce: Magnetické vlastnosti $R_2T\mathrm{In}_8$ a příbuzných tetragonálních sloučenin

Autor: Petr Čermák

Katedra / Ústav: Katedra fyziky kondenzovaných látek

Vedoucí doktorské práce: doc. Mgr. Pavel Javorský, Dr., Katedra fyziky kondenzovaných látek

Abstrakt:

Intermetalické sloučeniny $R_2T\mathrm{In}_8$ (R = vzácná zemina, T = přechodný kov), obecně nazývané “218” díky jejich stechiometrii jsou strukturně příbuzné se skupinou známých cerových těžkofermionových supravodičů $\mathrm{CeCoIn_5}$ a $\mathrm{CeRhIn_5}$. Vy smyslu dimenzionality se nachází na pomezí plně trojrozměrných intermetalik se strukturou $\mathrm{CeIn_3}$ a kvazi-dvourozměrných “115” supravodičů. To z nich činí ideální kandidáty pro studium vlivu dimenze na jejich vlastnosti. Nedávný výzkum v oblasti „218“ sloučenin přinesl nové možnosti a odhalil existenci cerových sloučenin s paladiem a platinou na místě přechodného kovu. Díky tomu se jejich studium dostává do popředí zájmu, přestože byly dlouho dobu opomíjeny na úkor jejich mnohem známějších „115“ příbuzným.

Soustředili jsme se hlavně na vyhodnocení magnetických struktur a krystalovopolních efektů ve sloučeninách $R_2\mathrm{RhIn_8}$ s R = Nd, Tb, Dy, Ho, Er, Tm, La, Lu, Y. V této práci prezentujeme výsledky objemových měření (měrné teplo, magnetizace) následované vyhodnocenými magnetickými strukturami z řady neutronových experimentů.

Klíčová slova: růst krystalů, fázové diagramy, magnetická struktura, neutronová difrakce, grupová teorie

Title: Magnetic properties of $R_2T\mathrm{In}_8$ and related tetragonal compounds

Author: Petr Čermák

Department / Institute: Department of Condensed Matter Physics

Supervisor of the doctoral thesis: doc. Mgr. Pavel Javorský, Dr., Department of Condensed Matter Physics

Abstract:

Intermetallic compounds $R_2T\mathrm{In}_8$ (R = rare earth, T = transition metal), commonly called “218” because of stoichiometry, are structurally related to a class of well-known Ce-based heavy-fermions like CeCoIn_5 or CeRhIn_5. They are located between fully 3D cubic compound (e.g. CeIn_3) and quasi-2D “115” superconductors, which makes them ideal candidates to study structural dimensionality effects on various properties. Recent developments in this field showed that it is possible to grow compounds with T = Pd or Pt with “218” stoichiometry. Therefore further study of “218” compounds is desired since much less is known about them compared to “115” compounds.

We have focused mainly on the determination of magnetic structures and crystal field effects along the series of Rh based “218” compounds for various rare-earth elements. The single crystals of compounds with R = Nd, Tb, Dy, Ho, Er, Tm, La, Lu, Y were successfully grown. Results of bulk measurements (specific heat, susceptibility) together with magnetic structures determined from several neutron experiments are presented.

Keywords: crystal growth, phase diagrams, magnetic structure, neutron diffraction, group theory

Contents

Introduction

The group of heavy-fermion tetragonal compounds based on the $CeIn_3$ common structural unit became of great importance after the discovery of superconducting state in applied pressure in $CeRhIn_5$ [1] and later at ambient pressure in $CeCoIn_5$ [2] and $CeIrIn_5$ [3]. This family of structurally related compounds is generally written as $Ce_nT_mIn_{3n+2m}$ (where T is a transition metal element Co, Rh, Ir, Pd or Pt, n and m are integers) and consists of n layers of $CeIn_3$ alternated along the *c*-axis with m layers of TIn_2. The possibility of changing dimensionality in these materials by changing m and n ratio together with changing of T element gives scientist a big playground for tuning ground state properties of these compounds (e.g. [4]). Since the finding of analogies between heavy-fermion superconductivity and ^3He magnetic superfluid state it is believed that this phenomena is mediated by a nearly localized Fermi liquid and so it has magnetic origin [5]. Thus a detailed understanding of the magnetic interactions in these materials is crucial in pursuing the origin of unconventional superconductivity.

There are many competing effects in cerium compounds which influences formation of a magnetic ground state [4]. This makes the understanding of the physics behind more difficult, so there comes an idea of substituting cerium with other rare-earth element. By this substitution, we will lose the superconducting properties, but the magnetism will be still present.

Our idea is to look into the series of the non-cerium analogues of a well-known heavy fermion superconductor. Study of the evolution of macro- and microscopical properties along the rare-earth series will help us to understand influence of different effects to the formation of the magnetic ground state. We plan to study magnetic structures, so the natural candidates for studying are the compounds with T = Rh, because both $CeRhIn_5$ and Ce_2RhIn_8 give evidence of antiferromagnetic behaviour. Relatives of $CeRhIn_5$ are already well studied and there exist a comprehensive thesis about that compounds [6]. Therefore our choice was settled to study non-cerium analogues of Ce_2RhIn_8.

After the brief overlook of theoretical background in chapter 1, we move to the description of the used experimental techniques in chapter 2. Both introductory chapters contain only the most important information, which will be used later. But they are always accompanied by a number of references for further reading. Chapter

3 concerns current knowledge of the studied compounds and summarizes previous results.

The principal chapter is the next one, number 4. Here we will go through the whole process of condensed matter research. The idea is to start with sample preparation and characterization, continue with bulk properties and finally move to neutron diffraction study in order to determine detailed magnetic structure.

1. Theoretical background

1.1. Magnetism in $4f$ electron systems

At the beginning of this thesis we would like to explain basics of magnetic properties of the rare-earth compounds. Rare earth atoms (R) include 17 elements consisting of 15 lanthanides in addition to scandium and yttrium. These two are included from historical reasons (they were part of the same ore deposits), but their electronic configurations are different as they don't contain $4f$ electrons. Based on the atomic number, we can divide rare earths into light rare earths (lanthanum – europium) and heavy rare earths (gadolinium – ytterbium).

1.1.1. Free ion

Magnetic properties of rare earths are mainly influenced by the $4f$ electron shell. Boundary compounds of the lanthanide series have this shell empty (lanthanum) or fully filled (lutetium) and according to Hund rules they don't exhibit magnetic. Together with yttrium, they are often used as nonmagnetic analogues to the others.

In the majority of atoms, attractive forces between the nucleus and electrons are shielded by the electrostatic repulsion among electrons. This is not the case in rare earths, where the $4f$ electrons are very close to nuclei (see Figure 1) and thus do not provide such effective shielding. Therefore, the ionic radius is decreasing from La to Lu. This effect is called Lanthanide contraction.

One can now think that if $4f$ electrons are very close to nuclei, they do not influence the electronic properties of this compound. However, as shown in Figure 1, you can see that the tail of $4f$ wave function interferes with closed $5s$ and $5p$ orbitals. This result in hybridization between $4f$ and conduction electrons, which is responsible for RKKY interaction (see chapter 1.1.2) and also Kondo screening effects in cerium compounds.

Hund rules are very important for magnetism in rare earth compounds. Regarding the third rule, light rare earths have low total angular momentum $J = |L - S|$, while in heavy rare earths it is larger: $J = |L + S|$. Here L is total orbital momentum and S is the total spin momentum. The electronic configuration and fundamental magnetic parameters of rare earths are summarized in Table 1.

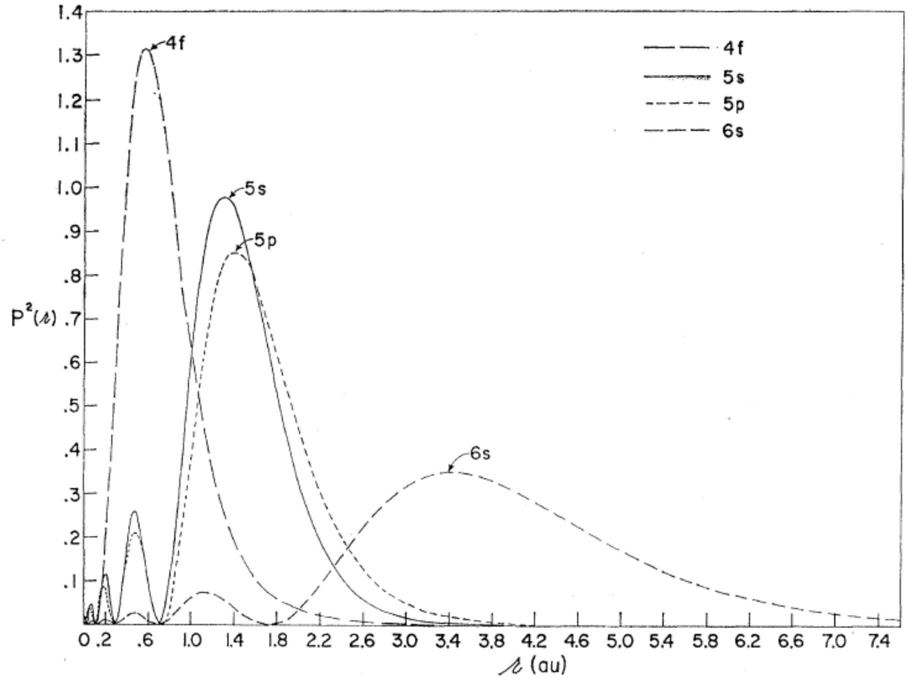

Figure 1 - Radial wave functions of Gd [7], which is typical in 4*f* compounds.

Table 1 - Magnetic parameters of rare-earth ions

	Z	$4f^n$	S	L	J	g_L	μ_{ORD}	μ_{eff}	G
La^{3+}	57	$4f^0$	0	0	0	0	0	0	0
Ce^{3+}	58	$4f^1$	1/2	3	5/2	6/7	2.14	2.54	0.178
Pr^{3+}	59	$4f^2$	1	5	4	4/5	3.2	3.58	0.8
Nd^{3+}	60	$4f^3$	3/2	6	9/2	8/11	3.27	3.62	5.11
Pm^{3+}	61	$4f^4$	2	6	4	3/5	2.4	2.68	3.2
Sm^{3+}	62	$4f^5$	5/2	5	5/2	2/7	0.71	0.85	4.46
Sm^{2+}	62	$4f^6$	3	3	0	0	0	0	0
Eu^{3+}	63	$4f^6$	3	3	0	0	0	0	0
Eu^{2+}	63	$4f^7$	7/2	0	7/2	2	7	7.96	15.75
Gd^{3+}	64	$4f^7$	7/2	0	7/2	2	7	7.94	15.75
Tb^{3+}	65	$4f^8$	3	3	6	3/2	9	9.72	10.5
Dy^{3+}	66	$4f^9$	5/2	5	15/2	4/3	10	10.65	7.08
Ho^{3+}	67	$4f^{10}$	2	6	8	5/4	10	10.61	4.5
Er^{3+}	68	$4f^{11}$	3/2	6	15/2	6/5	9	9.58	2.55
Tm^{3+}	69	$4f^{12}$	1	5	6	7/6	7	7.56	1.17
Tm^{2+}	69	$4f^{13}$	1/2	3	7/2	8/7	4	4.54	0.32
Yb^{3+}	70	$4f^{13}$	1/2	3	7/2	8/7	4	4.54	0.32
Yb^{2+}	70	$4f^{14}$	0	0	0	0	0	0	0
Lu^{3+}	71	$4f^{14}$	0	0	0	0	0	0	0

1.1.2. Rare-earth metals

The described localized properties of partially filled orbital are unique among other types of atoms. It also leads to well defined energy levels in the solid, which are nearly the same as in the free ion. This localized character has been be confirmed experimentally by measuring the effective magnetic moments μ_{eff} (see chapter 2.2.2). These moments are very close to full values expected from Hunds rules for free ion:

$$\mu_{eff} = \mu_B g_L \sqrt{J(J-1)} \tag{1}$$

where μ_B is Bohr magneton, g_L is Landé factor and J is total angular momentum.

Magnetic ordering in rare earth metals is mainly caused by the RKKY interaction. It is an indirect interaction which means that $4f$ electrons don't interact directly with each other, but locally interact with spin of conduction electrons. This interaction can be described by the exchange Hamiltonian H_{ex}:

$$H_{ex} = -\mathcal{J}(R_{ij}) S_i . S_j \tag{2}$$

where $\mathcal{J}$ is oscillating function with distance R_{ij}. These oscillations are called Friedel oscillations. $S_{i,j}$ are spins of the interacting electrons. De Gennes suggested that it is better to use quantum number J instead of S and replace S_i with projection of spin into the direction of J. The magnetic ordering temperatures will be than proportional to the de Gennes factor:

$$G = (g_L - 1)^2 J(J+1) \tag{3}$$

And the ordered moment will be close to:

$$\mu_{\mathrm{Ord}} = g_L J \tag{4}$$

The values of all these theoretical magnetic moments and factors are summarized in Table 1.

1.2. Crystalline electric field

Charge distribution around ions in a crystal lattice produces an electric field, called a crystal field (CEF). This field acts on electrons in the $4f$ shell, giving rise to the strong magnetic anisotropy of rare-earth materials. In a view of one atom, the crystal field removes directional degeneracy reflecting the symmetry of nearby atoms. Splitting of the multiplets depends on the crystal field symmetry. We can generally say that the splitting increases with lower symmetry.

As written above, $4f$ electrons are hidden deep inside an ion, so they are not much influenced by the crystal field. This implies separation of spin-orbit coupling (energies in order of 100 meV) and crystal field splitting. Typical crystal field splitting in rare earths correspond to energies of about 10 meV (hundreds of Kelvins). See Figure 2 for example of such splitting in Ce^{3+}.

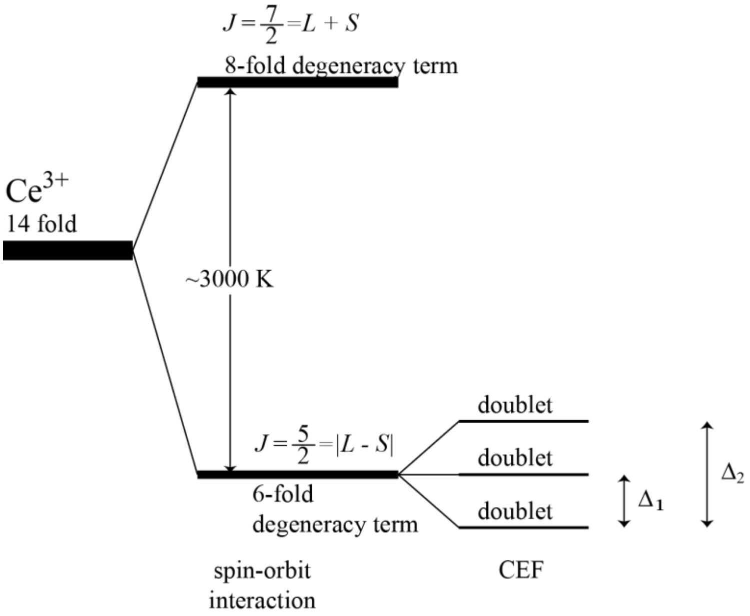

Figure 2 - Energy level scheme of $4f$ electrons in a cerium ion [6].

The calculation of the crystal field is possible from first principles. For described system with weak crystal field, we can express crystal field Hamiltonian with general relationship:

$$\hat{\mathcal{H}}_{CF} = \sum_{lm} B_l^m \hat{O}_l^m \tag{5}$$

B_l^m are crystal field parameters which can be calculated from a point charge model if we know the exact structure of the compound, otherwise it can be determined experimentally. $\hat{O}_l^m$ are Steven's operators representing the whole $4f$ shell (see [8] for details). The number of independent parameters in the B_l^m matrix depends on the symmetry of the crystal field. For example, given a cubic symmetry there are only two independent crystal field parameters B_4 and B_6, while for orthorhombic structure there are 9 independent parameters. In our case of tetragonal symmetry, equation (5) can be simplified to the form:

$$\hat{\mathcal{H}}_{CF} = B_2^0 O_2^0 + B_4^0 O_4^0 + B_4^4 O_4^4 + B_6^0 O_6^0 + B_6^6 O_6^6 \tag{6}$$

With the knowledge of the crystal field parameters, it is then straightforward to calculate the energy level splitting. The energy difference between ground state and n-th excited state is commonly marked as Δ_n, see Figure 2 for example.

If the compound contain odd number of f electrons, its J is half-integer and $4f$ energy levels always contain a so-called Kramers doublet. This degeneracy is based on the time reversal symmetry and is independent on crystal symmetry. External magnetic field breaks this doublet. For example all cerium compounds always split into maximum 3 energy levels (Figure 2).

1.3. Strongly correlated electron systems

A lot of magnetic systems can be understood in a very simplified view. We can assume that electrons do not interact with each other, but each electron is exposed to some effective interactions produced by an electron gas. This approach is called molecular field theory or sometimes theory of averaged fields. However in many cases, this simple approach is not enough and we have to consider other correlations between electrons. We called compounds exhibiting this behaviour strongly correlated electron systems because their correlations cannot be neglected. These include transition metals and their oxides, high-temperature superconductors and also cerium, ytterbium and uranium systems exhibiting Kondo interactions, usually called heavy fermion or electron compounds.

1.3.1. Heavy fermions

Heavy fermion materials have been a subject of study for nearly 40 years after the report of unusual properties of $CeAl_3$ in 1975 [9]. This group of materials is characterised by their anomalous specific heat. At low temperatures, the specific heat consists mainly from electronic contribution. This contribution is linear with temperature through a proportionality constant γ, also called Sommerfeld coefficient (more about specific heat is written in the chapter 2.2.1). Here for normal conductors, γ is in order of units of $\mathrm{mJ/mol.K^2}$. In heavy fermions, these values go up to 1000 $\mathrm{mJ/mol.K^2}$. This large value of Sommerfeld coefficient is ascribed to a large effective mass of the itinerant electrons – therefore the name Heavy fermions.

Heavy fermion materials are usually found in tetragonal and hexagonal cerium and uranium compounds. A large anisotropy in magnetic susceptibility is observed which indicates large crystal field effects. A simple CEF model is usually adequate to describe heavy fermion susceptibility.

A few years after discovering heavy fermions, the first heavy fermion superconductor (HFSC) $CeCu_2Si_2$ was reported by Steglich *et al.* [10]. Several uranium based ones were reported, but for over 20 years $CeCu_2Si_2$ and related compounds were the only cerium based HFSC. This was until 2000 when superconductivity in $CeIn_3$ was reported by Hegger *et al.* [1], producing much interest in HFSC. At present, there are over 40 HFSC exhibiting various structures and ground state properties.

In the framework of classical BCS theory, the presence of only a small amount of magnetic impurities will destroy superconductivity, because the interaction of two electrons in a spin singlet will break the pairing. But local magnetic moments always exist in heavy fermions, strongly affecting whole system, so superconductivity in these compounds seems unconventional.

The interplay between magnetism and superconductivity is still not understood. An important aspect in all unconventional superconductors is influence of dimensionality on the formation of the superconducting condensate. However it is not clear if it is driven by magnetic structures, which of course also depends on dimensionality. The microscopic coexistence of magnetic and superconducting state was observed in e.g. UPd_2Al_3 [11], and on the other hand large competition between those phenomena is reported for $CeCu_2Si_2$, where magnetism and superconductivity exists separately in domains [12]. Therefore the study of links between magnetism and dimensionality can bring important understanding to unconventional superconducting phenomena.

1.4. Magnetic propagation formalism

There are in general two ways of describing magnetic structure in materials. The first is very similar to the description of crystal structures: we define the magnetic unit cell and describe the positions, directions and amplitudes of the magnetic moments within. In addition to crystal structure, we must think more about the chosen coordinate system, because for lot of magnetic structures it is better to use polar instead of crystallographic coordinates. The biggest disadvantage of this method is that magnetic unit cell can be very big, sometimes thousands of magnetic atoms [13].

The second way is to use formalism based on describing atoms only in nuclear unit cell and propagation vectors, sometimes also called $\boldsymbol{k}$-vectors and labelled as $\boldsymbol{k}$. The direction and amplitude of the physical magnetic moment $\boldsymbol{\mu}_i$ associated with i^{th} atom in the unit cell is then described as

$$\boldsymbol{\mu}_i = \sum_{\{\boldsymbol{k}\}} \boldsymbol{m}_{i,\boldsymbol{k}} e^{-i\boldsymbol{k}\cdot\boldsymbol{T}}, \tag{7}$$

where $\boldsymbol{m}_{i,\boldsymbol{k}}$ is so called basis vector associated with propagation vector k and position of the atom i in the unit cell and $\boldsymbol{T}$ is lattice translation vector associated with the position of the magnetic moment. In general, the summation is done over the set of wavevectors $\{\boldsymbol{k}\}$. Both $\boldsymbol{k}$ and $\boldsymbol{m}_{i,\boldsymbol{k}}$ vectors are in general complex numbers. Luckily in the majority of compounds, this description can be simplified.

Let us now briefly describe the meaning of the term “star of the propagation vector”. For each propagation vector within the crystallographic unit cell, symmetry operations based on the space group describing the symmetry of the crystal can be applied. An application of rotational symmetry elements of the space group to the propagation vector will generate a set of unequivalent vectors. The set of these vectors is called star of the propagation vector. Each vector from this star is often called “arm of the star”. See Figure 3 for example.

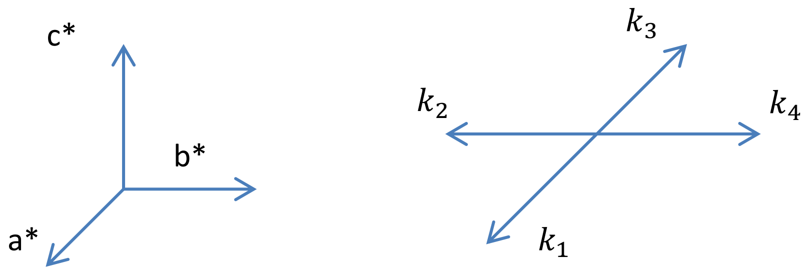

Figure 3 – The star of the propagation wave vector $\boldsymbol{k} = (\frac{1}{2}, 0, 0)$ in the tetragonal space group P4/mmm. The arm of the star are: $\boldsymbol{k}_1 = (\frac{1}{2}, 0, 0)$, $\boldsymbol{k}_2 = (0, -\frac{1}{2}, 0)$, $\boldsymbol{k}_3 = (-\frac{1}{2}, 0, 0)$ and $\boldsymbol{k}_4 = (0, \frac{1}{2}, 0)$.

Based on the number of arms from the star involved in magnetic structure, we can talk about four situations:

1. One propagation vector is preferred over others; we speak about single-k structure. It is the most common case and it is usually connected with generation of magnetic moments. In different magnetic domains,

different arms of the star are involved in formation of magnetic structures.

2. More arms from the star are involved simultaneously; we speak about multi-k structures.
3. Only one arm of the star is involved, but also with their harmonics. Which means that also propagation vectors $\frac{k}{2}, \frac{k}{3}$ can be involved in equation (7). Including higher harmonics to the generation of the magnetic structure will result in the squaring of sinusoidal modulation of the magnetic moments.
4. Case 2. and 3. together. We speak about crossed harmonics or intermodulated structures.

Also multiple $\boldsymbol{k}$-vectors from different stars can be connected with one atom.

Since $\boldsymbol{\mu}_i$ is physical magnetic moment, it cannot be expressed by imaginary number. Therefore when $\boldsymbol{m}_{i,\boldsymbol{k}}$ is real, the exponential must be also real or we need more propagation vectors to be involved. In simple case of single-k structure, we can expand the exponential to only its cosine component:

$$\boldsymbol{\mu}_i = \sum_{\{\boldsymbol{k}\}} \boldsymbol{m}_{i,\boldsymbol{k}} \cos(-2\pi \boldsymbol{k} \cdot \boldsymbol{T}). \tag{8}$$

The condition for zero sine component of exponential implies, that the cosine amplitude will be still equal to one and the only changing thing along the crystal will be sign in the components of the magnetic moment. It also implies that propagation must be commensurate (see below).

The second possibility how to ensure real $\boldsymbol{\mu}_i$ when $\boldsymbol{m}_{i,\boldsymbol{k}}$ is real is using more propagation vectors. Very often two arms of the star: k and $-k$ are involved. The imaginary component is then automatically cancelled out and equation (7) results in amplitude modulated magnetic structure.

The last thing which we mention in this chapter is classification of the propagation vectors on the basis of its size. We distinguish structure where:

1. $\boldsymbol{k} = (0, 0, 0)$

   There belong all ferromagnetic structures and also other structures where magnetic unit cell and crystallographic unit cell are equivalent. Magnetic reflections in appears on the same positions as nuclear ones.

2. $\boldsymbol{k} = (a, b, c) \wedge a, b, c \in \mathbb{Q}$

   Components of the propagation vector must be rational, but they are often equal to simple fraction like $\frac{1}{2}$. In the case of half-integer propagation magnetic reflections will occur in the half-integer reciprocal coordinates. We speak about commensurate structures (C).

3. $\boldsymbol{k} = (a, b, c) \wedge (a \vee b \vee c) \in \mathbb{R} \setminus \mathbb{Q}$

   When one of the component of the propagation vector is rational, two arms of the star $\boldsymbol{k}$ and $-\boldsymbol{k}$ must be involved in the structure. Each nuclear peak in diffraction pattern will be surrounded by pair of magnetic reflections, called satellites. These magnetic structures are called incommensurate (IC).

For further reading about magnetic structure description and also their determination using group theory we recommend excellent summary paper by Wills [13].

2. Experimental methods

This chapter we will give the reader brief description of the techniques used. We will describe in detail mainly the neutron scattering techniques, as the neutron diffraction experiment represent the major part of the thesis.

2.1. Sample preparation

At the beginning of every condensed matter research activity one must prepare samples or use samples prepared by someone else. The topic of this thesis brings us opportunity to grow samples by ourselves and therefore go through the whole process from the beginning.

2.1.1. Flux growth technique

Single crystals can be prepared by a large variety of techniques. We can classify them accordingly to the main principle: growth from a melt (Czochralski method, Bridgman technique, Zone melting technique) and growth from a solution (so called flux growth). Our samples grow incongruently and thus flux growth is the only way to prepare them, so this brief introduction will focus on this technique.

The basic principle of solution growth method is following. First the starting composition is prepared, which is generally different from the final composition of the sample. Usually there is an excess of one element with small melting temperature, called flux. In the case of self-flux (sometimes called true flux method) growth, this element is also part of the final product. Then the starting composition is heated to reasonably high temperature to melt all components. After some time (approx. 2 hours) designated to stabilize thermodynamical equilibrium, the cooling of the melt begins at a very slow constant rate. When temperature of the solution reaches the solid-liquid line in the phase diagram, single crystals start to grow while the solution becomes flux richer. This cooling process must be stopped punctually to avoid growth of other parasitic phases. The last phase is the centrifugation of the remaining flux.

The size and purity of final single crystals is often extremely sensitive to speed of cooling and of course starting composition. While the starting composition can be roughly estimated from the binary or ternary phase diagrams of used elements, the cooling rate must be determined experimentally. This means especially for new compounds trial-and-error method must be used. Further explanations and also step by step description of solution growth process is described, for example, in Klára Uhlířová's thesis [14].

2.1.2. Sample characterization

One of the advantages of the solution growth technique is that grown crystals have natural shapes, so we can easily distinguish by eye between hexagonal plates, needles, cubes and others. Careful analysis is however still necessary. First the crystals were analysed by microprobe and then the lattice parameters were determined using single crystal X-ray RIGAKU RAPID II diffractometer. Energy dispersive X-ray (EDX) analysis, also called microprobe technique, was done on scanning electron microscope Tescan Mira I LMH equipped with EDX detector Bruker AXS.

2.2. Bulk measurement

Bulk measurement techniques are the first step in determination of physical properties of a given compound. In this thesis we will focus on specific heat and magnetization measurements since these two techniques are crucial for building phase diagrams and also very helpful in case of unveiling magnetic structures.

2.2.1. Specific heat

Specific heat (or heat capacity) is tightly bound to the total free energy and to amount of order in the sample. Every physical phenomenon, which influences the energy states of particles in the material, will contribute to its specific heat. The existence of bulk measurement reflecting microscopic changes in sample is very useful, but brings also some difficulties. The main problem of the specific heat analysis is the difficulty of differentiating between individual contributions. The total free energy of system is the sum of the free energies of its components so that the total specific heat is the sum of these contributions.

One method of extracting the individual parts is based on choosing a temperature range, where one of these contributions is dominant. A very important contribution to overall specific heat C is the lattice vibrations (phonons) - C_{ph}. The contribution of conduction electrons $C_{el} = \gamma T$ is always present in conductive samples. Influence of CEF to the atoms with non-zero total magnetic moment gives rise to additional contribution, the Schottky specific heat. Magnetic ordering, formation of a superconducting state and other phase transitions are connected with a change in entropy and thus also contribute to the specific heat as a jump in its temperature dependence.

The phonon contribution, C_{ph}, depends on the phonon spectrum, which can in general, consist of 3 acoustic and $3n-3$ optic branches. In the pursuit of finding suitable expression for C_{ph}, the Debye model can be applied to the three acoustic branches and the Einstein model to the remaining optic ones. To take into account effects of anharmonicity which is not included in the models above, an anharmonic correction proposed by Martin [15] can be added. It is represented by a single parameter α which is 0 in the case of no anharmonic correction. This approach leads to following overall phonon specific heat description:

$$\begin{aligned} C_{ph} = {} & \frac{1}{1-\alpha_D T}\frac{9R}{x_D^3}\int_0^{x_D}\frac{x^4 e^x}{(e^x-1)^2}dx \\ & + \sum_{i=1}^{30}\frac{1}{1-\alpha_{Ei}T}Rx_{Ei}^2\frac{e^{x_{Ei}}}{(e^{x_{Ei}}-1)^2} \end{aligned} \tag{9}$$

where $x_D = \frac{\theta_D}{T}$, $x_E = \frac{\theta_E}{T}$, α_D and α_{Ei} are the anharmonic coefficients, R is the gas constant and θ_D and θ_{Ei} are the characteristic Debye and Einstein temperatures, respectively. At temperatures well below θ_D, the influence of the optic phonons can be neglected and the expression (9) can be reduced to only Debye contribution in the T^3 approximation.

The electronic and phonon low temperature contributions can be written as:

$$C_p = \gamma T + \beta T^3 \tag{10}$$

where β is a constant directly related to θ_D.

The splitting of degenerate ground states due to CEF brings an increase of entropy and thus a related specific heat contribution. This contribution is often called Schottky specific heat C_{sch} which is given by relation:

$$C_{sch} = \mathrm{k_B N_A}\left(\frac{\sum_{i=1}^{n}\left(\frac{E_i}{\mathrm{k_B}T}\right)^2 e^{-\frac{E_i}{\mathrm{k_B}T}}}{\sum_{i=1}^{n} e^{-\frac{E_i}{\mathrm{k_B}T}}} - \left(\frac{\sum_{i=1}^{n}\frac{E_i}{\mathrm{k_B}T}e^{-\frac{E_i}{\mathrm{k_B}T}}}{\sum_{i=1}^{n} e^{-\frac{E_i}{\mathrm{k_B}T}}}\right)^2\right) \tag{11}$$

where n is the number of energy levels ($n = 2J+1$) and E_i is energy of the level i.

We can simply calculate the total amount of the entropy connected with the crystal field splitting as

$$\Delta S = R \ln n. \tag{12}$$

All specific heat measurements were performed using PPMS instrument on single crystalline samples. Samples were attached to the sample holder (puck) by apiezon N grease to enhance thermal contact between sample and puck. Instrument software uses two-τ relaxation method, details of this measurement technique are described for in [16] or in simple way in my diploma thesis [17]. To determine the exact amount of the grease used for measurement, we always start measurement by measuring only empty puck with grease (few points at low temperatures) and then we attach our sample to the prepared grease. We can then determine the heat capacity of the sample by subtracting empty puck (with grease) from the system sample + puck.

2.2.2. Magnetic susceptibility and magnetization

Magnetic structures in rare-earth compounds are often formed at very low temperatures. Above the transition temperature, the compounds behave as paramagnet and net magnetic moment in zero magnetic fields is naturally zero. By applying an external magnetic field to the sample, individual magnetic moments flip in the direction of the applied magnetic field. This response to magnetic field is called the susceptibility, χ, and can be described by Curie-Weiss law in the paramagnetic region:

$$\chi = \frac{N_A \mu_b^2 \mu_{eff}^2}{3k_B(T - \theta_P)} + \chi_0 \tag{13}$$

where θ_P is the paramagnetic Curie temperature, χ_0, and includes the Pauli and Van Vlack susceptibility. The experimentally measured effective magnetic moment μ_{eff} can be compared with theoretical value from equation (1).

Magnetization and susceptibility measurements were carried out using the Quantum design PPMS instrument using the vibration sample magnetometer (VSM) technique. Magnetic susceptibility was usually measured under a small field of 0.1 T, and magnetization was measured in magnetic fields up to 14 T.

2.3. Neutron scattering

Neutron scattering is one of the very powerful solid state experimental techniques due to the neutron's unique properties. Although the total charge of neutron is zero, its internal charge distribution leads to a none-zero magnetic moment. In comparison to the Bohr magneton, the nuclear magneton of neutron is significantly smaller (1836 times), but this magnitude is still enough to interact with magnetic moments in matter. Neutrons can be produced in nuclear reactions, either by hitting a target with accelerated charged particles (spallation) or by absorbing thermal neutrons in ^{235}U nucleus (fission). Neither of these methods can be performed in small-laboratory conditions, so large facilities are needed.

Neutron scattering techniques can be divided into two groups based on the way neutron interacts with matter. If the energy of incoming and measured neutron is same, we speak about elastic scattering, or diffraction. The other case, when neutron gains or losses energy in the sample is called inelastic scattering. This technique is used to study dynamics in materials, its energy levels and excitations. Since this thesis is devoted to study of magnetic structures, we will focus on neutron diffraction as a very important probe to magnetic structure of materials.

The basics of the diffraction will not be described in this thesis, although very good introduction to this technique is given for example in [18]. Neutron diffraction is very similar to X-ray diffraction, but has some important differences. For further understanding we will introduce following basic relations. The intensities of the reflected beam are in general proportional to the square of structure factor F_{hkl}:

$$I \propto |F_{hkl}|^2 \tag{14}$$

where structure factor for neutron nuclear scattering is given by:

$$F_{hkl} = \sum_i b_c \, e^{-iqr_i} e^{-W_i} \tag{15}$$

Here the summation is calculated over the primitive cell, b_c is the coherent scattering length, q is the momentum transfer vector in reciprocal space related to hkl position, r_i is position of the i-atom and W_i is temperature factor. The scattering length is the reason why neutron scattering differs from the X-ray one. The structural neutron cross-sections are related to strong forces in nuclei and their values do not depend on atomic weight (like for X-rays). So it is very tough to distinguish neighbourhood atoms in periodic table by classical X-ray scattering, but it is usually much easier with neutrons. The absorption cross-section is in general much lower for neutrons. However there exist a few elements (specific isotopes) that are very strong neutron absorbents (e.g. ^{6}Li, ^{10}B, ^{157}Gd).

The most important feature of neutrons is the magnetic contribution to the scattering which is often as strong as nuclear one. In recent years, huge increases of synchrotron sources brilliance leads to the possibility to measure magnetic structures also with X-rays, but neutron diffraction still remains standard way of determining magnetic properties of solids. The magnetic scattering leads to additional diffraction pattern comparable with nuclear. The magnetic structure factor F_M is defined as:

$$F_M = p \sum_j f_j(q) m_j e^{-iqr_i} e^{-W_i} \tag{16}$$

The constant $p = 0.2696\ 10^{-12}$cm, $f_j(q)$ is magnetic form factor of j^{th} atom, m_j is the magnetic moment. Magnetic form factors are tabulated and unlike nuclear scattering length they depend on q and usually decrease faster than X-ray form factors.

The biggest disadvantage of neutrons is the relatively low flux produced by neutron sources. Even a normal laboratory X-ray generator produces photon beams with much higher intensity than a nuclear reactor. The synchrotron source then produces several orders of magnitude higher flux.

In the next section we will describe in more detail the instruments D10, IN3, VIVALDI, CYCLOPS and OrientExpress at Institute Laue Langevin (ILL) and instrument E4 in Helmholtz-Zentrum Berlin (HZB) used for performing diffraction experiments in this work..

2.3.1. Geometry of single crystal diffractometers

In order to solve the crystallographic structure of a material, we need to measure the intensities of many Bragg reflections as possible. The most simple way to do this is using 2-axis diffractometer. This precision instrument has two independent axes of rotation, commonly called 2θ and ω. The first one (rotation of detector) is used to satisfy Bragg's law under the condition of crystal cell parameters and incident monochromatic wavelength and the second one (sample rotation) is used to determine the intensity dependence on this angle. A basic layout of this setup is shown on Figure 4. With this geometry one can measure all reflections in the so called scattering plane, because in this setup there is no possibility to rotate crystal out of this plane. 2-axis instruments are often used to measure samples in extreme conditions, typically under high magnetic fields, because magnets cannot be tilted. Example of instrument with such geometry is E4 in HZB. It is also possible to use triple axis spectrometer (like IN3) to measure diffraction in 2-axis geometry (simply by setting analyser to see elastic neutrons). Some instruments have ability to lift the detector from the scattering plane to increase the coverage of reciprocal space (like on D23 in ILL) or they have big two-dimensional detector in which they can record also out-of-scattering-plane peaks (like on E4).

Because of the needs for accessing nearly full reciprocal space more advanced concept of 4-circle diffractometer is used. Two additional angles are used to change the scattering plane. See Figure 5 for the details of a typical instrument layout. For example D10 diffractometer can work in this geometry.

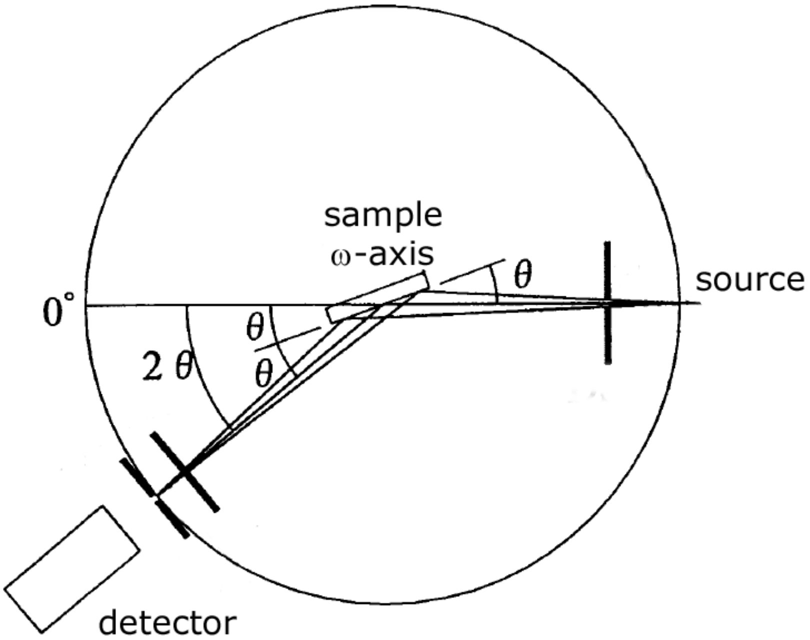

Figure 4 - basic layout of two-axis diffractometer (taken from [18])

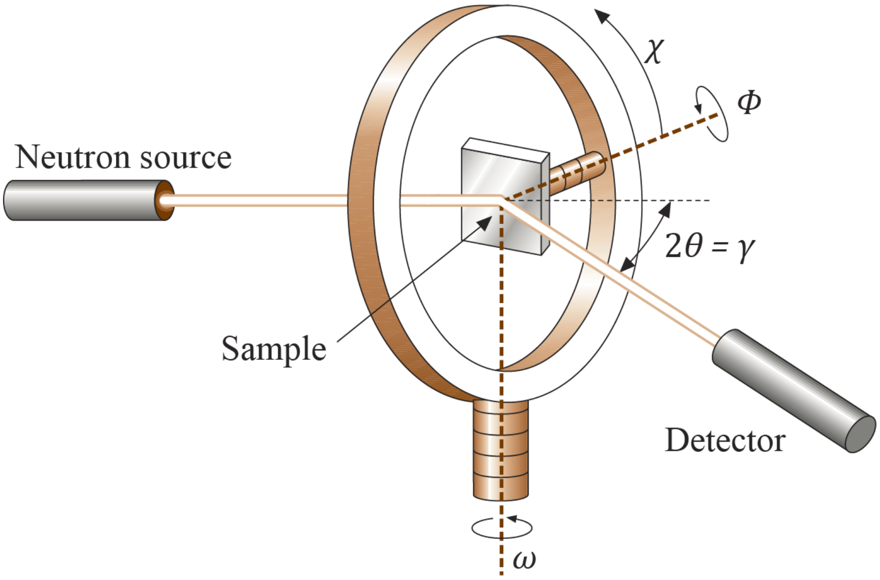

Figure 5 - layout of 4-circle diffractometer (edited picture taken from [19])

2.3.2. Neutron detectors

The advantages of neutrons were described in the beginning of Chapter 2.3 and there it was stated that they can penetrate deeply into matter. This implicates complications in the process of detection. In contrast to electrons, there is no method for detecting neutrons passing by the detector. In other words – if we want to detect neutron, we have to destroy it.

The most commonly used neutron detectors are ^{3}He gas tubes. Here, the neutron is absorbed by helium atom and produces charged particles with high energies. These particles are then easily detected and because of their high energy, it is easy to distinguish them from γ-radiation. An advantage of this method is very high efficiency; disadvantages are the lack of ^{3}He availability in the recent years and relatively low spatial resolution (in case of position sensitive detectors).

Other possible method represents scintillation detectors. Neutrons are absorbed in a plastic loaded with ^{6}Li or ZnS and the charge reaction creates decay of light quanta which goes through a photo-multiplier and are then detected by common CCD camera. These detectors are position sensitive, but they are not well suited for low flux detection as they are also sensitive to γ-radiation, which increases background.

When measuring single crystal diffraction on 1D detector (IN3), results of one ω-scan is a one-dimensional dependence of intensity on the ω-angle. When using 2D area detector (also called position sensitive detector - PSD) on D10 or E4, the result of this measurement is a 3D set of intensities.

2.3.3. Evaluation of single crystal experiments

Each experiment starts with sample orientation, centring, adjusting of incoming and outgoing slits. In the case of 2-axes layout, orientation of the sample means refinement of scattering plane, either by using cradle tilt angles on IN3 or by manually tilting the crystal holder on E4. When the scattering plane is correctly set, the only remaining parameter is the offset of the 2θ (denoted as A4 on IN3) angle. By measuring scans along the main crystallographic directions, we are able to refine the cell parameters of the measured sample. Any measured scan that cuts the Ewald sphere with reflection can contribute to square of modulus of the structure factor F. The ω-scan is also this case. This method is called the rotating crystal method. To obtain the integrated intensities, one should simply subtract the background and integrate the remaining intensity over ω. The background subtraction is commonly done by fitting measured data with a Gaussian, or Voigt function plus a constant background.

The situation is more complicated on the 4-circle diffractometer D10, where the orientation of the sample is defined by 3x3 orientation matrix; a so-called UB-matrix. Because of the 2D detector on D10, it is possible to orientate in an automatic way. First we rough adjust the UB-matrix as in the 2-axes geometry. Then we measure approximately 30 of the strongest reflections and integrate them. Program RACER [20] is used to integrate measured 3-dimensional data on D10. From the set of measured reflections it is possible to refine the UB-matrix and also cell parameters of the measured sample. This refinement is done automatically by the program rafd9 [21]. With refined UB-matrix we are prepared to measure a set of nuclear or magnetic reflections. Their intensities are then integrated using program RACER, obtaining a list of h, k, l indices and corresponding intensity value.

The measured set of integrated intensities are corrected to account for various effects to obtain square of structure factor F:

$$|F|^2 = \frac{y}{LA} I_0 \tag{17}$$

where I_0 is integrated intensity and three reduction factors are described below.

1) Lorentz factor, L

If we scan the crystal at constant speed of rotation, different reciprocal lattice point pass through the Ewald sphere with different speed. Correction for this difference is called the Lorentz factor, or sometimes the angular velocity factor. The basic expression is very simple and can be derived for all types of scans [22]. For normal beam geometry (four-circle setup on D10 or 2-axis diffractometer) a simple expression is used:

$$L^{-1} = \sin 2\theta \tag{18}$$

For the D10 diffractometer this correction is automatically calculated in the integration program RACER, but if we will integrate measured peaks manually, we must apply this correction factor. The expression is not valid if the detector is out of the equatorial plane, but this is not the case of our measurements. It is also not valid when using collimator before the detector [23], but this correction is very small and can often be neglected [24].

2) Extinction factor, y

Kinematical diffraction theory assumes that the incident and diffracted patterns are not attenuated by the sample. This is obviously not true. The size of this effect depends on the size and mosaicity of the domains in the sample and because these values are not generally known, the only way to treat this correction is by fitting.

The simplest way to implement this is with the phenomenological Zachariasen formula [25, 26]:

$$y = \left(1 + X\frac{0.001F^2\lambda^3}{sin(2\theta)}\right)^{-\frac{1}{2}} \tag{19}$$

where X has no physical meaning. More precise modelling of extinction is to use same equation but with different X for different crystallographic direction. Then parameter X is calculated from equation:

$$x = \left(\frac{\lambda}{2\sin\theta}\right)^2 (X_1h^2 + X_2k^2 + X_3k^2 + X_4hk + X_5hl + X_6kl) \tag{20}$$

and all 6 parameters X are used as a fitting parameter.

If we want to determine some microscopical properties of our sample, we must know the absorption weighted path of the incident and diffracted beam for each reflection. These values can be calculated for each reflection e.g. using program DATAP [27] (if we know shape of our crystal). With knowledge of these parameters, the Becker Coppens algorithm [28] can be used:

$$
\begin{gathered}
y = \sqrt{\frac{1}{1 + 2x_G + A\frac{{x_G}^2}{1 + Bx_G}}} \\
x_G = cF_c^2\frac{R}{a}\left(1 + \frac{9}{8}\left(\frac{R}{aG}\right)^2\right)^{-\frac{1}{2}} \\
a = \frac{\lambda}{\sin 2\theta} \\
c = \frac{1000T_{bar}\lambda^3}{V^2\sin 2\theta} \\
A = 0.58 + (0.48 + 0.24\cos 2\theta)\cos 2\theta \\
B = 0.02 - 0.025\cos 2\theta
\end{gathered}
\tag{21}
$$

where T_{bar} is the absorption weighted path of the incident and diffracted beam within the crystal, R is the domain radius and G is the width of mosaic spread of the domains. All these described models can be fitted using the program Fullprof [29].

3) Absorption factor, A

When neutrons passes through the homogenous matter of a thickness t, their intensity is always reduced by:

$$A = \exp(-\alpha t) \tag{22}$$

where α is total linear absorption coefficient. This effect is caused by nuclear capture process in the nucleus of atoms (so called true absorption) and coherent and incoherent scattering. For the single crystal measurement, the last two effects are treated as a part of the extinction. The linear absorption coefficient depends only on the composition of the sample and can be calculated using:

$$\alpha = \frac{n}{V}\sum_i \sigma_i \tag{23}$$

where n is number of formula units in unit cell, V is the unit cell volume and σ_i is absorption cross section of i atom. Values of the absorption cross sections are different for different isotopes, depend linearly on the used wavelength in the region of neutrons used by diffraction experiments and are tabulated for all known isotopes [30].

Calculation of absorption is not trivial and requires knowledge of the shape and the sizes of the sample. It is possible to use the program DATAP [27] for such calculations. It uses the method of Gaussian grid integration, see more details about this method in [31].

Apart from three described reduction factors, there are additional effects that are difficult to express analytically, but it is important to know about them:

Thermal diffuse scattering

During our experiment we do not detect only elastic Bragg reflections but also incoherent scattering and inelastic phonon scattering. We can easily get rid of incoherent scattering by subtracting background. Treatment of inelastic phonon scattering is much trickier. The easiest way is to use energy analysis (as on IN3) and then the measured data contains only elastic signal.

Treating the inelastic phonon signal from a Bragg reflection depends on the elastic constants of a material and it is not easy to calculate it. Since this effect is small and affects only thermal displacement parameters, thermal diffuse scattering is usually ignored.

Multiple diffraction

When more than one reciprocal lattice point is very close to Ewald sphere, incoming intensity is divided between these reflections. The observed intensity is than smaller than expected. Extinction is a special case of multiple diffraction, when scattering is related to only one reciprocal lattice point. For standard diffraction experiment, where we collect large number of reflections, it is possible to neglect multiple diffraction effect.

The integrated intensities corrected for Lorentz and absorption correction are used as an input for the least-square fitting program Fullprof [29]. Using this technique it is possible to refine the magnetic structure and size of the magnetic moments, structural parameters, changes in occupancy and other microstructural data.

From the temperature dependence of selected magnetic intensity, it is possible to determine the zero-field spontaneous magnetization and thus the critical exponent, β [32]. Below the Néel transition temperature, the order parameter is connected with staggered magnetic moment, which is proportional to square root of measured intensity. Thus we can fit data below transition temperature to expression:

$$I \propto (T_N - T)^{2\beta} \tag{24}$$

From the mean field theory β critical exponent should be equal to $1/2$, but in reality it is significantly lower. For the 3D Ising magnetic lattices $\beta \cong 0.313$, while for Ising 2D model it was exactly calculated that $\beta = \frac{1}{8}$ [33]. The critical exponent β was also calculated for X-Y ($\beta = 0.345$) and Heisenberg ($\beta = 0.367$) model.

2.3.4. Laue technique

Laue diffraction is the process of scattering that occurs when a stationary crystal is illuminated by a white (polychromatic) beam. This experiment was first proposed by Max von Laue which lead to the discovery of X-ray diffraction by crystal lattice in 1912 [34]. The experimental arrangement for this method is very simple. A stationary crystal is illuminated by a white beam producing a so-called Laue pattern on neutron sensitive plates.

Two types of detectors are used nowadays. The first possibility uses neutron-sensitive image plates, upon which the diffraction pattern is recorded. These plates are read after each exposure by a rotating laser detector. This type of detector is used on the very-intense vertical-axis Laue diffractometer (VIVALDI) [35]. This type of detector is very efficient and suitable for small samples, but the biggest disadvantage is a slow readout and erasure time of 5 minutes together.

The other possibility is using CCD-based detectors. In this system high-performance image-intensified CCD cameras view a large-area neutron scintillator via close focus lenses. This technique allows capturing Laue diffraction pattern in much shorter time (few seconds) than image plate technique. Thanks to this speed it is possible to use CCD cameras for orienting the sample, as in instrument OrientExpress at ILL [36]. This does not exclude utilization of CCD-based detectors to also record a full Laue pattern. This idea was for the first time used in Cylindrical CCD Laue Octagonal Photo Scintillator (CYCLOPS) [37]. The CYCLOPS instrument is composed of 16 detectors arranged to octagonal geometry.

Now we will explain basics of Laue method. Contrary to single crystal monochromatic diffraction, here a stationary crystal is irradiated by polychromatic beam. This results not in a single Ewald sphere, but in a range of such spheres. The largest spheres correspond to shortest wavelengths and vice-versa. All of them pass through the origin of the crystal lattice. As you can see from Figure 6, all reciprocal-lattice points lying between the boundary spheres corresponds to possible reflections. This is the reason why stationary crystal can give rise to a large number of simultaneously produced reflections.

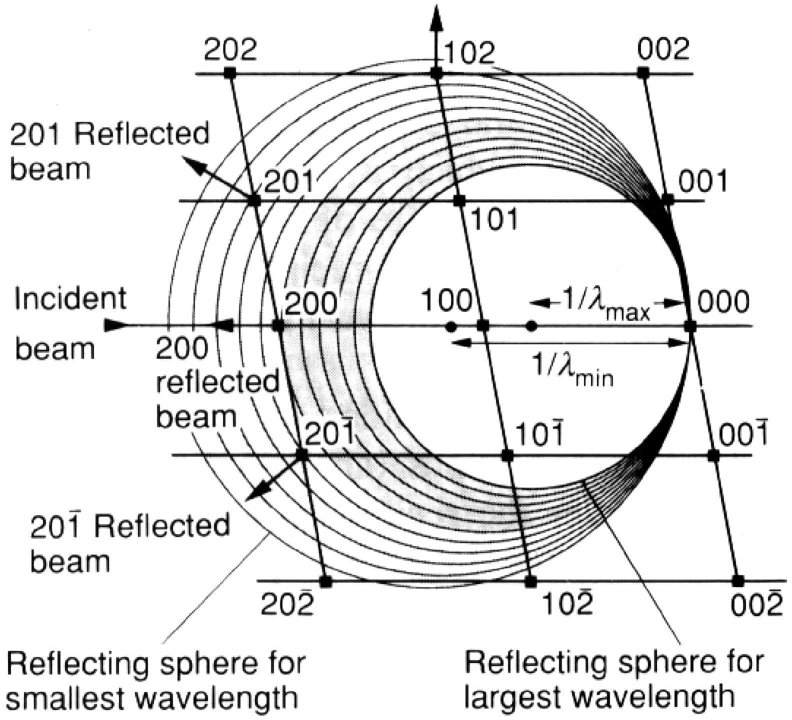

Figure 6 - Ewald construction for a white beam (from [38])

2.3.5. Treating Laue data

The indexing of the Laue patterns is not so simple as for experiments with constant wavelength. It was even believed that it is not possible to use Laue data for structure determination. However the big improvements in synchrotron sources and detectors showed that after very short times, lots of information about the sample can be collected and also evaluated. This technique is massively used, especially for structure determination of protein crystals. The VIVALDI and CYCLOPS instruments are the newest attempts to do the same on the neutron sources with all the advantages of neutron radiation (like sensitivity to the magnetic moment).

The result of a typical neutron Laue experiment is a set of high-resolution images taken at defined experimental conditions, as temperature or ω-angle (sometimes also called spindle angle). In case of the image plate detector on VIVALDI, these images are ready for indexation. The CCD cameras exhibit noise and also different cameras have different efficiency, so the CYCLOPS images need some pre-processing. First step is to de-noise the image (this is done by floating window averaging) and apply alpha-correction to get rid of different detector efficiencies. Because standard Laue indexing software works with plane geometry (as in OrientExpress) or cylindrical one (as in VIVALDI), octagonal geometry in Cyclops must be transformed to the cylindrical. The next optional step is subtraction of the background (taken for example from empty cryostat measurement). Finally we can proceed to pattern treatment.

On the following paragraphs the Laue pattern treatment in the software Esmeralda Laue Suite [39] will be described, but general principles are the same in the other software suites. First we search for experimental reflections in the pattern. There are two algorithms to do that, first (automated peak finding) checks the high intensity spots and derivative of intensity around them. Second one (threshold) divides whole pattern into small blocks, calculates the average intensity in each block and marks pixels with intensity above given threshold. The parameters for a peak finding should be always adapted to suit the treated image.

With a set of experimental peaks it is possible to use one of the three automatic orientation routines.

1. <u>Stepwise rotation around nodals</u>: one must set at least one bright spot in the pattern which would probably correspond to some main reciprocal lattice point (like 1 0 0). The algorithm then tries to rotate crystal around these selected “nodal” points (which is only one-dimensional problem). The number of selected nodal points linearly increases calculation. Because of that reason it is better to start with only one nodal point. This method always results in some solution, even if it is wrong. Details and advantages of this method are described in [40].
2. <u>Angle comparison of Obs-Calc peaks</u>: In this method a small number of strongest reflections is chosen for orientation (like 20). Then the angular distance for each two spots is calculated and compared with the generated angular distances for all reflections up to chosen Miller index. This method may not find solution at all, so one must properly choose the strongest reflections. It is not suitable for weak, diffuse or smeared spots, because in that case the angle between reflections is not

calculated properly. See [41] for details and the mathematical background.

3. <u>All possible rotations</u>: Running this algorithm from the scratch means totally brute force algorithm, trying all possible orientations (a three-dimensional problem). Without knowledge of rough orientation it takes very long time (up to days) and it is recommended to use another method. However if we know approximate orientation, we can try only orientations in limit of few degrees around it.

After proper indexing of the experimental spots, there is time for refining not only orienting angles but also the tilts and offsets of the detector, cell parameters and other distortions. This is done using least squares refinement. Experimental peaks must be indexed before running this routine, which means there are created corresponding pairs of experimental and calculated peaks. The distance between these pairs of peaks is then minimized during the refinement process. It is usual to re-index the peaks after the refinement and run the refinement procedure again on the larger set of input data.

Integration of the calculated reflections is the final step. The parameters for integration are only the size of circles around each reflection which to integrate and the size of the border of these circles. From the intensity in the border, the background is calculated and then subtracted. Esmeralda is also able to take into account the overlap of close reflections. The second possibility for integration is program Argonne-Boxes which integrates peaks in a more sophisticated way (it treats them as ellipsis, not circles) but cannot treat overlapping reflections [20].

3. State of the art: “218”, “115” and related compounds

As was stated in the chapter 1.3.1, $CeIn_3$ compound was the first heavy fermion superconductor [42] with different structure than $CeCu_2Si_2$. Discovery of superconductivity under applied pressure was followed by discovering ambient pressure superconductivity in $CeCoIn_5$ [2] and $CeIrIn_5$ [3]. All these compounds belong to the family of structurally related compounds which is generally written as $R_nT_mX_{3n+2m}$, where R is rare earth, T is a transition metal element Co, Rh, Ir, Pd or Pt, X is In or Ga and n and m are integers. In this chapter we will describe some important aspects why is this group of compounds interesting. We will also summarize previous results related to our further study.

3.1. Crystal structures

All $R_nT_mX_{3n+2m}$ compounds are tetragonal (or cubic in the special case of m = 0) with lattice parameter $a \cong 4.6$ Å and c parameter varying with different layering. This layering feature is crucial and makes these systems ideal candidates for studying heavy-fermion superconductivity. Every compound consists of n layers of RX_3 alternated along c-axis with m layers of TX_2 building blocks. By changing m and n, we can change dimensionality of the rare-earth atoms, which are responsible for magnetism and, in case of cerium also superconductivity of these systems.

The simplest case is when $m = 0$ and $n = 1$: this structure is simple cubic, space group $Pm\bar{3}m$, and has a $AuCu_3$ structure type (Figure 7a). These compounds are fully three-dimensional – each rare-earth atom has six nearest neighbourhood rare-earth atoms spread along all three main crystallographic directions. Because of the stoichiometric coefficients is this structure called “13” (read as one-three).

By inserting a layer of transition element atoms between layers of rare-earth atoms, one can obtain so called “115” structure (Figure 7c). Here $m = 1$ and $n = 1$, so structure is tetragonal with space group $P4/mmm$ and $HoCoGa_5$-structure type. It is most known because of its superconducting member $CeCoIn_5$ [2]. See next chapter for detailed properties of these compounds.

Compounds with this structure are incongruently growing, so the flux growth method is the only possible method for their preparation. This technique requires lot of tries with different starting compositions to be able to produce a large sample. During some preparation attempts another structure called “218” [4] was discovered.

It is also tetragonal with the same space group, but has $m = 1$ and $n = 2$ and it has Ho_2CoGa_8-structure type (Figure 7b). It is often stated, that “218” structure is in between “115” and “13” compounds by means of dimensionality [4].

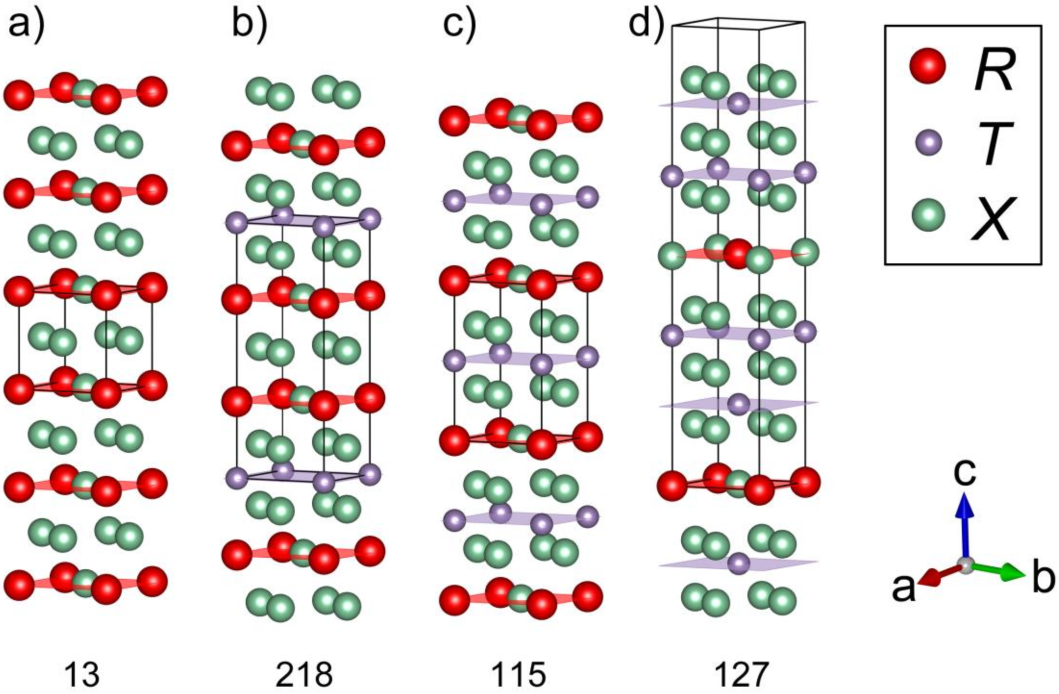

Figure 7 - Evolution of dimensionality in $R_nT_mX_{3n+2m}$ systems

In the year 2008 it was discovered even more two-dimensional system with $m = 2$ and $n = 1$ (Figure 7d), so called “127” [43]. It is also tetragonal but it crystallizes in body-centred space group $I4/mmm$. That is also the reason why its unit cell is two times larger in c direction than in case of “218” compounds. The latest progress in preparation of heavy-fermion superconductors shows the possibility to grow structures with even higher m and n values [44].

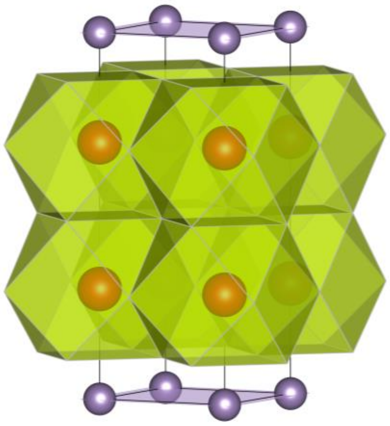

Figure 8 - cubooctahedron arrangement of indium (respectivelly gallium) atoms around rare-earth position in “218” structure.

A very important crystallographic common property of all these systems is existence of cubooctahedron of In/Ge (=X) atoms around a rare-earth atom, R. This feature is displayed in the Figure 8. Existence of this shielding gives unique properties in these systems [45], as will be described later.

3.2. Cerium compounds overview

Undoubtedly the most interesting compounds in studied materials are cerium based heavy-fermions. The simplest case is $CeIn_3$, where the cerium atoms have fully 3D character. It orders antiferromagnetically (AF) at $T_N = 10$ K with propagation vector $k = (0.5\ 0.5\ 0.5)$ [46]. With an applied pressure of 2.8 GPa it undergoes a superconducting transition at very low temperatures $T_{SC} = 0.18$ K [47]. Shortly after unveiling superconductivity in $CeIn_3$, it was found superconductivity in cerium "115" materials and this topic remains an active area of research up to the present. The reason is that by adding a transition element to the unit cell, one has the additional opportunity to change the physical properties of the system. Especially in "115" compounds, exchanging cobalt with rhodium or iridium significantly changes the ground state properties.

$CeCoIn_5$ and $CeIrIn_5$ are well known heavy fermion superconductors with transition temperatures at $T_{SC} = 2.3$ K and 0.4 K respectively [48]. By contrast $CeRhIn_5$ orders antiferromagnetically at the Néel temperature $T_N = 3.8$ K and becomes superconducting with applied pressure $p = 1.63$ GPa at $T_{SC} = 2.2$ K [1]. It is believed, that significant increase of superconducting transition temperature in comparison with "13" compounds is caused by quasi two-dimensionality in the electronic states, which is related to their tetragonal structure [4].

The magnetic structure in $CeRhIn_5$ is incommensurate (IC) propagating with a wave vector $k = (0.5\ 0.5\ 0.297)$ and magnetic moments of $0.75\ \mu_B$ lying within *ab*-plane [49, 50]. The size of this moment gives a major part of the expected moment in the crystal-field doublet ground state ($0.92\ \mu_B$), which suggests $4f$-localized magnetism. Here the influence of neighbouring Ce layers is decreased leading to incommensurate propagation along c-axis. The other existing compounds from cerium "115" family do not exhibit magnetic order without applied magnetic field. By applying external magnetic field along c-axis in $CeCoIn_5$ there appears a so-called Q-phase with magnetic moments of $0.15\ \mu_B$ aligned along c-axis and propagating with wave-vector $k = (0.45\ 0.45\ 0.5)$ [51]. It is a question whether this magnetic ordering has origin in Fulde–Ferrell–Larkin–Ovchinnikov phase or not, see [4] and references therein for discussion.

Table 2 - Known magnetic structures for compounds from $\mathrm{Ce}_n T_m \mathrm{In}_{3n+2m}$ family.

Compound	Propagation	Direction	Size (μ_b)	T_N (K)	
$CeIn_3$ [46]	0.5 0.5 0.5		0.48	10	[1]
$CeRhIn_5$ [49, 50]	0.5 0.5 0.297	ab-plane	0.75	3.8	
$CeCoIn_5$ [51]	0.44 0.44 1/2	c-axis	0.15	0.3	[2]
$Ce_{0.95}Nd_{0.05}CoIn_5$ [52]	0.45 0.45 1/2			0.9	
Ce_2RhIn_8 [53]	0.5 0.5 0	52° from ab-plane	0.55	2.8	

All cerium "115" compounds have "218" relatives exhibiting nearly similar behaviour. Ce_2CoIn_8 undergoes superconducting state at $T_{SC} = 0.4$ K [54], which is significantly lower than its "115" relative. Superconductivity in Ce_2IrIn_8 has not yet been observed and it remains a heavy fermion paramagnet down to 50 mK [55]. The only magnetic cerium compound with "218" structure is Ce_2RhIn_8 having AF transition at $T_N = 2.8$ K. It exhibit magnetic order with commensurate propagation $k = (0.5\ 0.5\ 0)$ and staggered moment of $0.55\ \mu_B$ pointing $52°$ from ab-plane [53]. The moment stacking in the ab-plane layers of cerium remains the same as in $CeIn_3$, but moments stopped propagating along tetragonal c-axis. The recently discovered cerium based "218" compounds are Ce_2PdIn_8 and Ce_2PtIn_8 which have no "115" relatives. Ce_2PdIn_8 is a heavy-fermion superconductor in ambient pressure with $T_{SC} = 0.7$ K [56, 57]. The recent studies show a lot of similarities between this compound and well $CeCoIn_5$ [58]. Ce_2PtIn_8 seems to have antiferromagnetic behaviour with superconductivity under applied pressure, details will be published [59].

The recently discovered "127" compound $CePt_2In_7$ orders magnetically below $T_N = 5.5$ K, forming AF structure [60] with unknown microscopic details. It becomes superconducting under an applied pressure of 3.5 GPa and $T_{SC} = 2.1$ K. Up to now this is the only compound from "127" family [60].

---

[1] Magnetic moment direction cannot be determined by neutron diffraction.

[2] In the magnetic field 11 T applied along the [1-10] direction.

Cerium compounds don’t exist with X = Ga, while this structure is possible only for heavy rare-earth elements with gallium [61]. In summary, magnetic structures in cerium based compounds embody complex behaviour originated from a mixture of competing effects. The different sizes and directions of magnetic moments are summarized in Table 2.

3.3. Bulk properties

We will focus only on “13”, “115” and “218” families, as they are investigated much more than others and allow us to follow some general trends. Bulk properties of all these groups can be summarized as follows:

La, Lu and Y samples are always non-magnetic because their 4*f* shells are full/empty. This makes them ideal candidates for reference measurement, for example of phonon spectra. Pr and Yb compounds generally possess no magnetic ordering and remains paramagnetic down to the milikelvin temperature range. The Pm compound was never reported and also europium ones seem to not exists. However, there exists one study on $EuIn_3$ [62], but the existence of this compound is in contradiction with published In-Eu binary phase diagrams. The rest of compounds order AF and can be split into three groups based on the direction of the easy magnetization axis. Generally compounds with Gd and Sm are nearly isotropic, compounds with R = Nd, Tb, Dy, Ho have an easy magnetization axis along the tetragonal *c*-axis, and compounds with Er and Tm have easy magnetization axis lying within the *ab*-plane.

It is possible to exchange In with Ga in “115” and “218” compounds if the R ion belongs to heavy rare-earth elements (Gd-Yb). These intermetallics have similar properties as their indium relatives.

It is interesting to follow evolution of Néel temperature with changing dimensionality. The most complete study was done on “13” and rhodium “115” compounds (detailed description of rhodium “115” family is given in Hieu’s thesis [6]) where all Néel temperatures are known. They are summarized in Table 3. While “13” compounds follow de Gennes scaling on T_N [6], in case of “115” and “218” compounds Gd compound deviates from this behaviour. Namely, the Néel temperature of the gadolinium compound is smaller than in the terbium one.

Table 3 - Néel temperatures for rhodium based “13”, “115” and “218” compounds

R	T_N (K) of $R\mathrm{In}_3$	T_N (K) of $R\mathrm{RhIn}_5$	T_N (K) of $R_2\mathrm{RhIn}_8$
Ce	10 [46]	3.8 [49, 50]	2.8 [53]
Nd	4.9, 5.3, 5.9 [63]	11 [64]	10.7 [65]
Sm	16 [66]	8, 15.3 [6]	15 [67]
Gd	44 [68]	39 [69]	40 [67]
Tb	32 [70]	47.3 [71]	43 [72]
Dy	7.9 [73]	28.1 [6]	
Ho	11 [70]	15.8 [6]	
Er	4.8 [74]	2.9, 4.2 [6]	
Tm	1.6 [75]	3.6 [6]	

Studies of the “218” family are not yet completed as seen from Table 3. As it is a main topic of this thesis, let us shortly summarize known results: $\mathrm{Pr_2RhIn_8}$ remains paramagnetic down to low temperatures [76], $\mathrm{Nd_2RhIn_8}$ orders antiferromagnetically below T_N = 10.7 K [65] and is the only compound from this series in which field-induced transition to another antiferromagnetic phase was reported [77]. Antiferromagnetic order was found also in $\mathrm{Sm_2RhIn_8}$ ($T_N =$ 15 K) [67], $\mathrm{Gd_2RhIn_8}$ ($T_N = 40$ K) [67] and $\mathrm{Tb_2RhIn_8}$ ($T_N = 42.8$ K) [72].

3.4. Magnetic structures

Although there exist a lot of compounds with “115” and “218” structures, the magnetic structures were microscopically studied only in those with T = Rh, X = In, then in T = Co, X = Ga and also in $\mathrm{Sm_2IrIn_8}$. These non-cerium compounds often follow the microscopic RKKY interaction, crystalline electrical field (CEF) effects, and the hybridization between $4f$-electrons and conduction electrons [78]. All presently known magnetic structures with corresponding references are summarized in Table 4.

Table 4 - Known magnetic structures of non-cerium compounds from $R_nT_mX_{3n+2m}$ family.

compound	propagation	direction	Size (μ_b)	T_N (K)	
		"13" structures			
NdIn$_3$ [63]	(½, ½, 0)	c-axis	2	5.9	[3]
GdIn$_3$ [68]	(½, ½, 0)	c-axis		44	
TbIn$_3$ [70]	(½, ½, 0)	10° from c-axis	8.4	32	
DyIn$_3$ [73]	(½, ½, 0)	27° from c-axis	8.8	24	
HoIn$_3$ [70]	(½, ½, 0)	58° from c-axis	9	7.9	
ErIn$_3$ [74]	(½, ½, 0)	[1 1 1]		4.8	
TmIn$_3$ [75]	(½, ½, 0)	[1 1 1]	4.89	1.6	[4]
		"115" structures			
NdRhIn$_5$ [64]	(½, 0, ½)	c-axis	2.5	11	
GdRhIn$_5$ [69]	(½, 0, ½)	b-axis		39	
TbRhIn$_5$ [71]	(½, 0, ½)	c-axis	9.5	47.3	
DyRhIn$_5$ [6]	(½, 0, ½)	c-axis		28.1	
HoRhIn$_5$ [6]	(½, 0, ½)	c-axis		15.8	
TbCoGa$_5$ [79]	(½, 0, ½)	c-axis		36.2	[5]
HoCoGa$_5$ [80]	(½, 0, ½)	c-axis		9.7	[6]
		"218" structures			
Tb$_2$RhIn$_8$ [72]	(½, ½, ½)			42.8	
Gd$_2$RhIn$_8$ [81]	(½, 0, 0)	ab-plane		40.8	
Sm$_2$IrIn8 [82]	(½, 0, 0)	ab-plane		14.2	[7]
Gd$_2$CoGa$_8$ [83]	(½, ½, ½)	ab-plane		20.0	
Tb$_2$CoGa$_8$ [83]	(½, ½, ½)	c-axis		28.5	
Dy$_2$CoGa$_8$ [83]	(½, ½, ½)	c-axis		15.2	
Ho$_2$CoGa$_8$ [78]	(½, ½, ½)	c-axis		5.1	
Er$_2$CoGa$_8$ [61]	(0, ½, 0)	a-axis	4.71	3	
Tm$_2$CoGa$_8$ [61]	(½, 0, ½)	a-axis	2.35	2	

---

[3] This C structure is stabilized below 4.7 K. Above this temperature there is a mixture of IC phases.

[4] Compound also reveals (0, 0, ½) propagation and IC structure.

[5] Magnetic structure for phase between 5.4 and 36.2 K.

[6] This C structure is stabilized below 7.4 K. Between this temperature and T_N exists IC phase with $k = (0.5, 0, 0.359)$.

[7] Direction of the moments was determined to be 18° from a-axis.

4. Results and discussion

As stated in the introduction, our experimental work will be focused on the non-reported members of 218 family with T = Rh and X = In. We will start with sample preparation, bulk properties measurement and finally microscopic magnetic structure determination by means of neutron diffraction.

4.1. Sample preparation

Single crystals of R_2RhIn$_8$ were prepared by the solution growth method from an indium flux with starting compositions around 2:1:40 (R:Rh:In). The elements were put into alumina crucibles, sealed under high vacuum and heated up to 910-950 °C. The samples were then slowly cooled (2 °C/h) to 400 °C where the remaining indium solution was centrifuged. In this way, plate-shaped cuboid single crystals were obtained, always with the *c*-axis axis oriented perpendicular to the plate and the *a*-axis parallel with the side of the cuboid. All prepared final samples (which were used for further measurement) are listed in Table 5.

Table 5 - Prepared samples of R_2RhIn$_8$

Compound	Starting composition	Weight (mg)	$a \times b \times c$ (mm)
Y_2RhIn$_8$	2:1:40	7	$2 \times 1 \times 0.4$
La$_2$RhIn$_8$	2:1:40	16	$3 \times 2.5 \times 0.4$
Nd$_2$RhIn$_8$	2:1:40	13.5	$1.7 \times 1.5 \times 0.8$
Tb$_2$RhIn$_8$	2:1:30	3.8	$2 \times 0.7 \times 0.3$
Dy$_2$RhIn$_8$	2:1:30	3.5	$2.5 \times 0.4 \times 0.4$
Ho$_2$RhIn$_8$	2:1:30	5.2	$3 \times 1 \times 0.2$
Er$_2$RhIn$_8$	2:1:50	7.2	$4 \times 1.5 \times 0.2$
Tm$_2$RhIn$_8$	2:1:25	4.4	$1.5 \times 1.5 \times 0.2$
Lu$_2$RhIn$_8$	2:1:40	4	$2 \times 0.7 \times 0.3$

The chemical composition and homogeneity were verified by an energy-dispersive X-ray detector (EDX) Bruker AXS.

4.2. Nonmagnetic compounds

As stated in chapter 2.2.1, phonon contributions are an important part of the whole measured specific heat. As our compounds contain a lot of atoms in the unit cell (11), the experimental determination of the phonon branches is difficult. This is the main reason why we started our bulk measurements with determination of specific heat of all possible non-magnetic R_2RhIn$_8$ compounds (R = Y, La, Lu), where only electronic and phonon contributions are taking effect.

Lanthanum and Yttrium compounds are already known to crystallize in correct tetragonal Ho$_2$CoGa$_8$-type structure, space group P4/mmm [67, 72] and Lu$_2$RhIn$_8$ was not reported before. The lattice parameters of the investigated single crystals were determined from single crystal X-ray RIGAKU RAPID II diffractometer. The specific heat was measured using the Quantum Design PPMS in the temperature range between 1.8 K and 300 K; in case of Lu$_2$RhIn$_8$ down to 0.4 K. Samples stated in Table 5 were used.

The X-ray analysis revealed all compounds to be single crystals with the tetragonal structure and P4/mmm space group. The observed lattice parameters, listed in the Table 6, follow the usual lanthanide contraction with parameters of Y$_2$RhIn$_8$ placed close to those of Tb$_2$RhIn$_8$ (see chapter 4.3.1). Comparing La$_2$RhIn$_8$ and Lu$_2$RhIn$_8$, the change of c parameter is larger than the change of a and the c/a ratios has thus maximum value for La$_2$RhIn$_8$.

There are three atomic position parameters which are not fixed by symmetry for the Ho$_2$CoGa$_8$-type crystal structure (listed at the bottom of the table). The

Table 6 - Structural parameters of studied compounds.

	Y$_2$RhIn$_8$	La$_2$RhIn$_8$	Lu$_2$RhIn$_8$
a (pm)	460.7	469.8	455.4
c (pm)	1201.7	1234.4	1185.3
c/a	2.608	2.628	2.603
$V_{f.u.}$ (nm^3)	0.255	0.272	0.246
z_R	0.3077	0.3049	0.3090
z_{In2}	0.3085	0.3069	0.3094
z_{In3}	0.1230	0.1181	0.1252

indium positions are denoted in a usual way, i.e. In1 at 2e, In2 at 2h and In3 at 4i crystallographic site. These parameters were calculated by Dr. Diviš using first-principles calculations based on density-functional theory.

4.2.1. Specific heat analysis

The specific heat of the studied compounds, shown in Figure 10, consists only from the electronic and the phonon contributions and all are non-magnetic. The phonon spectrum of the R_2RhIn_8 compounds splits in general to 3 acoustic and 30 optic branches. In pursuit of finding suitable expression for C_{ph}, we applied the Debye model to the three acoustic branches and the Einstein model to the optic branches, described by equation (9).

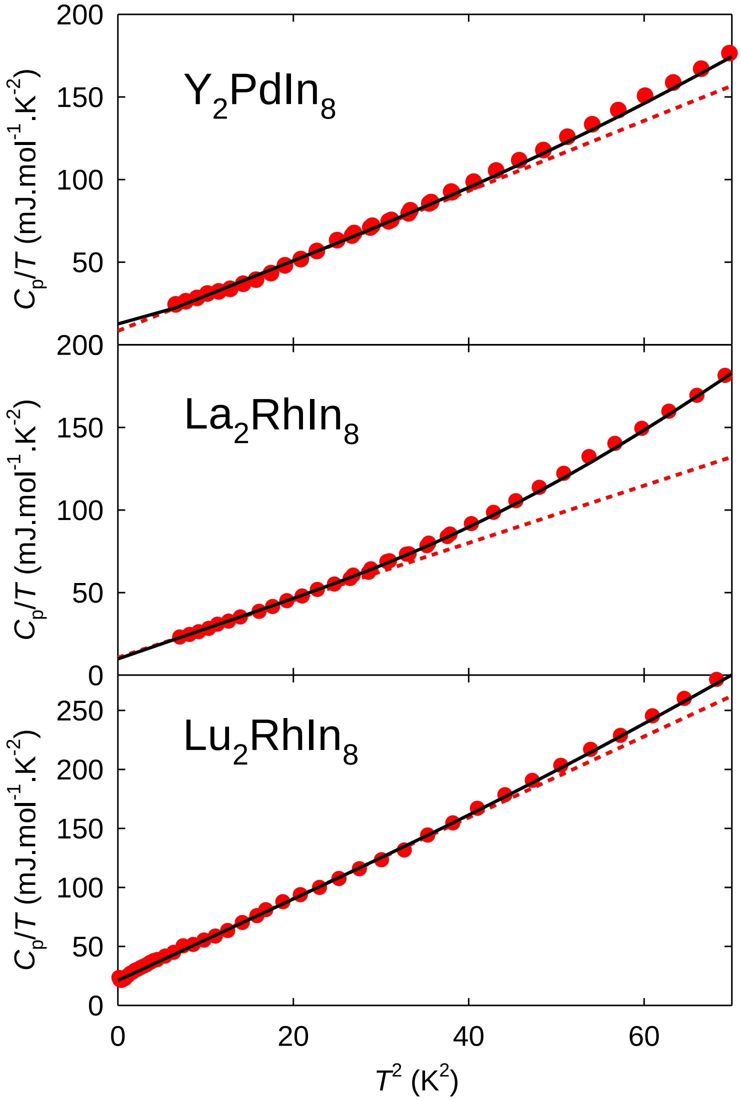

Figure 9 - Low temperature specific heat of studied compounds. Dashed lines are results of fitting equation (9) and solid lines are results of overall fitting which includes additionally the optic phonons as described by equation (10)

The measured low-temperature data are shown in Figure 9 in the C_p/T vs T^2 representation. The data for Lu_2RhIn_8 considerably exceeds the specific heat of the other two compounds at low temperatures. Therefore, to exclude some experimental error, we have performed additional independent measurement of Lu_2RhIn_8 down to 0.4 K. The new set of data confirmed this unexpected behaviour as seen in Figure 9.

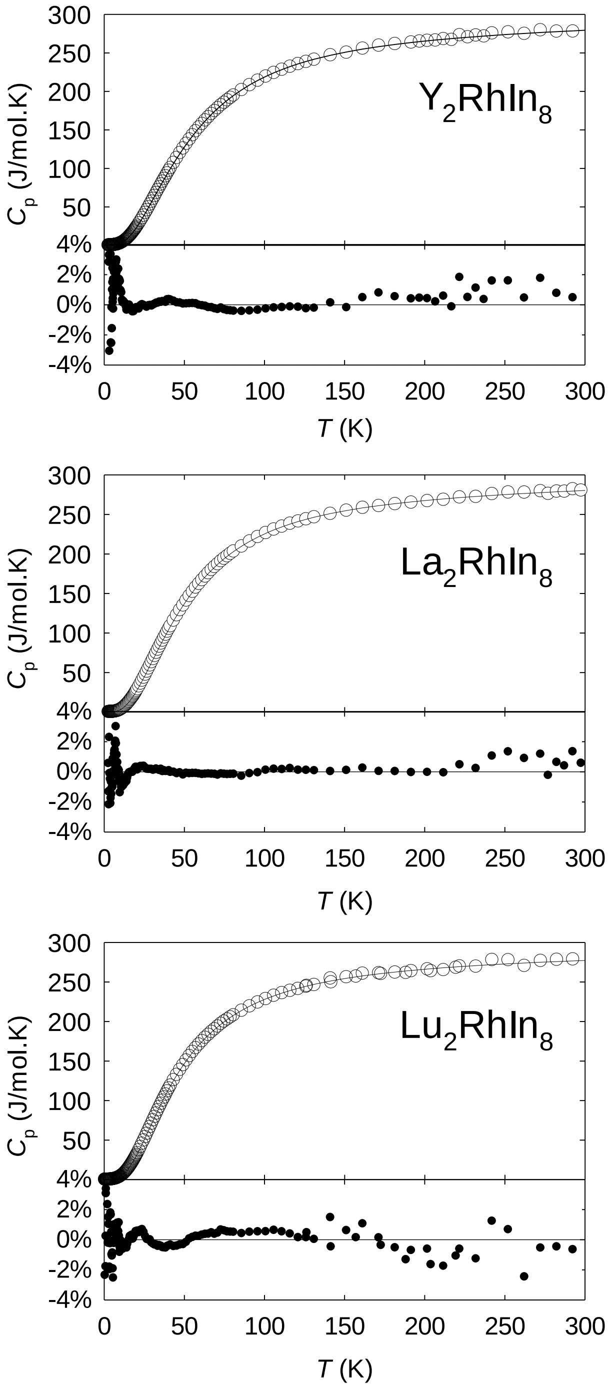

Figure 10 - The experimental specific heat, solid lines represent curves calculated using parameters from Table 7. Proportional residues after subtracting calculated values $\frac{(C_{meas}-C_{calc})}{C_{calc}} \times 100$ % are below each graph.

We also observe clear deviation from linearity already at relatively low temperatures above 5 K in all three compounds. The non-linear increase of C_p/T indicates presence of the low energy optic phonons. Therefore, equation (10) should be considered with care and applied at the lowest temperatures only. We fit our data by the equation (10) considering only the linear part of the C_p/T vs T^2 plot up to 5 K. In this way, the γ coefficients and the Debye temperatures were determined and are listed in Table 7. The corresponding fit is drawn in Figure 9. We stress that the θ_D values here characterize just the three acoustic branches of each compound. The determined θ_D compare well with the energies of the acoustic phonons found for $UCoGa_5$ [84], which crystallize in a related tetragonal structure.

In the second step, we tried to describe the measured data from the whole temperature region using the non-linear fitting of expression (9) with fixed electron contribution and fixed Debye temperature describing the three acoustic branches. In the case of compounds with 30 optic branches, the number of free parameters is too large to get any final unambiguous solution. Therefore, we reduced the number of parameters to some acceptable minimum with the aim to describe the main features of the phonon spectra and reproduce well the measured data, so that the model could serve as an estimation of the non-magnetic contribution in magnetic R_2RhIn_8 compounds. To simplify the model, we grouped the optic modes to threefold degenerated branches. It is quite a natural assumption and signs of such a scheme can be traced out also in results of the first-principles calculations of $PuCoGa_5$ [85].

By testing several different degeneracy models, we finally used three parameters θ_{E1}, θ_{E2} and θ_{E3} and one overall anharmonic coefficient α for the Yttrium and Lanthanum compound, while for the Lutetium one it is better to add another Einstein branch (θ_{E4}).

For all compounds the lowest energy level θ_{E1} describes 3 degenerated branches. The results are summarized in the Table 7. Please note that the given Debye temperatures describes just the three acoustic phonon branches and cannot thus be compared e.g. with substantially higher values given for La_2RhIn_8, Ce_2RhIn_8 [86] or Ce_2PdIn_8 [87] which were derived to describe the whole phonon spectrum of 33 branches in the whole temperature region up to 300 K. We believe that our approach with θ_D describing only the acoustic phonons better reflects the real phonon dispersions.

We are aware that our overall approach with a given number of θ_E parameters is only a model still far from complex reality, but it can be well used for estimation of the phonon specific heat for isostructural magnetic compounds. The main feature is nevertheless indisputable: the very low energies of lattice vibrations in these compounds. To demonstrate quality of the fit the residuals from fitting C_p/T are shown in Figure 10.

The slightly enhanced relative deviations in the low temperature region below 6 K are caused mainly due to a relatively small heat capacity of the samples at these temperatures and the instrumental accuracy. The difference between the measured and calculated values remains below ~ 3% in the whole temperature region, which is comparable with the overall instrumental accuracy [88].

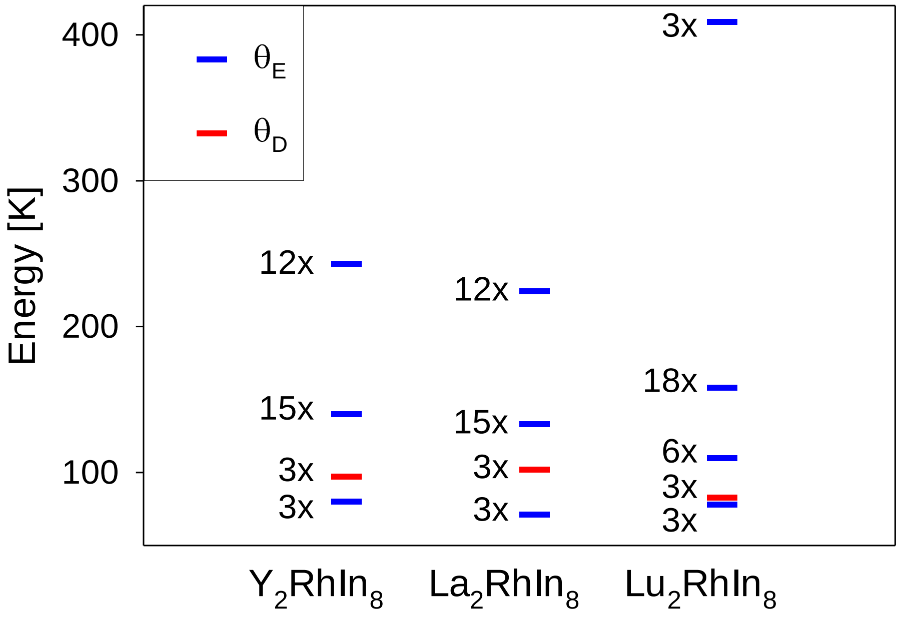

Figure 11 - Graphical representation of determined energy levels of optical (blue) and acoustic (red) branches.

The θ_D and θ_E values depend generally on the atomic masses and interatomic distances. The mass dependence can qualitatively account for lower θ_D in Lu compound compared to the Y and La counterparts, but comparison of Y_2RhIn_8 and La_2RhIn_8 contradicts the expected mass dependence. Also the comparison of the characteristic energies of the optical branches implies a larger importance of the interatomic distances than the atomic masses. Y_2RhIn_8 and La_2RhIn_8 show very similar overall phonon dispersions which probably reflects opposite effect of atomic masses and interatomic distances. In all compounds, the optic phonon levels lie anomalously low and the derived data imply crossing of the optic and acoustic branches in their dispersion relation. This behaviour is in accordance with the detailed phonon spectra for the related system $UCoGa_5$, as presented in reference [84]. The quantitative comparison of our present study with the results reported for $UCoGa_5$ [84] and $PuCoGa_5$ [85] indicates that the optic phonon energies are probably somewhat lower in R_2RhIn_8 compounds than in the two mentioned compounds. Unfortunately, to the best of our knowledge there is no study of phonon spectra for the lanthanide based compounds which could serve for more pertinent comparison with our results.

Table 7 - Parameters characterizing the specific heat. The listed Einstein and Debye temperatures describe the number of phonon branches given before the value.

	Y_2RhIn_8	La_2RhIn_8	Lu_2RhIn_8
γ $(\mathrm{mJ.mol^{-1}.K^{-2}})$	8.4	9.9	21.1
θ_D (K)	3x 97	3x 102	3x 83
θ_{E1} (K)	3x 80	3x 71	3x 78
θ_{E2} (K)	15x 140	15x 133	6x 110
θ_{E3} (K)	12x 243	12x 224	18x 158
θ_{E4} (K)			3x 409
α $(\mathrm{K^{-1}})$	1×10^{-4}	1×10^{-4}	1×10^{-4}

4.3. Bulk properties of magnetic compounds

In this chapter, we present detailed analysis of crystal structure and low temperature bulk properties of R_2RhIn_8 compounds for R = Tb, Dy, Ho, Er and Tm. Based on the magnetization and the specific heat measurements on single crystals, we determined the easy magnetization directions and the magnetic phase diagrams, which are prerequisites for further microscopic studies.

4.3.1. Structure characterization

The structural lattice parameters of investigated single crystals were determined from single crystal X-ray diffraction experiment. The X-ray analysis confirmed that all investigated R_2RhIn_8 compounds maintain the tetragonal Ho_2CoGa_8-type structure. Both the lattice parameters and the cell volume decreases with increasing atomic number of the rare-earth element according to the lanthanide contraction (see Figure 12). All the determined structural parameters are summarized in Table 8.

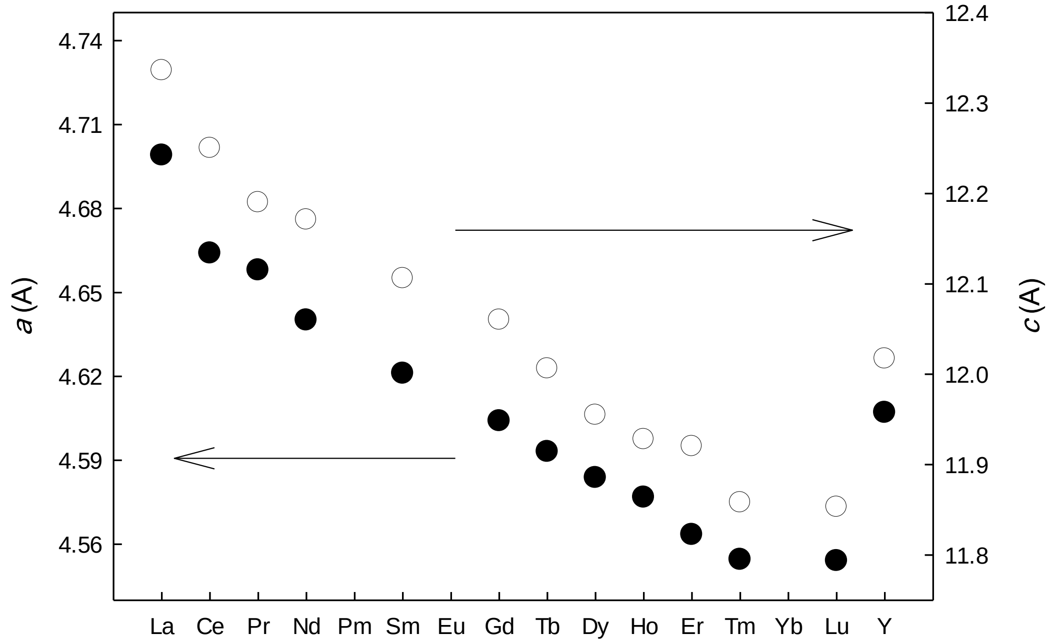

Figure 12 - Lattice parameters in the R_2RhIn$_8$ compounds. Beside our data, we use the data published in [89, 90, 65, 67]

4.3.2. Specific heat

The specific heat was measured by the relaxation method using the Quantum Design PPMS 9 T and 14 T systems in the temperature range between 1.8 K and 300 K in magnetic fields up to 14 T.

Table 8 - Parameters of compounds along the series

	a (Å)	c (Å)	V (Å^3)	T_N (K)	$m_{14\mathrm{T}}$ (μ_B)
Tb_2RhIn_8	4.593(3)	12.006(5)	55.144	43.6(3)	15.7(1)[8]
Dy_2RhIn_8	4.584(3)	11.955(6)	54.797	25.1(2)	15.7(1)
Ho_2RhIn_8	4.577(2)	11.928(9)	54.590	10.9(2)	17.0(1)
Er_2RhIn_8	4.563(4)	11.920(5)	54.396	3.8(1)	17.1(2)
Tm_2RhIn_8	4.555(2)	11.858(7)	54.007	4.1(2)	12.9(1) [9]

---

[8] $m_{60\mathrm{T}}$

[9] $m_{9\mathrm{T}}$

The temperature dependence of the specific heat of all studied compounds is represented in Figure 13 and Figure 14. In zero magnetic field, one anomaly is observed for each compound, except for Ho_2RhIn_8 showing two close anomalies which will be discussed later. The shape of the anomalies in all compounds is typical for a second-order phase transition, in our case between paramagnetic and antiferromagnetic state. The idealization of the specific-heat jump under the constraint of entropy conservation yields the Néel temperatures summarized in Table 8. The Néel temperature of Tb_2RhIn_8 determined as 43.6 K is roughly in agreement with $T_N = 42.7$ K reported by Serrano [72]. Evolution of the Néel temperature along the R_2RhIn_8 series, including previously published results for R = Nd, Sm and Gd [77, 67], follows approximately the de Gennes scaling as shown on Figure 15. The biggest difference from theoretical de Gennes values is for Gd compound which T_N is below transition temperature of Tb_2RhIn_8.

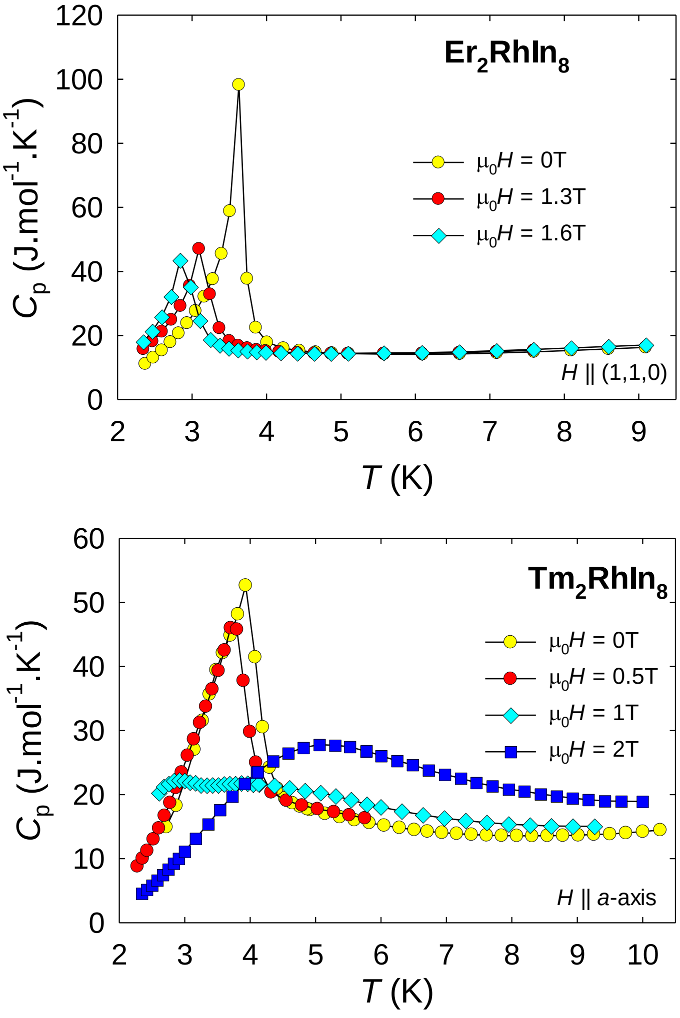

Figure 13 - The specific heat of the R_2RhIn_8 compounds with easy magnetization axis within *ab*-plane. The applied magnetic field is along *a*-axis.

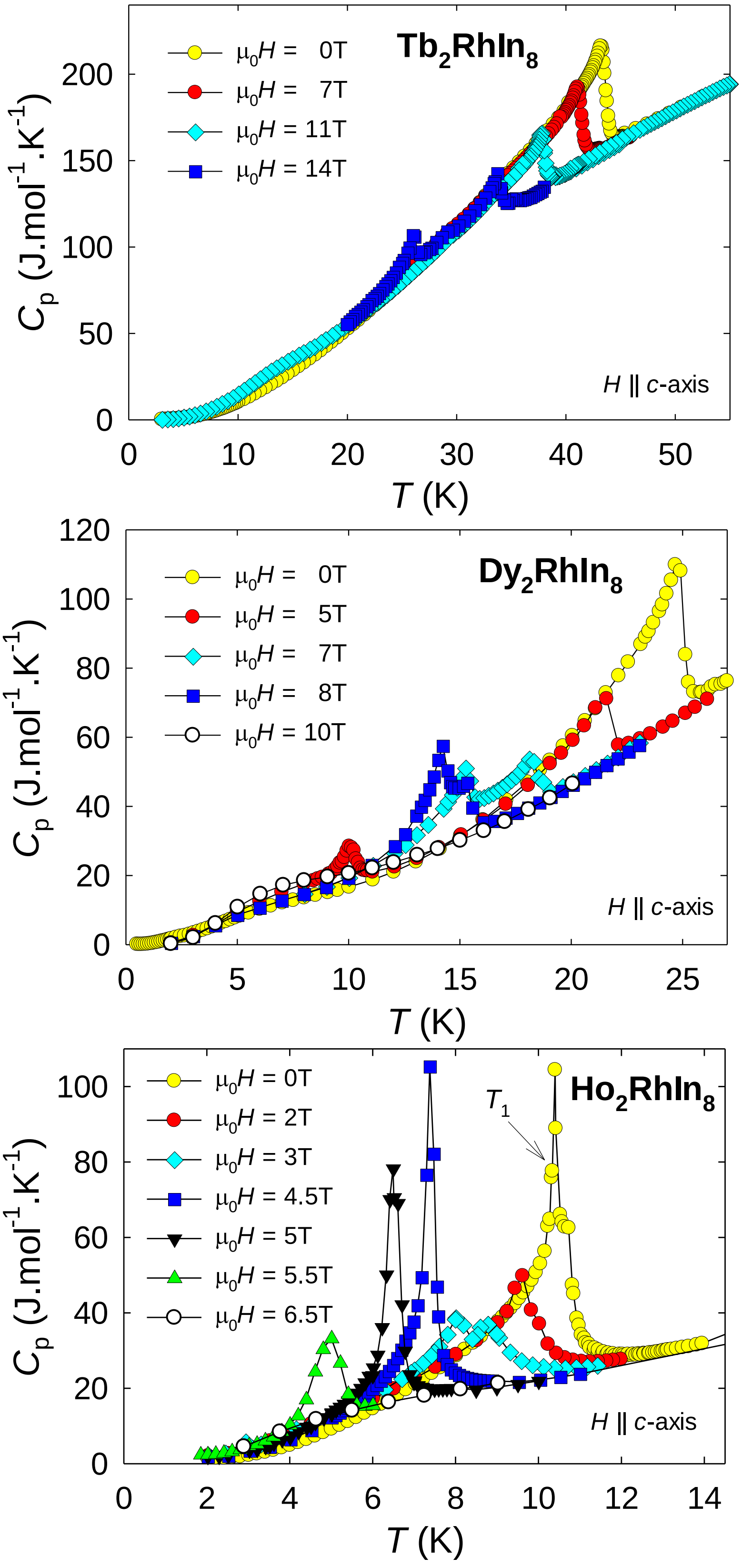

Figure 14 - The specific heat of the R_2RhIn$_8$ compounds with easy magnetization axis along *c*-axis in the low temperature region. The applied magnetic field is along this direction.

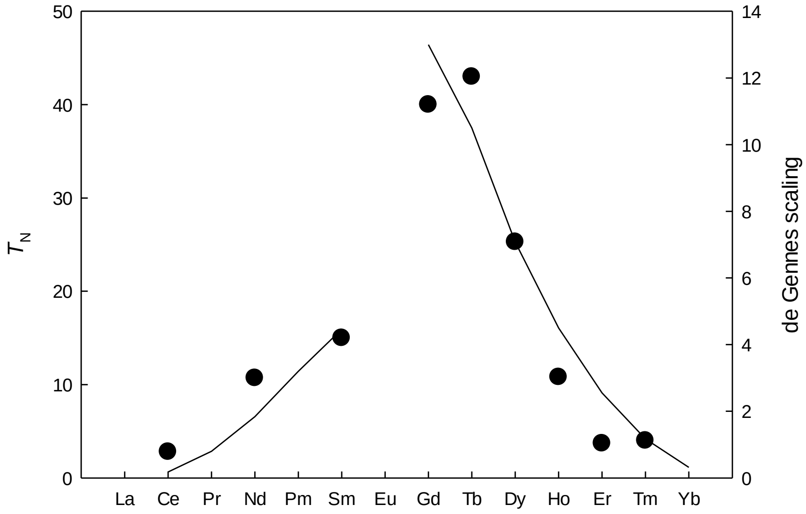

Figure 15 – Evolution of Néel temperatures along the R_2RhIn$_8$ series. The solid line corresponds to De Gennes scaling.

4.3.3. Magnetization

The magnetization was measured on the PPMS instrument using a Vibrating Sample Magnetometer. Magnetization measurements were done between 1.8 K and 300 K in external magnetic fields up to 14 T applied along different crystallographic directions of measured single crystals. The measured magnetization curves were corrected for the demagnetization field reflecting the sample shape of each sample.

Magnetization curves measured with field applied along various crystallographic directions are shown on Figure 16 for compounds with easy axis along tetragonal *c*-axis and on Figure 17 for Er and Tm where the easy magnetization axis lies within *ab*-plane. The magnetization curves measured at 2 K (5 K for Tb$_2$RhIn$_8$) reveal the largest anisotropy in Tb$_2$RhIn$_8$ with the anisotropy field estimated to 60 T, considering further metamagnetic transition for $H \parallel c$. To clarify this expectation, high field experiment on the terbium compound was performed. Data were measured on the same sample at T = 1.5 K in pulsed magnetic fields up to 60 T (pulse duration 20 ms) at the High-field Laboratory in Dresden-Rossendorf by Prof. Andreev. An induction method using a coaxial pick-up coil system was used to carry out the measurement. A detailed description of the high-field magnetometer is described in [91]. The measured high-field data together with data from PPMS system are plotted in the Figure 18.

The difference of anisotropy direction in compounds containing different rare-earth ions is probably governed by the sign of the second order Stevens constant α_j which is positive for Er and Tm and negative for Tb, Dy and Ho. Similar relation between the easy magnetization direction and the rare-earth element was found in the isostructural R_2CoGa$_8$ compounds [92] and many other tetragonal systems including e.g. RRhIn$_5$ [93]. In analogy to our results on Er$_2$RhIn$_8$, Er$_2$CoGa$_8$ also shows a rather weak anisotropy and the determined crystal field parameters indicate that the compound is on the border line of a magnetic anisotropy crossover [92].

Compounds of the first group (R = Tb, Dy and Ho) exhibit rather similar magnetic behaviour. The most remarkable common feature is the existence of two metamagnetic transitions when the field is applied along the *c*-axis. Both transitions are seen as sharp steps in the $M(H)$ curve measured at 2 K for Dy$_2$RhIn$_8$ and Ho$_2$RhIn$_8$, or 1.5K in pulsed field for Tb$_2$RhIn$_8$. The first one corresponds to transition to some intermediate magnetic phase (AF2) in which the sum of magnetic moments equals exactly one half of the total moment in the ferromagnetic state. As there are two crystallographic *ab*-planes containing rare earth atoms in the unit cell of the Ho$_2$CoGa$_8$-type structure (see Figure 7), it supports the idea that the moments couple antiferromagnetically within one of the planes and ferromagnetically within the other one. A similar hypothesis with a sequence of ferromagnetic and antiferromagnetic (100) or (110) planes is discussed by Hieu et al. [94] for RRhIn$_5$ series which exhibit the same two-step magnetization curves. Such magnetic coupling, however, seems quite unusual because all the rare earth sites are crystallographically equivalent. For further understanding of the microscopic details of this field-induced transition, neutron experiment in applied magnetic field is desirable. See chapter 4.4.4 for such experiments.

The second transition in this compounds leads to the ferromagnetic state. Certain differences between the value of magnetization measured in 14 T (see Table 8) and the full R^{3+} free ion moments is presumably due to the crystal field effects. A similar effect is observed in related “115” compounds [6]. Both metamagnetic transitions become less sharp with increasing the temperature as shown for Ho$_2$RhIn$_8$ in Figure 16. Pulsed field experiment confirmed similar behaviour also in the Tb compound.

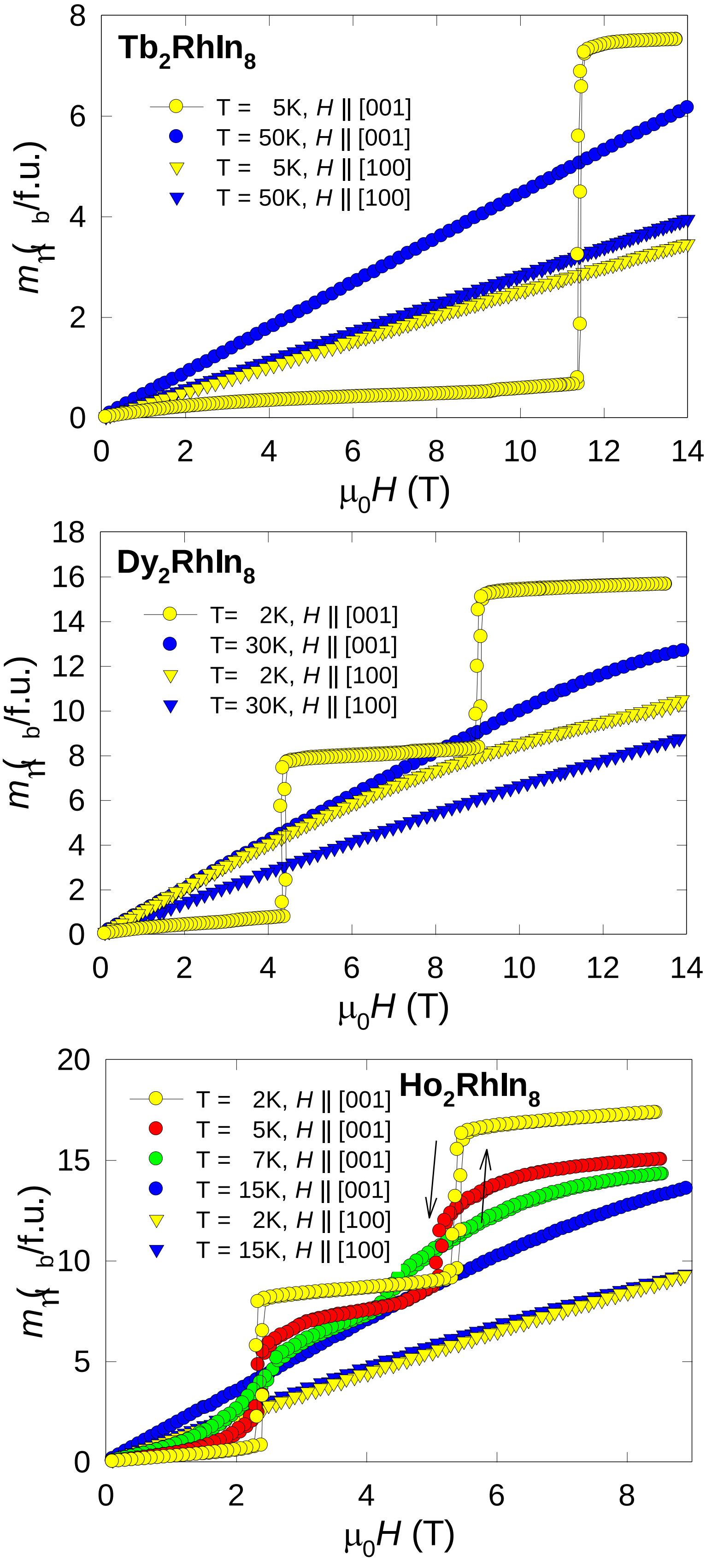

Figure 16 - Magnetization curves of Tb_2RhIn_8, Dy_2RhIn_8 and Ho_2RhIn_8 compounds measured for magnetic field applied along tetragonal *c*-axis at several representative temperatures.

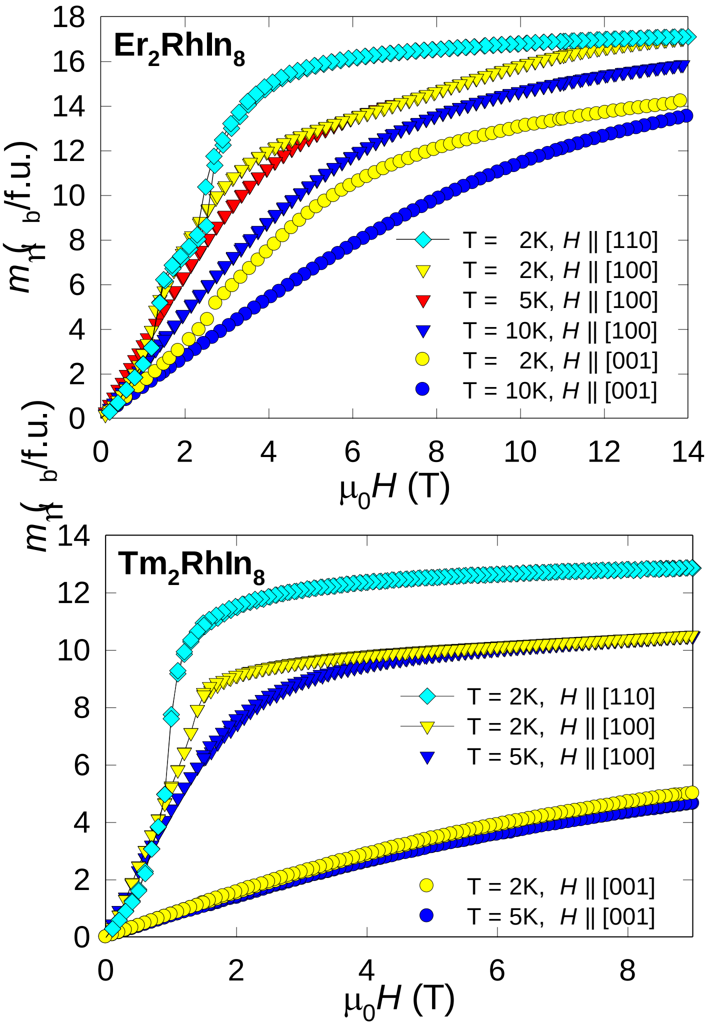

Figure 17 - Magnetization curves of Er_2RhIn_8 and Tm_2RhIn_8 compounds.

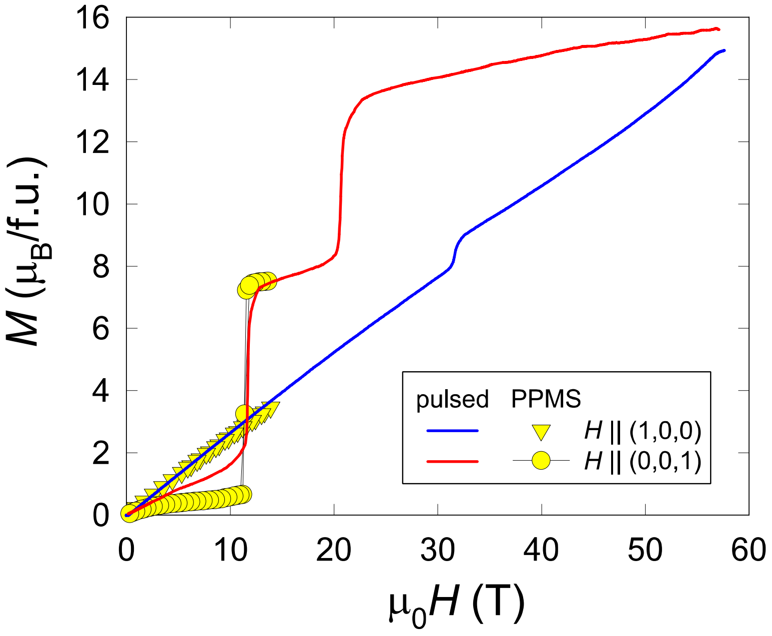

Figure 18 - Magnetization curves measured along the main crystallographic axes of the Tb_2RhIn_8 single crystal. Data obtained from pulsed source (lines) were compared to the data measured by PPMS (yellow points).

4.3.4. Phase diagrams

The derivative of the $M(H)$ curves measured at different temperatures and $M(T)$ dependencies measured in different fields were inspected to construct the magnetic phase diagrams for the field applied along the c-axis. The points obtained as maxima of these derivatives are represented as circles in Figure 19. The vertical and horizontal error bars correspond to the $M(H)$ and $M(T)$ dependencies. The intermediate magnetic phase is labeled as AF2 in Figure 19, following the notation introduced for RRhIn$_5$ compounds [94]. The critical fields of the phase transitions at 2 K amount to 2.5 T and 5.8 T for Ho$_2$RhIn$_8$, 4.3 T and 9.5 T for Dy$_2$RhIn$_8$ and 11.7 T and 20.7 T for Tb$_2$RhIn$_8$.

To reveal more details of the magnetic phase diagrams, the specific heat was measured in different magnetic fields applied along the easy magnetization direction, i.e. along the c-axis for Tb$_2$RhIn$_8$, Dy$_2$RhIn$_8$ and Ho$_2$RhIn$_8$. The representative data are shown in Figure 14.

First, we observe a gradual shift of the transition temperature with increasing field as expected for an antiferromagnetic state. Two clear anomalies can be then distinguished for a certain field range, corresponding to T_N and AF1-AF2 transition. Both transitions are well seen e.g. in the 14 T curve of Tb$_2$RhIn$_8$ or the 3 T curve of Ho$_2$RhIn$_8$. With further increasing the field, a single anomaly is observed again as seen well in the Ho$_2$RhIn$_8$ case. The very broad anomaly observed for Tb$_2$RhIn$_8$ in 11 T between 10 and 20 K could be related to fact that the measurement is close and parallel to the AF1-AF2 magnetic phase borderline. The phase transition temperatures obtained from all the measured $C_p(T)$ dependencies are in a good agreement with the magnetization data and represented as triangles in Figure 19.

As already mentioned above, Ho$_2$RhIn$_8$ represents certain exception when showing two sharp anomalies at $T_N = 10.9(2)$ K and $T_1 = 10.4(1)$ K in the specific heat measured in zero field. One can first consider presence of HoIn$_3$ phase grown inside the Ho$_2$RhIn$_8$ crystal typical for some R$_2$TX$_8$ compounds [95]. The magnetic properties of HoIn$_3$ are somewhat contradictory: the specific heat shows a well pronounced anomaly at $T_N = 7.9$ K [96], whereas the former susceptibility measurements indicate $T_N = 11$ K [66]. The result from susceptibility might eventually explain the anomaly observed in our data. To fully clarify phase purity of this single crystal, Laue diffraction experiment is needed (see Chapter 4.4.1).

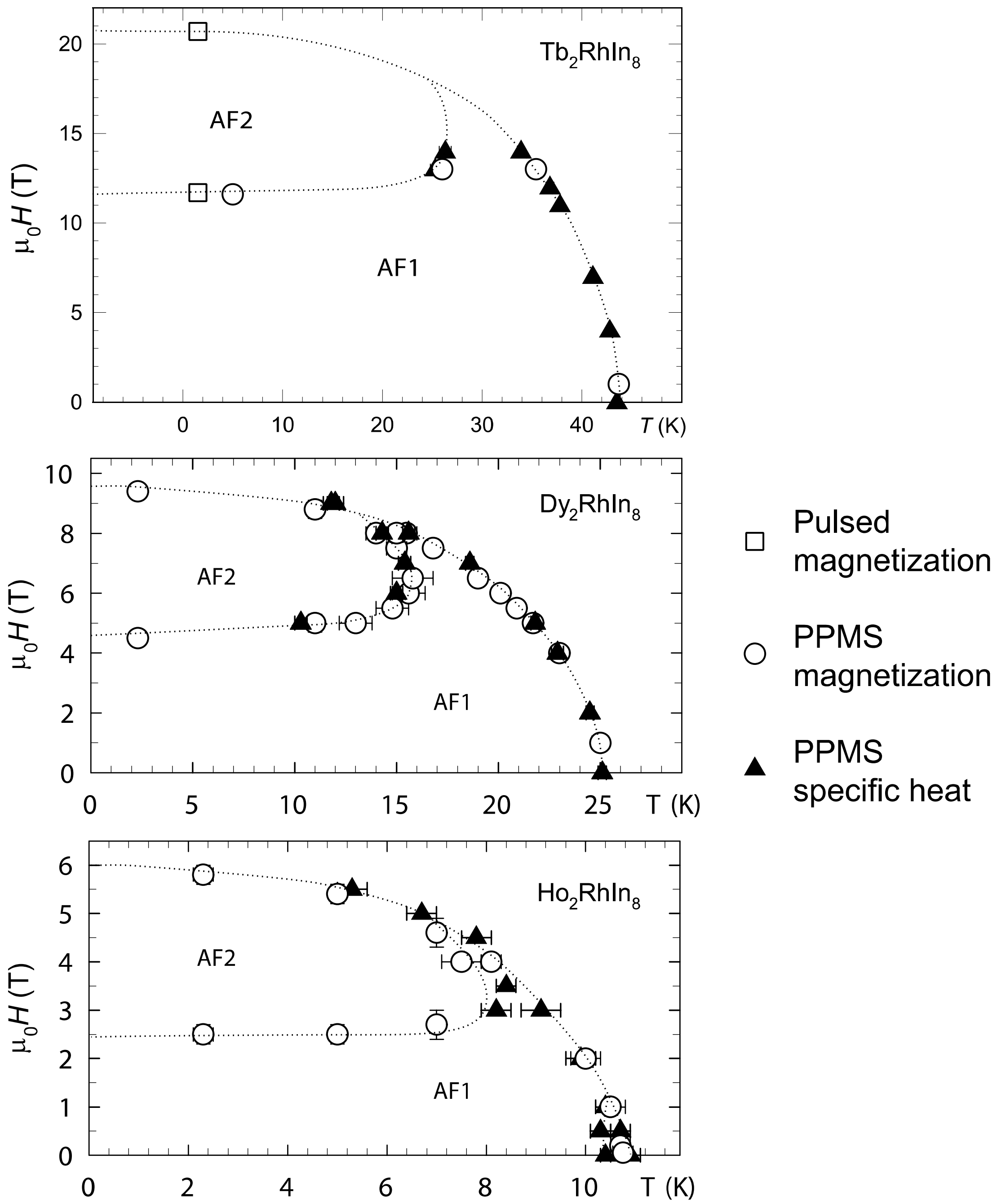

Figure 19 - Magnetic phase diagrams of Tb_2RhIn_8, Dy_2RhIn_8 and Ho_2RhIn_8 compounds. Data were determined from both specific heat and magnetization measurements (pulsed and PPMS). The lines are drawn to guide the eye.

Another explanation is the existence of further magnetic phase AF3 in a very narrow temperature region between T_N and T_1. Ho_2RhIn_8 would be then the first compound showing this phase among all RTX_5 and R_2TX_8 studied up to now. One can consider e.g. some incommensurate propagation along the *c*-axis in this phase before going to simple antiferromagnetic phase below T_1. Such magnetic structures were observed in several tetragonal systems such as e.g. UNi_2Si_2, UCu_2Si_2 [97, 98].

The transition to the ferromagnetic state occurs in Er_2RhIn_8 and Tm_2RhIn_8 in relatively low magnetic fields around 2.5 T and 1.0 T, respectively. The specific heat data are consistent with the antiferromagnetic order showing gradual decrease of T_N when increasing applied external field. Above the critical field, the specific heat anomaly broadens significantly and the magnetic entropy shifts to higher temperatures as expected for a field-induced ferromagnetic state (see the 2 T curve for Tm_2RhIn_8).

Despite the identical moment direction, the magnetic phase diagram of Er_2RhIn_8 and Tm_2RhIn_8 are different. The behaviour of Tm_2RhIn_8 is characterized by a single antiferromagnetic phase below T_N, whereas the magnetization curve of Er_2RhIn_8 reveals an additional metamagnetic transition in field around 1.4 T applied along the [110] direction. This indicates existence of another magnetic phase that exists between 1.4 and 2.5 T at 2 K. This can give us a cue for determination of magnetic structures and that the microscopical character of these two compounds will be different.

4.3.5. Comparison with “115” and related “218” compounds

The magnetic phase diagrams of Tb_2RhIn_8, Dy_2RhIn_8 and Ho_2RhIn_8 for $H \parallel c$, constructed on the basis of magnetization and specific heat measurements, shown in Figure 19, have similar character with two magnetic phases beside the paramagnetic and the field-induced ferromagnetic state. The phase boundaries also have an analogous shape. The determined phase diagrams are very similar to those of $R\mathrm{RhIn}_5$ compounds [77, 94] which signifies similar magnetic properties. The phase diagram of Nd_2RhIn_8 presented in [77] was rather uncompleted, but latest results on our piece of single crystal [99] shows the same shape of the phase diagram as in the other compounds. The magnetic phase diagrams of $R_2\mathrm{CoGa}_8$ compounds show also two magnetic phases and somewhat different shape of the phase boundaries [92]. The magnetic structure of the field-induced phase in the $R_2\mathrm{CoGa}_8$ system is unknown neither.

The magnetic moments in Er_2RhIn_8 and Tm_2RhIn_8 lie within the *ab*-plane as demonstrated on Figure 17. This is again in analogy to the $R\mathrm{RhIn}_5$ or $R_2\mathrm{CoGa}_8$ series [93, 92]. The [100] easy magnetization direction is reported in these two series, whereas our magnetization data reveal clearly the [110] direction as the easy magnetization in Er_2RhIn_8 and Tm_2RhIn_8. It is not clear, whether the measurement along this direction was performed for the two other series mentioned above.

We want to point out tetragonal system "122" with $ThCr_2Si_2$-structure type, where the compounds $TbCo_2Si_2$, $DyCo_2Si_2$, $TbCo_2Ge_2$ and $DyCo_2Ge_2$ exhibit the similar behaviour [100, 101]. It is important to note, that first heavy fermion superconductor $CeCu_2Si_2$ [10] grows with the same structure type.

4.4. Magnetic structures

In order to determine microscopic details of the magnetically ordered phase in studied compounds, a series of neutron diffraction experiments were performed. Generally, a Laue experiment was first performed to determine the propagation vector and then we continued on single crystal diffractometer. All experiments were taken on the same samples as bulk measurements, see Table 5.

4.4.1. Determination of the propagation vectors

Together six experiments on six compounds from the series were done on two Laue diffractometers CYCLOPS and VIVALDI at ILL. The Laue patterns for each compound were always recorded in the paramagnetic and ordered regions to allow magnetic satellites to be easily distinguished. For each sample the crystal was mounted with the obvious symmetry axes well away from the vertical axis. This orientation allows us to eliminate presence of the reflections only on the detector

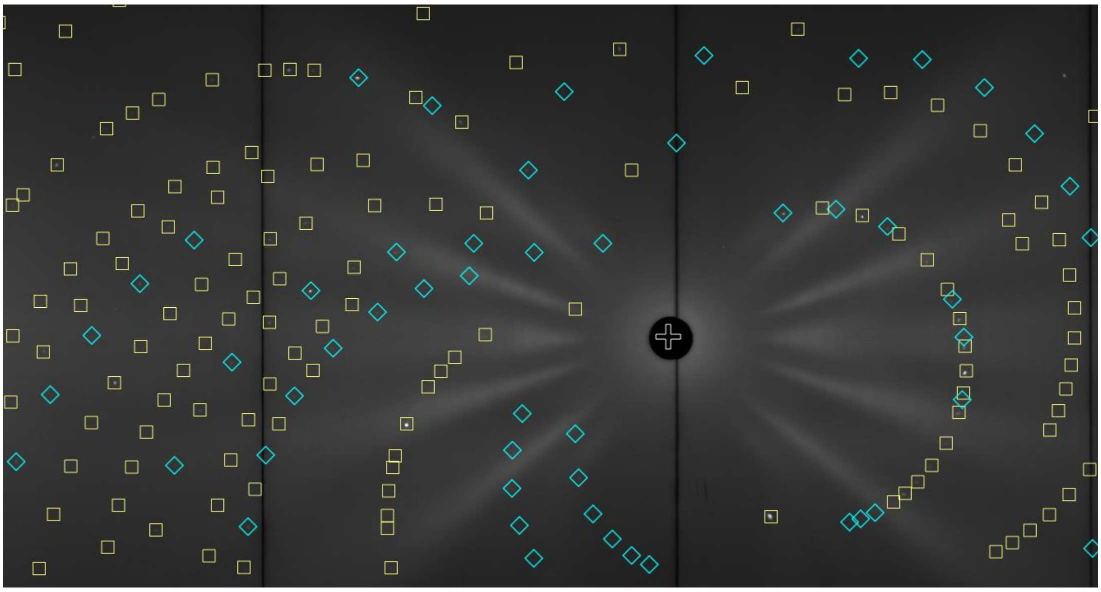

Figure 20 - Laue pattern of Nd_2RhIn_8 taken at 2 K. Yellow squares denote nuclear reflections and blue diamonds denote magnetic satellites.

boundary and also discover any possible purely magnetic signal. Laue patterns were than taken at several ω angles. The count of patterns as well as used temperatures for each compound is summarized in the Table 9.

Table 9 - Measured Laue patterns

Sample	Instr.	Paramagnetic state				Ordered state				Fig.
		T [K]	#	t [min]	$\Delta\omega$ [°]	T [K]	#	t [min]	$\Delta\omega$ [°]	
Nd_2RhIn_8	VIVALDI	30	9	115	10	2	9	115	10	20
Tb_2RhIn_8	VIVALDI	60	9	55	10	10	9	55	10	21
Dy_2RhIn_8	VIVALDI	40	9	55	10	2	9	55	10	21
Ho_2RhIn_8	CYCLOPS	14	2	180	30	1.5	26	15	5	22
Er_2RhIn_8	CYCLOPS	8	26	15	5	1.5	26	15	5	22
Tm_2RhIn_8	CYCLOPS	6	5	35	30	1.5	5	35	30	27

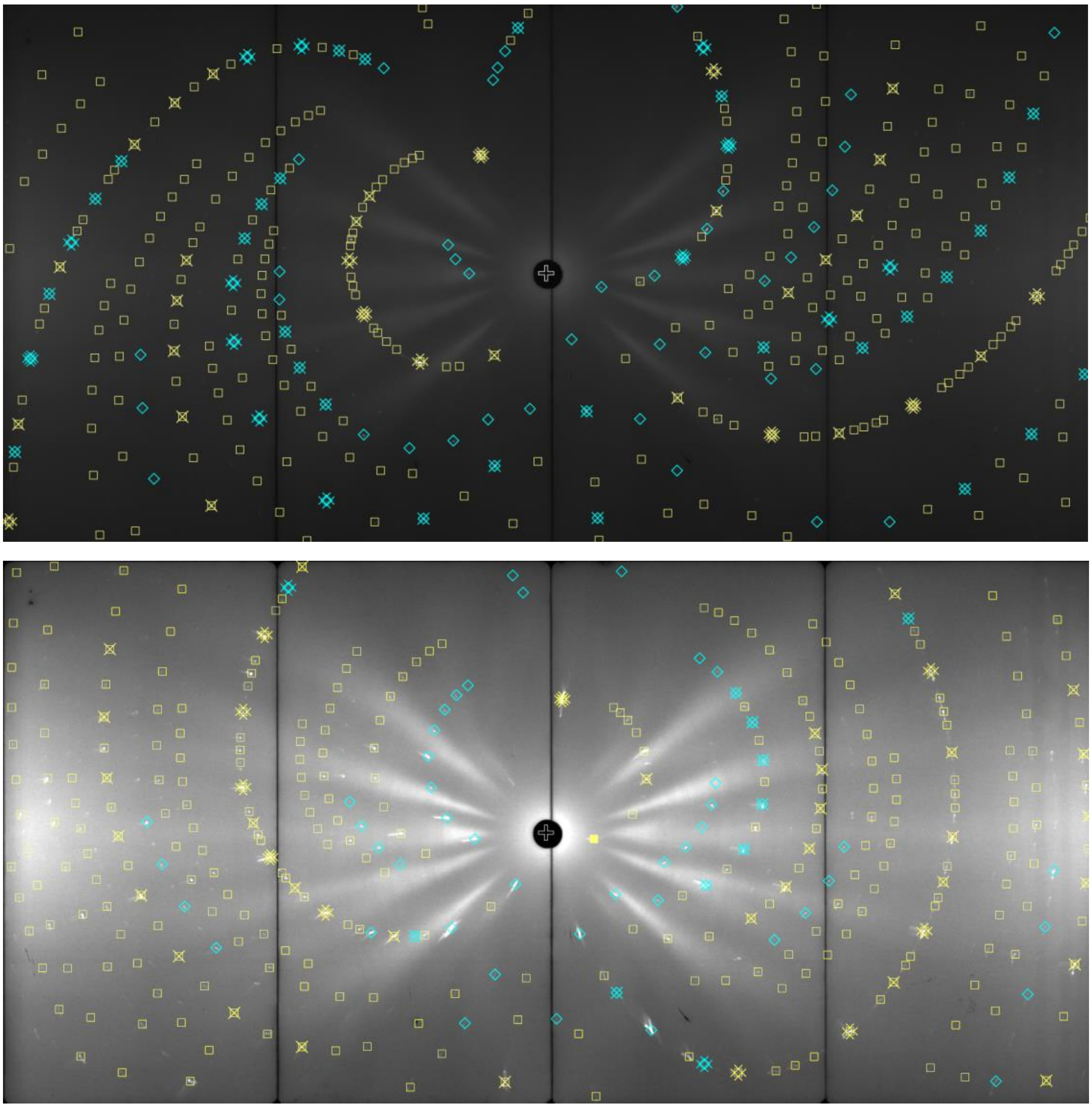

Figure 21 - Laute pattern of Tb_2RhIn_8 (top) and Dy_2RhIn_8 (bottom) taken at 10 and 2 K, respectively. Yellow squares denote nuclear reflections while blue diamonds denote magnetic ones.

In addition for Ho_2RhIn_8, series of 50 patterns was taken in the slow temperature sweep mode (0.1 K/min) in order to determine temperature dependence of the magnetic Bragg peaks and the nature of AF3 phase mention in the Chapter 4.3.4. Each of these patterns was recorder only for 2 minutes, but with higher gain of the cameras. Such a high gain is not ideal for further quantitative refinement of the pattern, because of a big increase of the electronic noise. However it is possible to use it during temperature sweep, if we just want to follow intensity of selected peaks and look for the creation of the new ones. Results of these measurements are described in chapter 4.4.4.

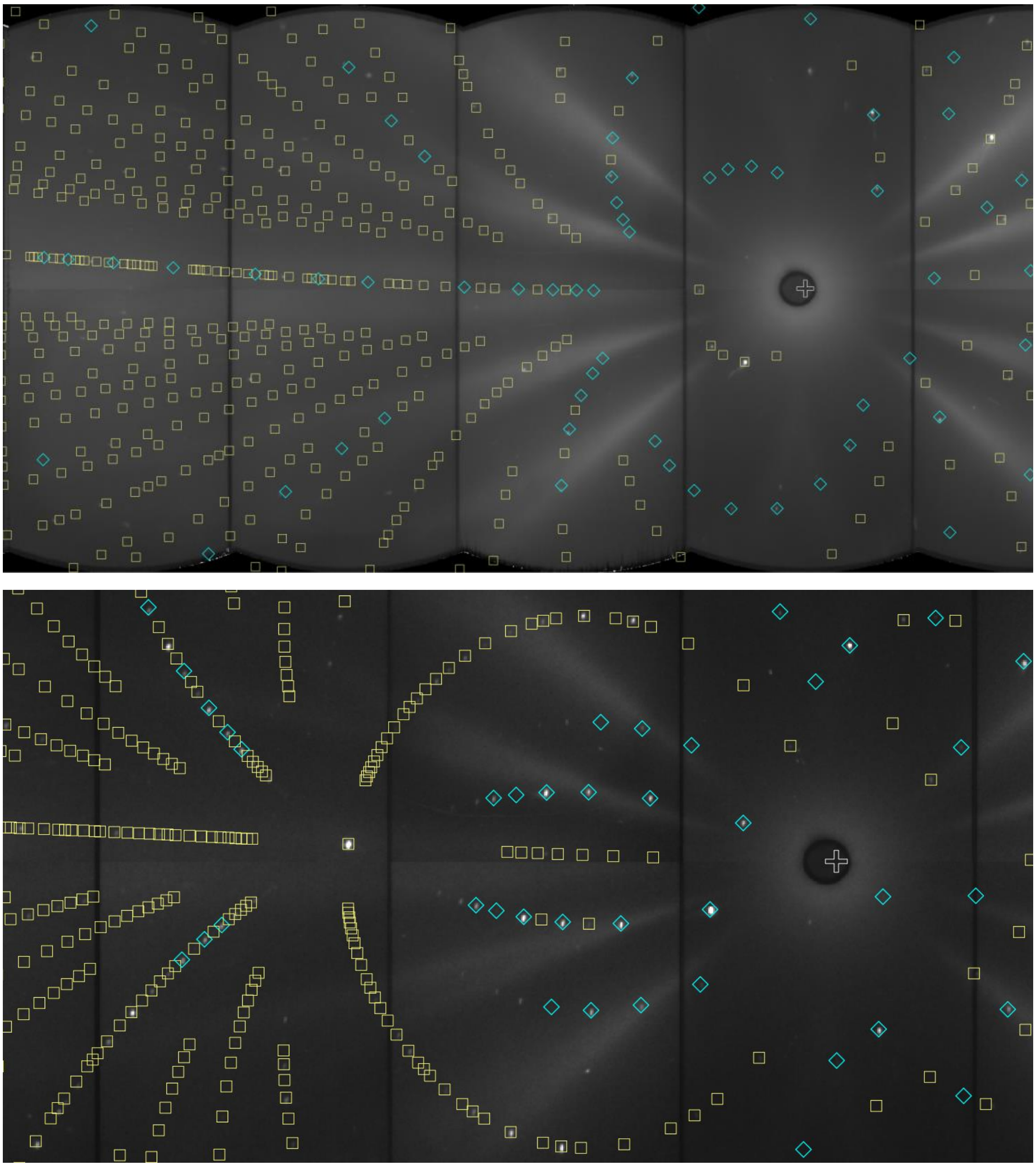

Figure 22 - Laute pattern of Ho_2RhIn_8 (top) and Er_2RhIn_8 (bottom) taken at 1.5 K. Yellow squares denote nuclear reflections and blue diamonds denote magnetic ones.

The CYCLOPS patterns were first transformed from octagonal to cylindrical geometry, and also a mathematical filter for decreasing noise was applied. For the measurement of Er_2RhIn_8, an alpha correction for the different sensitivity of different cameras can also be applied. But since this kind of treatment of the CYCLOPS data is still in commissioning phase, this correction was finally not used. The patterns from VIVALDI were used without further changes. All Laue patterns, both from the VIVALDI and the CYCLOPS instruments, were indexed and integrated using the Esmeralda Laue Suite software [39]. This software was also used for finding propagation vectors.

The overall Laue pattern for Nd_2RhIn_8 is represented in Figure 20, for Tb_2RhIn_8 and Dy_2RhIn_8 is in Figure 21 and for Ho_2RhIn_8 and Er_2RhIn_8 in Figure 22. The diffuse streaks on all patterns correspond to the textured powder pattern due to aluminium in the cryostat. All the observed diffraction spots at paramagnetic temperature can be indexed assuming the tetragonal structure with the space group P4/mmm. At the cryostat base temperature, a large number of new, purely magnetic reflections appear. All magnetic reflections in the compounds with *R* = Nd, Tb, Dy

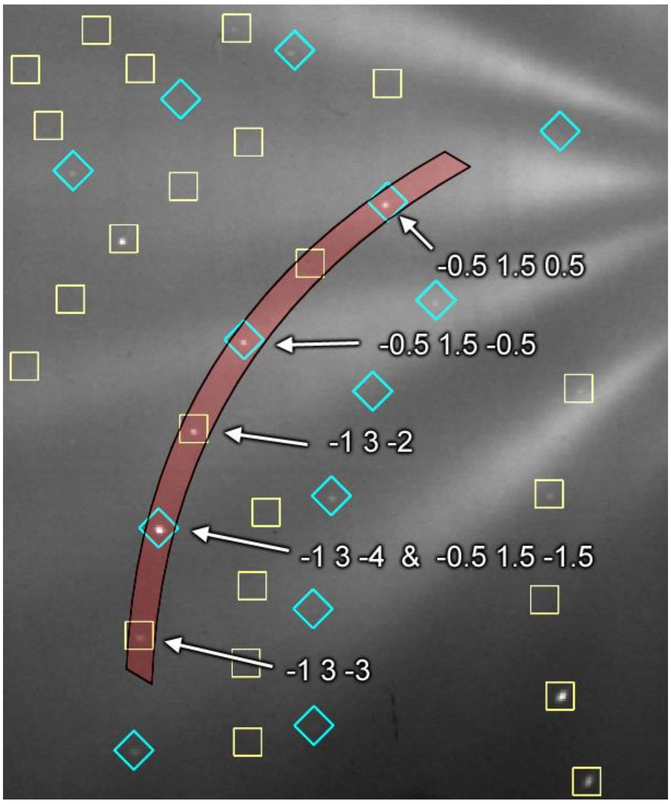

Figure 23 - Part of the Laue picture of Nd2RhIn8 with diffraction spots marked as in Figure 20. Red color denotes area of integration along the reciprocal [hkl]* (with h = −1, k = 3, and l = n) direction which corresponds to the intensities shown in Figure 24.

and Er can be described by a single propagation vector $\boldsymbol{k} = \left(\frac{1}{2},\frac{1}{2},\frac{1}{2}\right)$. The propagation vector of Ho_2RhIn_8 is different; there we observed reflections, which can be described by propagation vector $\boldsymbol{k} = \left(\frac{1}{2},0,0\right)$ and equivalent $\boldsymbol{k} = \left(0,\frac{1}{2},0\right)$. This implies existence of the multi-k structure or magnetic domains in the sample.

To illustrate indexation of the spots belonging to determined propagation vectors, we show a smaller cut of the Laue picture of Nd_2RhIn_8 in Figure 23. The intensities along the [001] crystallographic direction, indicated in that picture, are then shown in Figure 24. Note that individual positions could correspond simultaneously to several reflections that are overlapped with different wavelengths. Therefore more than one reflection can contribute to one spot.

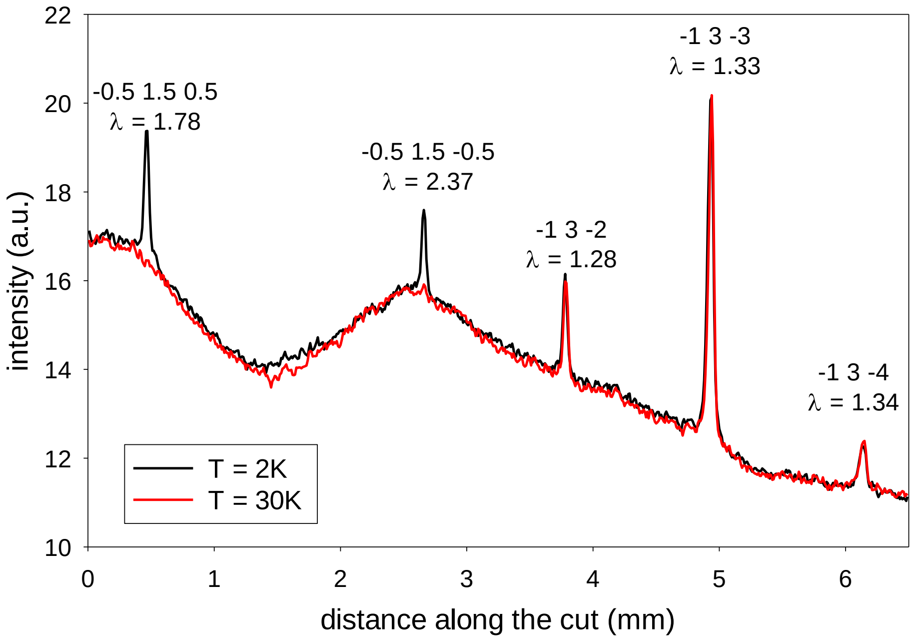

Figure 24 - Diffraction intensities taken from a cut through a Laue picture of Nd_2RhIn_8 as indicated in Figure 23.

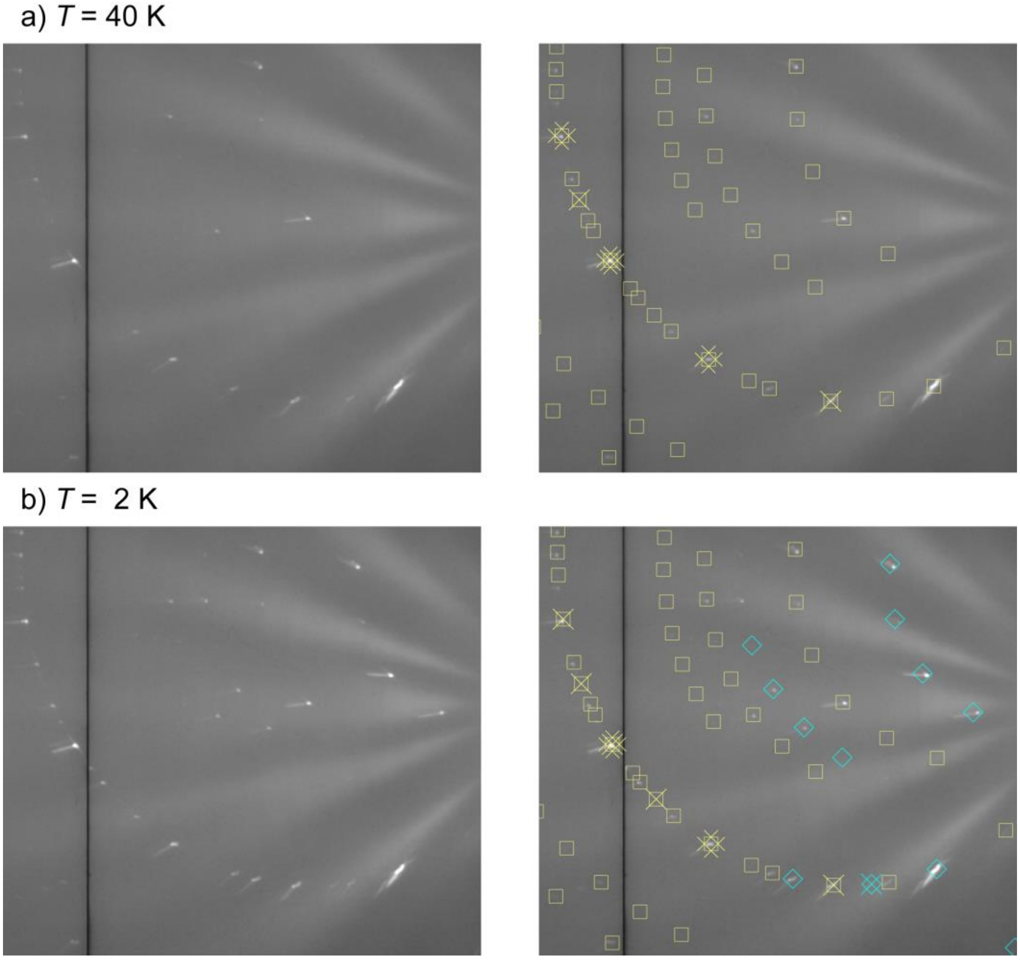

Figure 25 – Comparison of the selected part of the Laue pattern of Dy_2RhIn_8 at paramagnetic (a) and ordered (b) region. Left part of each picture is raw data, right is overlaid with indexed peak positions.

Another illustration is done in Figure 25 for Dy_2RhIn_8. You can see number of new spots, which appeared when entering magnetically ordered region in the T = 2 K. All newly appeared peaks are indexed with commensurate propagation vector $\boldsymbol{k} = \left(\frac{1}{2}, \frac{1}{2}, \frac{1}{2}\right)$. Blurred peaks are denoted to be effect of big crystal mosaicity. This effect does not influence the determination of the commensurate propagation vector.

The final compound studied by Laue diffraction is Tm_2RhIn_8. From its Laue patterns it is clear that it orders incommensurately, see Figure 27 for full indexed pattern from CYCLOPS instrument. Indexing all the peaks is not very straightforward. A large number of reflections can be ascribed to propagation vector $\boldsymbol{k_1} = \left(\frac{1}{2}, 0, 0.42\right)$, however a few clear magnetic peaks were not indexed. The first possible solution is to allow existence of higher harmonics and therefore probably some square modulated structure along c-axis. Another solution is to use a second propagation vector $\boldsymbol{k_1} = (0,0,0.16)$. The possible indexation of selected cut through the Laue pattern regarding two propagation vectors is depicted on Figure 26.

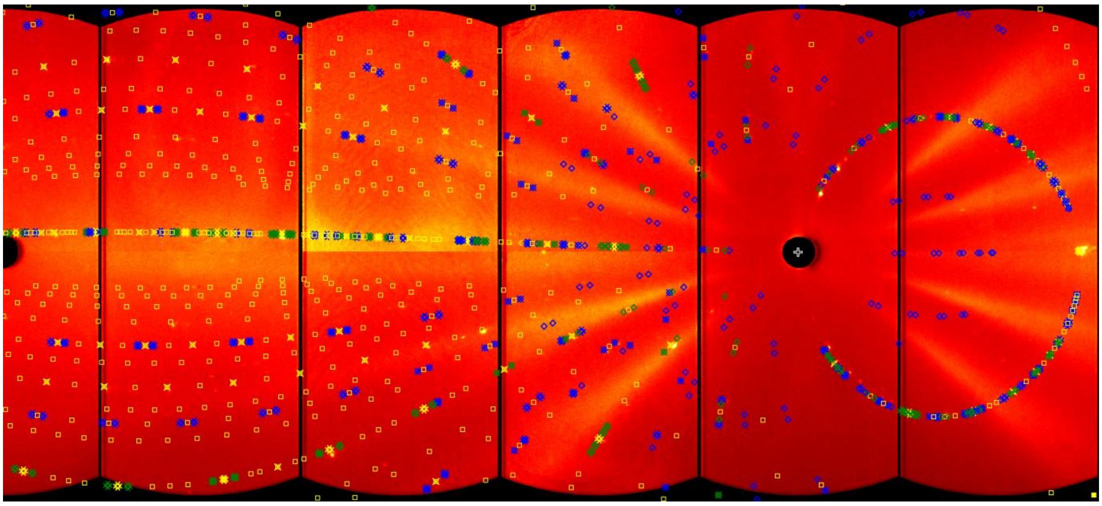

Figure 27 - Laute pattern of Tm_2RhIn_8 taken at 2 K. Yellow squares denote nuclear reflections while the blue and the green diamonds denote magnetic ones.

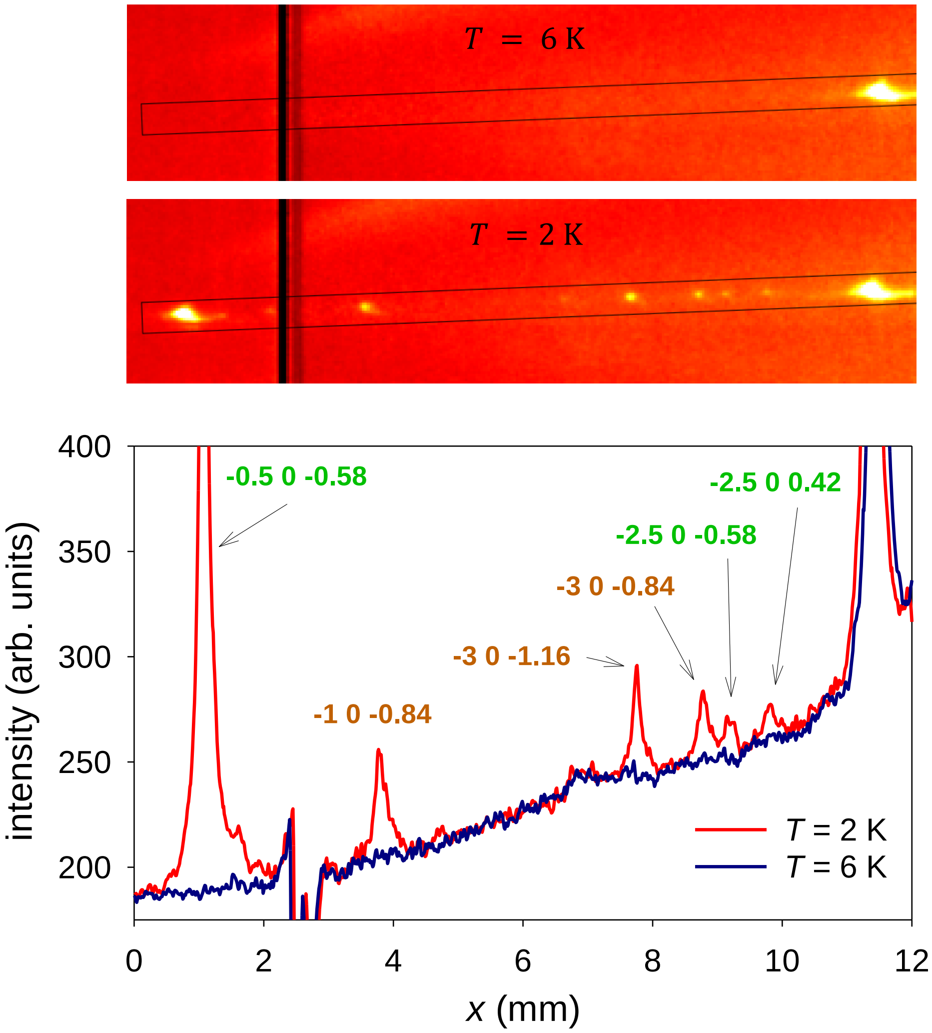

Figure 26 – Diffracted intensities along the cut from the Laue pattern of Tm_2RhIn_8. Cuts from the pattern are depicted above the intensity chart.

We can summarize the results from Laue diffraction measurement as follows: only the Tm_2RhIn_8 compound has an incommensurate magnetic structure, deviating from the studied series and also related “218” and “115” compounds. All other compounds orders with commensurate antiferromagnetic structures. Determined propagation vectors are summarized in Table 10. The knowledge of the propagation vector was subsequently used during the further single crystal diffraction experiments in the next chapters.

Table 10 - Determined propagation vectors

Compound	Propagation vector $\boldsymbol{k}$
Nd_2RhIn_8	$\left(\frac{1}{2},\frac{1}{2},\frac{1}{2}\right)$
Tb_2RhIn_8	$\left(\frac{1}{2},\frac{1}{2},\frac{1}{2}\right)$
Dy_2RhIn_8	$\left(\frac{1}{2},\frac{1}{2},\frac{1}{2}\right)$
Ho_2RhIn_8	$\left(\frac{1}{2},0,0\right)$
Er_2RhIn_8	$\left(\frac{1}{2},\frac{1}{2},\frac{1}{2}\right)$
Tm_2RhIn_8	$\left(\frac{1}{2},0,0.42\right)$ + higher harmonics or $\left(\frac{1}{2},0,0.42\right)+(0,0,0.16)$

4.4.2. Representation analysis

In order to restrict the number of possible magnetic structures, we applied symmetry arguments as developed in the representation analysis [102]. The different irreducible representations with their associated basis vectors have been calculated with the help of the BasIreps program [29] using the previously determined propagation vectors. Let us now in details describe the situation in the case of the most common propagation vector $\boldsymbol{k}=\left(\frac{1}{2},\frac{1}{2},\frac{1}{2}\right)$.

The little group (or group of the propagation vector) coincides with the space group $G_{\boldsymbol{k}}=P4/mmm$ (all rotational symmetry operators of P4/mmm leave invariant the propagation vector), so the small representations coincides with the full irreducible representations of the space group. There are together 10 irreducible representations ($irreps$) associated with the $\boldsymbol{k}=\left(\frac{1}{2},\frac{1}{2},\frac{1}{2}\right)$ propagation vector. Two of them, Γ_9 and Γ_{10}, are two-dimensional and remaining 8 are one-dimensional. However, the global reducible magnetic representation of the R $2g$ Wyckoff site can be decomposed in $irreps$ as $\Gamma_{2g} = \Gamma_2 + \Gamma_7 + \Gamma_9 + \Gamma_{10}$. Because there are always two magnetic sublattices corresponding to the 2g Wyckoff site within the unit cell, the basis vectors have six components each. The first three correspond to the magnetic moment components of the R atom at the position with x, y, z site symmetry (R1) and the other three to those of the atom at the $-x, y, -z + 1$ site (R2). By making linear combinations of the basis vectors within the same irreducible representation we obtain the vectors representing the components of the magnetic moments of both atoms. These combinations are summarized in Table 11. One can see, that in the case of the one-dimensional representations Γ_2 and Γ_7 there is only a single free parameter u describing the magnetic structure. For the two-dimensional representations Γ_9 and Γ_{10}, there are, in general, two parameters u and v. In both cases the difference between Γ_2 and Γ_7, or Γ_9 and Γ_{10}, respectively, resides in the either parallel, or antiparallel coupling between the two rare-earth sublattices. As the propagation vector is $\boldsymbol{k} = \left(\frac{1}{2}, \frac{1}{2}, \frac{1}{2}\right)$, the magnetic unit cell is doubled in x, y, z direction and the direction of the moments in the neighboring (chemical) unit cells have to be opposite.

Table 11 - Direction of magnetic moments for all possible irreducible representations corresponding to the propagation wave vector $\boldsymbol{k} = \left(\frac{1}{2}, \frac{1}{2}, \frac{1}{2}\right)$ and the magnetic $2g$ site in the P4/mmm space group.

site	Γ_2	Γ_7	Γ_9	Γ_{10}
R1	$0\ 0\ u$	$0\ 0\ u$	$u\ -v\ 0$	$u\ v\ 0$
R2	$0\ 0 - u$	$0\ 0\ u$	$-u\ v\ 0$	$u\ v\ 0$

The similar analysis has been done also for other possible propagation vectors, $\boldsymbol{k} = \left(\frac{1}{2}, 0{,}0\right)$ found in Ho_2RhIn_8 and Er_2CoGa_8 and $\boldsymbol{k} = \left(\frac{1}{2}, 0, \frac{1}{2}\right)$ found in Tm_2CoGa_8. For a detailed analysis of these cases see work of Johnson et al. [61]. Summary of all possible magnetic structures regarding theory of representations is in Table 12. Note that within one unit cell are two positions of R atom, which means that for example stacking $+ - - +$ along c-axis is stacking over two unit cells.

Table 12 - Possible magnetic structures regarding theory of representations.

	moment direction	c-axis stacking
$\boldsymbol{k} = \left(\frac{1}{2}, 0, 0\right)$	a	$++++$
	a	$+-+-$
	b	$++++$
	b	$+-+-$
	c	$++++$
	c	$+-+-$
$\boldsymbol{k} = \left(\frac{1}{2}, 0, \frac{1}{2}\right)$	a	$+--+$
	a	$++--$
	b	$+--+$
	b	$++--$
	c	$+--+$
	c	$++--$
$\boldsymbol{k} = \left(\frac{1}{2}, \frac{1}{2}, \frac{1}{2}\right)$	c	$+--+$
	c	$++--$
	in ab-plane	$+--+$
	in ab-plane	$++--$

4.4.3. Single crystal diffraction experiments in zero-field

The four-circle neutron diffraction experiments were performed for the Nd_2RhIn_8, Dy_2RhIn_8 and Ho_2RhIn_8 samples on the D10 diffractometer at ILL, with a wavelength $\lambda = 2.36$ Å using pyrolytic graphite monochromator and filter before the sample. The sample was installed into a C-shaped Eulerian cradle equipped with a special helium-flow cryostat allowing cooling up to 1.5 K. After cooling the samples to 2 K, cell parameters and orientation were refined on the basis of several strong nuclear reflections using the program RAFD9 [21]. The number of reflections used for initial refinement is written in Table 13. Then a set of reflections at 2 K and temperature dependencies of selected magnetic and nuclear reflections were taken for Nd_2RhIn_8 and Dy_2RhIn_8. For Ho_2RhIn_8 only nuclear reflections were measured, in order to refine extinction parameters and use them in the refinement of further field experiment on E4. Refer next chapter 4.4.4 for details. All reflections were measured as ω-scans. They were integrated and corrected for Lorentz factor using the program RACER [20].

In the case of Er_2RhIn_8, we have used the triple axis spectrometer IN3 at ILL. The sample was mounted with the [110] and the [001] lattice vectors in the scattering plane into the standard ILL helium-flow "orange" cryostat. After cooling to 1.5 K, the tilt of the sample was adjusted by a goniometer and the lattice parameters were refined. Contrary to D10, IN3 has only ^{3}He detector tube, so measured data are only 1D scans. We measured the reflections in the elastic condition at $\lambda = 2.36$ Å using ω-scans as well. All measured datasets from IN3 were fitted with Gaussian profiles using Python script and the integrated intensities were corrected for the Lorentz factor (see Appendix 1. for the used script).

Table 13 - Summary of performed single crystal diffraction experiments in zero-field

	Nd_2RhIn_8	Dy_2RhIn_8	Ho_2RhIn_8	Er_2RhIn_8
Instrument	D10	D10	D10	IN3
absorption coefficient (cm−1)	9.018	19.134	9.738	10.707
number of measured reflections (nonequivalent)				
for orienting	41	20	19	-
nuclear	364 (70)	350 (68)	345 (68)	60 (21)
magnetic	461 (50)	383 (38)	-	57 (15)

All measured compounds contain large amounts of indium, which is medium absorbing material for neutrons and moreover dysprosium is very absorbing element. Therefore all integrated intensities were corrected for absorption correction. Their absorption coefficients were calculated based on equation (23) and are tabulated in Table 13. The program DATAP [27] was used for the correction of the integrated intensities. As an input for the routine, we used sample sizes from Table 5 and calculated absorption coefficients.

The obtained set of data contained many equivalent reflections. All these were reduced together using the program DataRed [29]. Obtained number of measured equivalent and non-equivalent reflections is listed in Table 13. The program FullProf [29] was used for the refinement of the nuclear and magnetic structures. The extinction correction for Nd_2RhIn_8, Dy_2RhIn_8 and Er_2RhIn_8 was refined using the Zachariasen formula with anisotropic correction (`Ext-Model=4` in FullProf). The isotropic variant of this correction (`Ext-Model=1`) was used for Ho_2RhIn_8. The reason for this was an idea of using refined extinction parameter from D10 as fixed input for the measurement on the E4 diffractometer in field. This is possible to do because both instruments use the similar wavelength and both measurements were performed on the same single crystal. See next chapter 4.4.4 for E4 experiment.

We have tried to use also Becker Coppens algorithm for extinction refinement in order to obtain domain radius and mosaic spread in these compounds. Application of such correction should be possible, since program DATAP calculated absorption weighted path of the incident and diffracted beam within the crystal for each measured reflection. However application of such model did not lead to stable least-square fit. After the discussion with the author of FullProf, Juan Rodriguez-Carvajal, it was concluded, that this fitting model is in FullProf not yet fully working.

The determined structural parameters at the lowest temperature are summarized in Table 14. To illustrate the quality of the fit, the observed vs. calculated integrated nuclear intensities are depicted in Figure 28 and the reliability factors from the FullProf refinement are in listed in Table 13. The worse fit for the Ho_2RhIn_8 is caused by the fact, that we used an isotropic fit for the extinction. Fitting with anisotropic parameters causes big improvements for the fit, especially for the

Table 14 - Structural parameters of R_2RhIn_8 at $T = 1.6$ K determined from neutron diffraction.

R	Nd	Dy	Ho	Er
		lattice parameters		
a (Å)	4.6213(9)	4.572(2)	4.5648(16)	4.552(2)
c (Å)	12.113(3)	11.96(1)	11.953(12)	11.980(2)
		atomic positions along the c-axis		
R	0.3083(3)	0.3095(2)	0.3098(3)	0.311(1)
In(2)	0.3059(6)	0.3078(7)	0.3086(6)	0.311(1)
In(3)	0.1212(4)	0.1226(5)	0.1245(4)	0.125(2)
		reliability factors		
RF^2	6.70	5.58	11.5	11.80
RF	5.34	4.40	10.1	9.94
χ^2	3.14	2.58	5.67	3.57

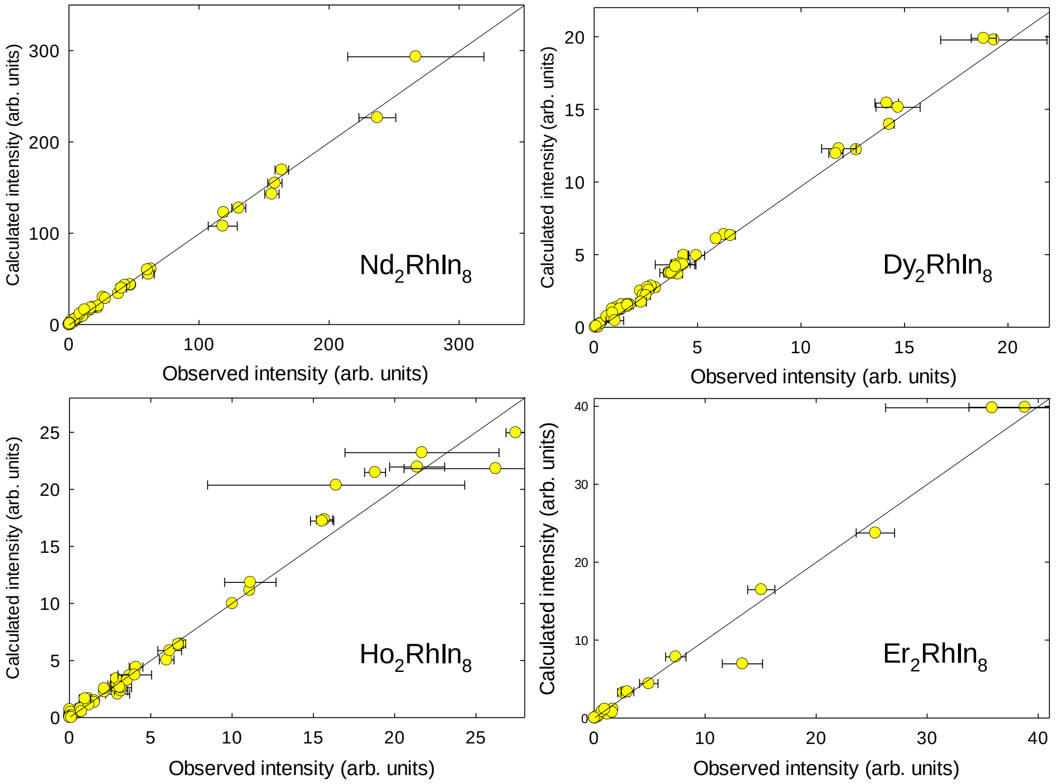

Figure 28 – Observed and calculated integrated nuclear intensities. The calculated intensities correspond to the parameters given in Table 14.

strong reflections where the extinction is important. The worse fit for the Er_2RhIn_8 is caused by using only 2-circle geometry. A consequence of this is a smaller amount of the reachable reflections and also additional error cause by misalignment of the scattering plane. In total all nuclear structure measurements are in agreement with expected space group P4/mmm and Ho_2CoGa_8 structure type.

The temperature dependence of the selected nuclear intensities of Nd_2RhIn_8 and Dy_2RhIn_8 is shown in Figure 29. We observed no change in intensity above and below the transition temperature, indicating that there is no contribution with $\boldsymbol{k} = (0, 0, 0)$ propagation vector. Similar conclusion can be deduced from the temperature dependence of Laue patterns from CYCLOPS for Er_2RhIn_8 and Ho_2RhIn_8, where no change in nuclear intensities is observed as well.

As the whole next chapter is devoted to magnetic structure of Ho_2RhIn_8, we will skip it for now and we will focus on compounds with Nd, Dy and Er on the position of rare earth element. All have same commensurate propagation vector $\boldsymbol{k} = \left(\frac{1}{2}, \frac{1}{2}, \frac{1}{2}\right)$ and thus the results from the previous chapter give us only several possibilities of magnetic moment arrangements. All four possible magnetic structures (listed in Table 12) were refined in FullProf software. The best agreement between observed and calculated intensities of Nd_2RhIn_8 and Dy_2RhIn_8 is obtained for magnetic moments pointing along the *c*-axis with their parallel alignment within one unit cell and corresponding to Γ_2.

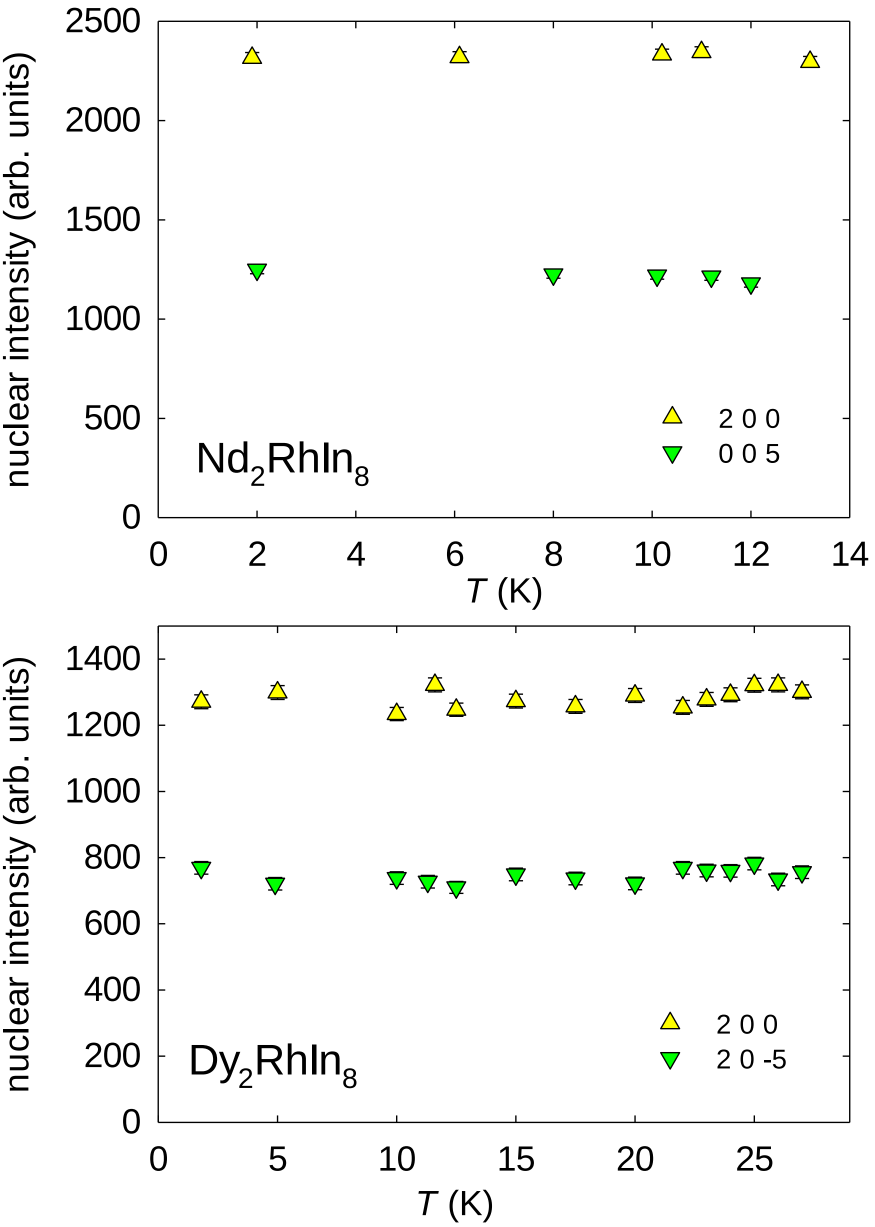

Figure 29 – Temperature dependence of intensities of selected reflections.

For Er_2RhIn_8 the fitting procedure showed that the best agreement is obtained with the model Γ_{10} where the magnetic moments in the unit cell lie in the *ab*-plane pointing the same direction ($+ + - -$ stacking along the *c*-axis). As Er_2RhIn_8 was measured in IN3, only reflections within the (-110) scattering plane could be measured. Taken set of reflection is then not sufficient to determine the exact direction of the moments within the *ab*-plane.

The refined amplitudes of the magnetic moments are summarized in Table 15 and the obtained magnetic structures are depicted in Figure 30. The comparison of observed and calculated intensities for all compounds is shown in Figure 31.

Table 15 - Magnetic structure parameters of Nd_2RhIn_8, Dy_2RhIn_8 and Er_2RhIn_8.

R	Nd	Dy	Er
magnetic structure			
$\boldsymbol{k}$		$\left(\frac{1}{2},\frac{1}{2},\frac{1}{2}\right)$	
μ (μ_B)	2.53(9)	6.9(3)	6.4(1.4)
direction of the moment	c-axis	c-axis	ab-plane
c-stacking	$++--$	$++--$	$++--$
T_N (K)	10.63(4)	24.24(8)	3.70(6)
β	0.22(3)	0.20(1)	0.16(2)
reliability factors			
magnetic RF^2	15.5	9.46	20.2
magnetic RF	9.83	6.95	13.2
magnetic χ^2	6.01	2.65	8.29

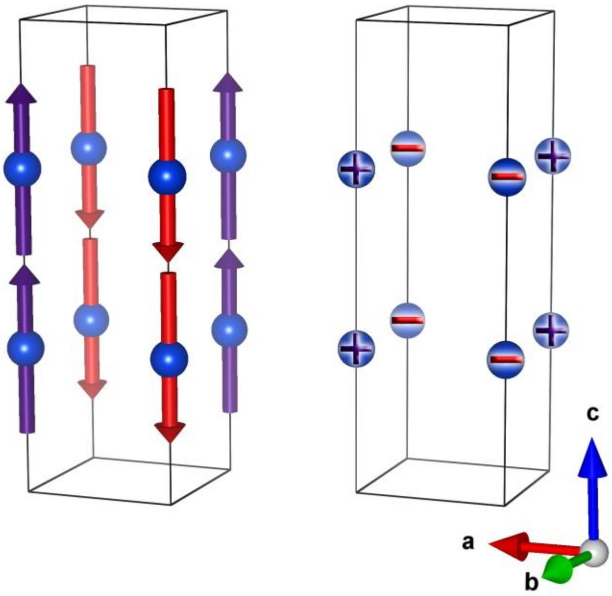

Figure 30 – Magnetic structure of Nd_2RhIn_8, Dy_2RhIn_8 (left) and Er_2RhIn_8 (right) compounds. Note that magnetic moments of Er_2RhIn_8 can point anywhere within the *ab*-plane, but are all parallel to each other.

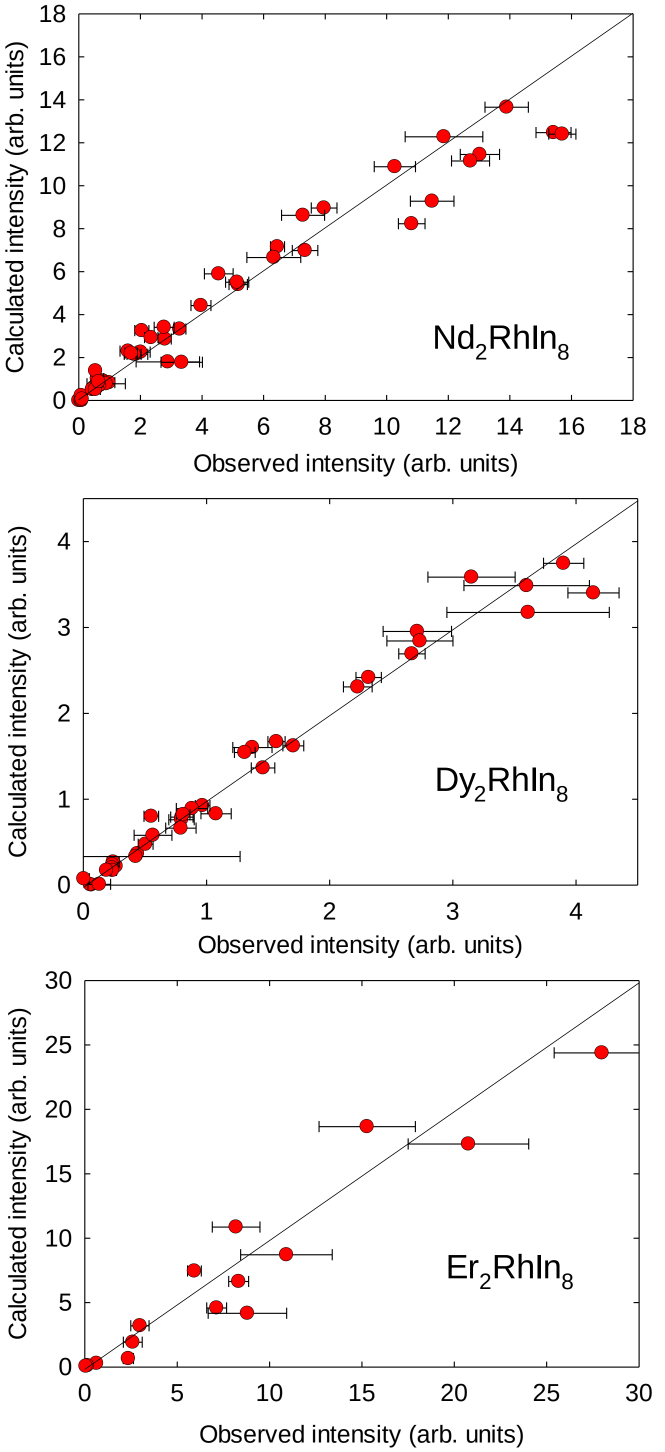

Figure 31 – Observed and calculated integrated magnetic intensities. The calculated intensities correspond to the parameters given in Table 15.

For completion of the magnetic refinement, the rare-earth moments were allowed to lie in a general direction by combining two representations in order to check a lowering of symmetry. We did not observe any noticeable improvement of the fits and the local minima were always found within 1 - 2 degrees out of the previously determined direction using a single representation. We can therefore conclude that the magnetic moments of Nd_2RhIn_8 and Dy_2RhIn_8 lie along the tetragonal c-axis, while they lie within the ab-plane in the case of Er_2RhIn_8, lowering the symmetry at least to orthorhombic (remember that for experimental limitations we could not determine the directions of the moment within the ab-plane).

4.4.4. Magnetic structures of Ho_2RhIn_8 in its rich phase diagram

In chapter 4.3.2 was revealed, that Ho_2RhIn_8 is special among the other studied compound, because it has most complex phase diagram (Figure 19). In addition to zero-field phase AF1 and field induced phase AF2, which exists also in other compounds with easy magnetization axis along c-axis, there exists another small zero-field region near transition temperature. It was speculated, that reason for this is either impurities, or existence of an incommensurate phase AF3. Because of this exceptional character, Ho_2RhIn_8 was chosen for most detailed study.

Magnetic phase AF1 as well as the behaviour in applied magnetic field was measured using the two-axis neutron diffractometer E4 at Helmholtz-Zentrum Berlin, Germany. Focusing monochromator with vertically bent PG crystals was used to select the wavelength $\lambda = 2.432$ Å. Scattered intensities were observed using a 200x200 mm two-dimensional position-sensitive detector (PSD) in distance $l_{s-d} = 748$ mm from the sample. The experiment was performed using a He flow cryostat at the temperature range 1.6 - 15 K. First the sample was loaded into a horizontal-field magnet HM-2 and aligned with its reciprocal (h, 0, l) plane in the horizontal scattering plane of the instrument. Magnetic field was then applied along easy c-axis. In order to extend number of observable reflections, sample was realigned and mounted to the vertical-field magnet VM-2 to have (h, k, 0) plane aligned with scattering plane of the instrument. 10° opening angle of the magnet allows us to reach reflections with index (h, k, 0.5) on the PSD detector.

In addition we have used the triple axis spectrometer IN3 at ILL to measure few missing information, as zero-field temperature dependence of magnetic Bragg reflections. See chapter 4.4.3 for instrument setup.

Treatment of the E4 data is little bit more complicated than treatment of data from D10, because there is no software for automatic integration of 2D detector data (as RACER in ILL). The whole integration process was therefore done by Python script (see appendix 2. for details). At first, background detector data were cut out to the rectangular shape around observed reflection. Then fitting of the Gaussian profile function along the ω-scan. This technique allows us to reduce the background and also to distinguish out-of-plane and in-plane reflections.

We will illustrate process of the data treatment on the reflection 0.5 0.5 0.5 which was measured in the vertical magnet. As the sample was oriented with (h, k, 0) scattering plane, this reflection appeared out of the plane. It appeared at $2\theta = 21.71°$, $T = 1.60\,\mathrm{K}$ and in applied field $B = 3\,\mathrm{T}$. See raw measured data visualized on Figure 32. We have measured simultaneously reflection 0.5 0.5 0.5 and a part of equivalent reflection 0.5 0.5 -0.5. Since bottom reflection did not appeared fully, we have treated only the top reflection.

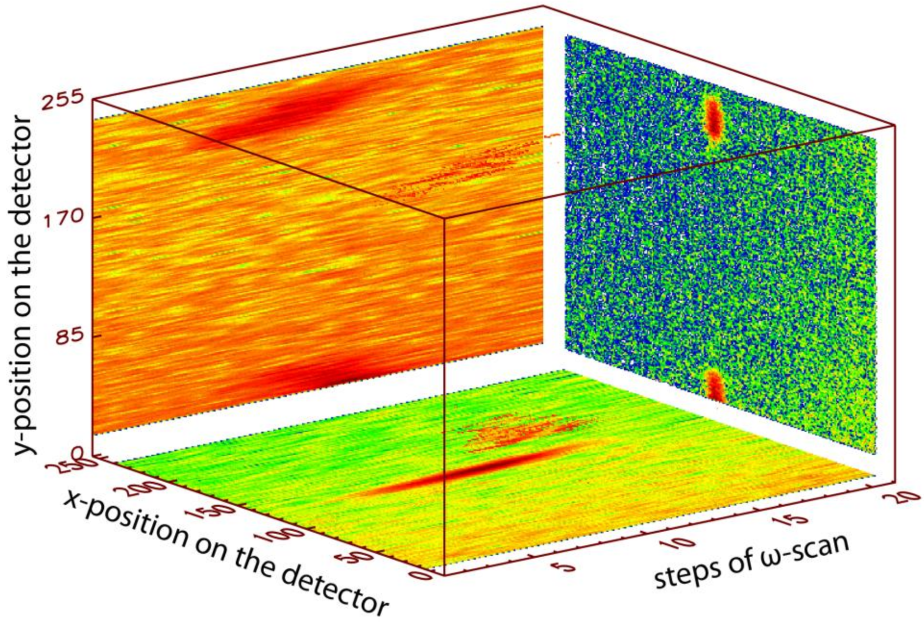

Figure 32 – measured reflection 0.5 0.5 0.5 in vertical magnetic field 3T.

Let us clarify, that measured spot really belongs to 0.5 0.5 0.5 reflection. Considering that lattice constant c is much bigger than a and measured reflection is close to the scattering plane, it is possible to derive following relation from Bragg law and simple geometrical constrains:

$$L = \frac{y_{spot}}{l_{s-d}} \frac{c}{\lambda}, \qquad (25)$$

where L is reciprocal coordinate of measured spot, y_{spot} is vertical distance of the measured spot from the middle of the detector and l_{s-d} is distance between sample and detector. As $y_{spot} = 78\,\mathrm{mm}$, resulting L =0.51, which confirms that observed peak is the 0.5 0.5 0.5 reflection.

The next step in treatment of the peak is its trimming, which leads to area shown in Figure 33. These data were summed along x and y direction of the detector producing intensity vs. ω dependence, which was fitted with background + Gaussian profile. Resulting integrated intensity was corrected for Lorentz factor, equation (18). All measured peaks on E4 were treated in this way.

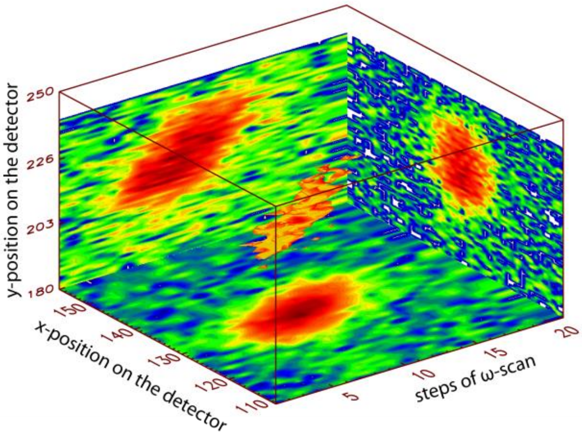

Figure 33 – Trimmed raw intensity data of the reflection 0.5 0.5 0.5

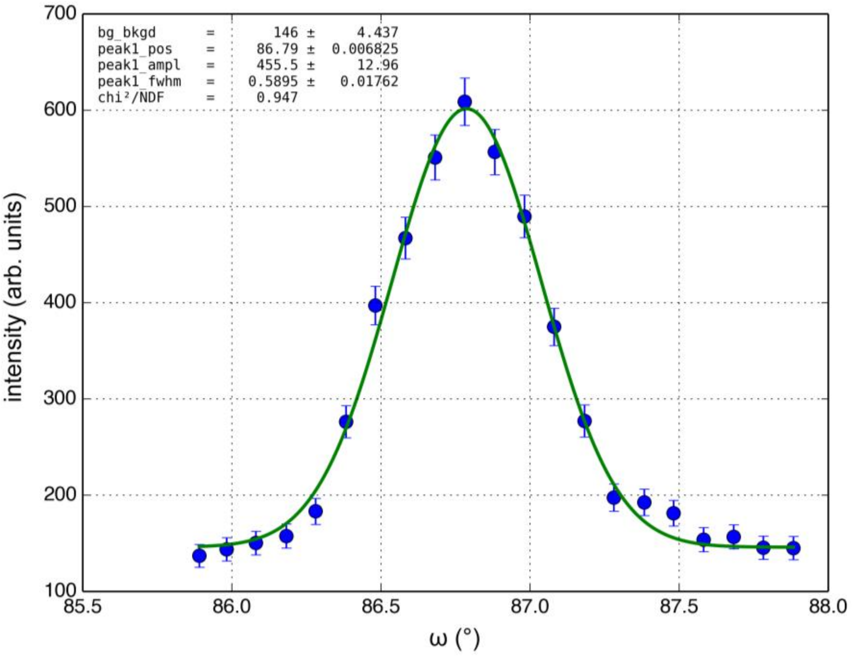
```
bg_bkgd      =      146 ±     4.437
peak1_pos    =    86.79 ±  0.006825
peak1_ampl   =    455.5 ±     12.96
peak1_fwhm   =   0.5895 ±   0.01762
chi²/NDF     =    0.947
```

Figure 34 – ω-scan over 0.5 0.5 0.5 reflection. Solid line is Gaussian fit to the measured data.

Data from IN3 were just fitted with Gaussian profile, as this instrument has only 1D detector. All integrated intensities were corrected for the Lorentz factor.

The obtained raw data were reduced using the program DataRed and the program FullProf was used for the refinement of the structures.

4.4.4.1 Zero field commensurate structure AF1

We have measured two sets of nuclear and magnetic reflections – from horizontal and from vertical magnet. Due to the small window of the high field magnets, only a limited number of reflections was observed. To decrease error of the fitting routine, only strong reflections were used for refinement. Also simulations in FullProf were done in order to see if measured strongest reflections agree with simulated ones.

Data from horizontal and vertical magnet was treated separately because of different background and observed intensities. Extinction correction determined from D10 nuclear measurement was used for all treatments. Number of measured non-equivalent reflections in the different magnets is summarized in Table 16.

The important fact for magnetic structure treatment is that all 16 magnetic reflections measured in vertical magnet was clearly zero. From the 6 possible magnetic structures listed in Table 12, there is only one in which all reflections with $h\ k\ 0$ indices are cancelled out due to the magnetic moment arrangement. It is structure with magnetic moments along c-axis with stacking $+-+-$. The reflections $h\ k\ 0$ were the only one with propagation $\boldsymbol{k} = \left(\frac{1}{2}, 0\ , 0\right)$ which we were able to measure in vertical magnet, so it was not possible to use data from vertical magnet for refinement. The predicted structure was confirmed by refining data from horizontal magnet. Results of FullProf treatments are listed in Table 16.

Table 16 - Summary of FullProf refinement of reflections measured in zero magnetic field on E4

Type of magnet	Horizontal		Vertical	
Type of reflections	Nuclear	Magnetic	Nuclear	Magnetic
Number of measured reflections	7	7	4	16
Scale	65(3)	fixed	29(2)	fixed
μ_{AF1}	-	6.9(2) μ_B	-	??
RF^2	13.7	17.0	13.7	-
RF	10.6	7.91	6.37	-
χ	2.14	0.53	3.81	-

Because of the propagation vector $\boldsymbol{k} = \left(\frac{1}{2}, 0\ , 0\right)$, there exists two *k*-domains or multi-*k* structure in Ho_2RhIn_8. The second domain is connected with the arm $\boldsymbol{k} = \left(0, \frac{1}{2}, 0\right)$. For the treatment in FullProf, only reflections from one domain were used. Considering that both domains are equally populated, we have measured only half of the volume of the sample. The volume of the sample is proportional to the measured intensity, which is proportional to the square of the magnetic moment. Therefore we need to multiply fitted magnetic moment with $\sqrt{2}$. Value in Table 16 is already corrected with this factor.

On the basis of a neutron diffraction experiment it is not possible to distinguish between multi-*k* structure and the existence of magnetic domains. But the multi-*k* structure will imply existence of the holmium atoms with the zero magnetic moment. But this case is unlikely because of magnetization measurements and therefore we conclude that there exist two magnetic k-domains, corresponding to the propagation vectors $\boldsymbol{k} = \left(\frac{1}{2}, 0\ , 0\right)$ and $\boldsymbol{k} = \left(0, \frac{1}{2}, 0\right)$. These domains are equally populated, and application of the external magnetic field along the *c*-axis did not influence this population. Resulting magnetic structure is depicted in Figure 35.

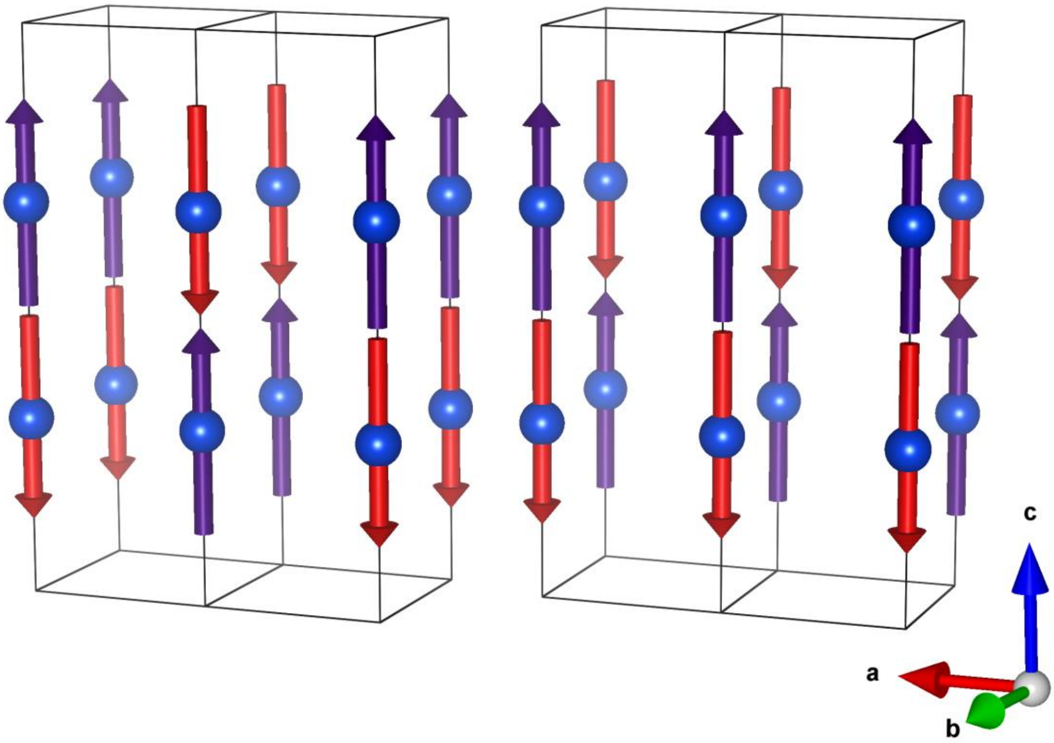

Figure 35 - Magnetic structure of Ho_2RhIn_8 in the AF1 phase. Two magnetic domains are shown.

4.4.4.2 Field induced structure AF2

In order to determine the magnetic structure in the field induced magnetic phase AF2, Bragg reflections were measured in the field of 4 T. The thorough search in the reciprocal space leads to observation of 6 propagation vectors: $\boldsymbol{k}_0 = (0, 0, 0)$, $\boldsymbol{k}_1 = \left(\frac{1}{2}, 0, 0\right)$, $\boldsymbol{k}'_1 = \left(0, \frac{1}{2}, 0\right)$, $\boldsymbol{k}_2 = \left(\frac{1}{2}, 0, \frac{1}{2}\right)$, $\boldsymbol{k}'_2 = \left(0, \frac{1}{2}, \frac{1}{2}\right)$ and $\boldsymbol{k}_3 = \left(\frac{1}{2}, \frac{1}{2}, \frac{1}{2}\right)$, where $\boldsymbol{k}_{1,2}$ and $\boldsymbol{k}'_{1,2}$ correspond to the different magnetic domains. Reciprocal space positions 0.5 0.5 l and $h\,k$ 0.5 were measured for a longer time and no magnetic reflections were found there. The magnetic unit cell size is thus $2a \times 2b \times 2c$.

The sum of the magnetic moments associated with $\boldsymbol{k}_1$ - $\boldsymbol{k}_3$ within magnetic unit cell is always zero, as they are always propagating within *ab*-plane canceling out moments at the 2g Wyckoff site. The magnetization measurements clearly show that the overall magnetic moment in the AF2 phase amounts to the half of the magnetic moment of purely ferromagnetic phase in field above 6 T. This moment must be thus associated with the ferromagnetic component $\boldsymbol{k}_0$ as this is the only one which is not cancelled out.

Results of the theory of representations analysis in chapter 4.4.2 are valid also for the magnetic structures in field. For structures with $\boldsymbol{k}_1$ and $\boldsymbol{k}_2$ there exists always 6 allowed 1D irreducible representations. In case of $\boldsymbol{k}_3$, there is a possibility for the moment to lie in any direction within *ab*-plane. Taking into account the fact that all moments in AF1 points along *c*-axis and a clear field induced spin flip behaviour is observed, we can consider that magnetic moments associated with all wave vectors in AF2 points also along the *c*-axis. Therefore we have two possibilities for each $\boldsymbol{k}$-vector, each with different stacking of the magnetic moments within the nuclear unit cell.

We will now focus on the possible magnetic spin arrangement within ($00z_{\mathrm{Ho}}$) plane. There are four magnetic positions within this plane in the magnetic unit cell, all corresponding to one atom site in the nuclear unit cell. Let’s mark them as on Figure 36.

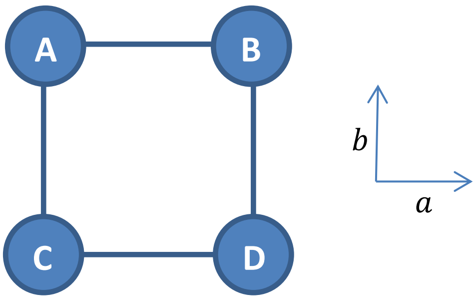

Figure 36 – Schematic view on Ho atoms in *ab*-plane of magnetic unit cell. Each atom position is marked with a letter.

Neglecting out of plane component, there can exist 4 propagation vectors for $2a$ x $2b$ magnetic unit cell in maximum:

$$\boldsymbol{k}_{0,plane} = (0,0),$$

$$\boldsymbol{k}_{1,plane} = \left(\frac{1}{2},0\right),$$

$$\boldsymbol{k}_{2,plane} = \left(0,\frac{1}{2}\right) \text{ and}$$

$$\boldsymbol{k}_{3,plane} = \left(\frac{1}{2},\frac{1}{2}\right).$$

If we neglect the change of the magnitude of the magnetic moment (i.e. imaginary component of basis vector) and assume that the magnetic moments are along *c*-axis, magnitude of the magnetic moments can be calculated by equation (8). Total magnetic moments on individual magnetic atom sites will be:

$$\begin{aligned} \mu_A &= \mu_{\boldsymbol{k}_0} + \mu_{\boldsymbol{k}_1} + \mu_{\boldsymbol{k}_2} + \mu_{\boldsymbol{k}_3}, \\ \mu_B &= \mu_{\boldsymbol{k}_0} - \mu_{\boldsymbol{k}_1} + \mu_{\boldsymbol{k}_2} - \mu_{\boldsymbol{k}_3}, \\ \mu_C &= \mu_{\boldsymbol{k}_0} + \mu_{\boldsymbol{k}_1} - \mu_{\boldsymbol{k}_2} - \mu_{\boldsymbol{k}_3}, \\ \mu_D &= \mu_{\boldsymbol{k}_0} - \mu_{\boldsymbol{k}_1} - \mu_{\boldsymbol{k}_2} + \mu_{\boldsymbol{k}_3}, \end{aligned} \tag{26}$$

where $\mu_{\boldsymbol{k}_{0-3}}$ are magnetic moments associated with relevant propagation vectors.

Considering only spin flip scenario, it is required that total magnetic moments μ_{A-D} on all 4 sites must have the same amplitude. That results in the only possible solution:

$$\mu_{\boldsymbol{k}_0} = \mu_{\boldsymbol{k}_1} = -\mu_{\boldsymbol{k}_2} = \mu_{\boldsymbol{k}_3}, \tag{27}$$

$$\mu_A = -\mu_B = \mu_C = \mu_D = 2\mu_{\boldsymbol{k}_0} \tag{28}$$

which means that one of the four moments in plane is flipped. Magnetic moments arrangement in *ab*-plane is depicted on Figure 37.

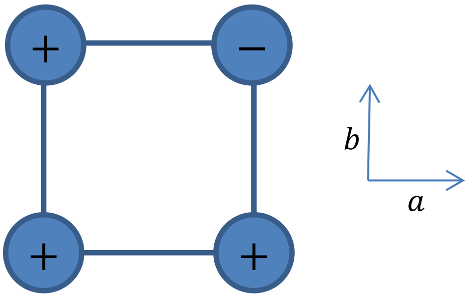

Figure 37 – Magnetic structure in *ab*-plane of Ho_2RhIn_8. Magnetic moments are pointing along *c*-axis.

Extending from the 2D case to the real Ho_2RhIn_8 structure brings more options by different stacking along *c*-axis. Taking into account fact, that total moment at one site cannot exceed theoretical moment of holmium ($10\,\mu_B$), only two independent models summarized in Table 17 and depicted in Figure 38 are possible.

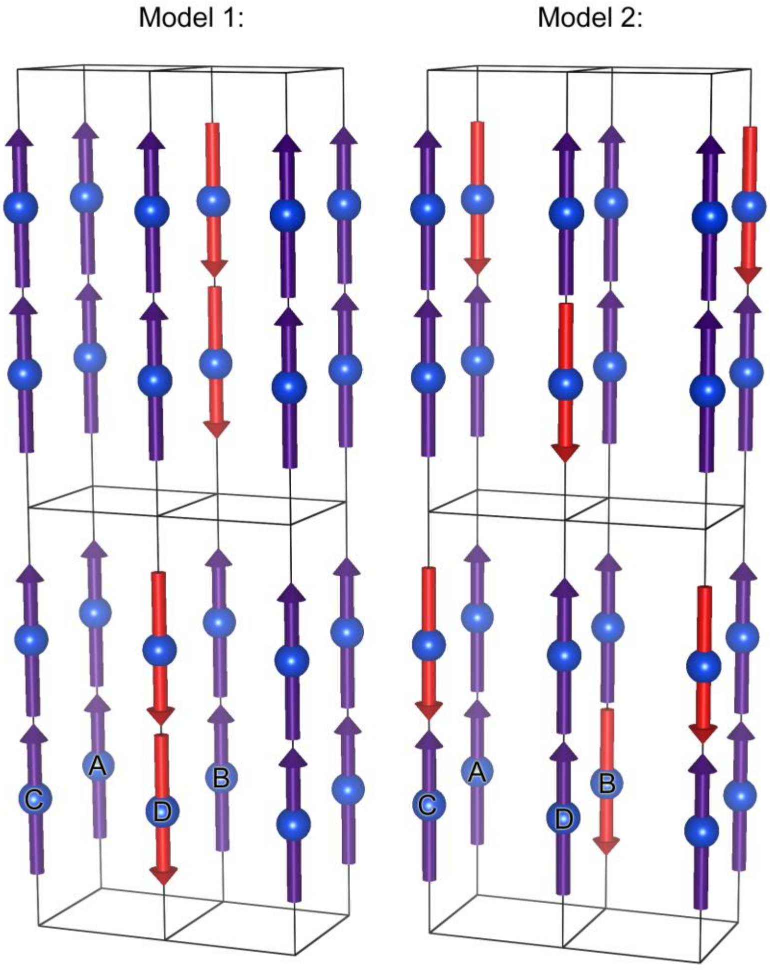

Figure 38 – possible magnetic structures in AF2 phase of Ho_2RhIn_8

Table 17 - Possible magnetic stacking in AF2 phase

	stacking of site A along c-axis	
	model 1	model 2
$k_0 = (0,0,0)$	$++++$	$++++$
$k_1 = \left(\frac{1}{2},0,0\right)$	$++++$	$+-+-$
$k_2 = \left(0,\frac{1}{2},\frac{1}{2}\right)$	$--++$	$-++-$
$k_3 = \left(\frac{1}{2},\frac{1}{2},\frac{1}{2}\right)$	$++--$	$++--$
Overall stacking	$++++$	$+++-$

These models are distinguishable on the same principle as for AF1 phase - on the basis of the existence of the reflections (hk0) for propagation vector $\boldsymbol{k}_1$. These reflections are forbidden in the model 2. As we did not observed any of these reflections, the correct model describing the magnetic structure of Ho_2RhIn_8 in the applied magnetic field (AF2 phase) is the model 2. As well as in AF1, there will exist two magnetic k-domains. The corresponding magnetic structure is depicted in Figure 39.

Quantitative refinement using the FullProf software confirmed results and leads to the magnetic moments listed in Table 18. Treatment was not possible for reflections with propagation k_1 in vertical magnet, since all measured reflections were zero (but this helps to distinguish that model 2 is correct). Treatment was also not possible for the propagation vector $\boldsymbol{k}_3$, since we have reached only 1 magnetic reflection associated with this propagation (due to the construction of magnets).

Table 18 - Summary of FullProf treatment of the measured reflections in AF2 phase of Ho_2RhIn_8

Type of magnet	Horizontal		Vertical			
Propagation vector	$\boldsymbol{k}_0$	$\boldsymbol{k}_1$	$\boldsymbol{k}_0$	$\boldsymbol{k}_1$	$\boldsymbol{k}_2$	$\boldsymbol{k}_3$
Number of measured reflections	7	7	3	16	16	1
Magnetic moment $\mu_{\boldsymbol{k}}$ (μ_B)	3.5(3)	3.7(2)	3.8(6)	?	4.0(2)	?
RF^2	81.7	9.37	40.4	-	22.8	-
RF	44.0	5.26	21.6	-	11.9	-
χ	2.09	0.138	2.86	-	1.06	-

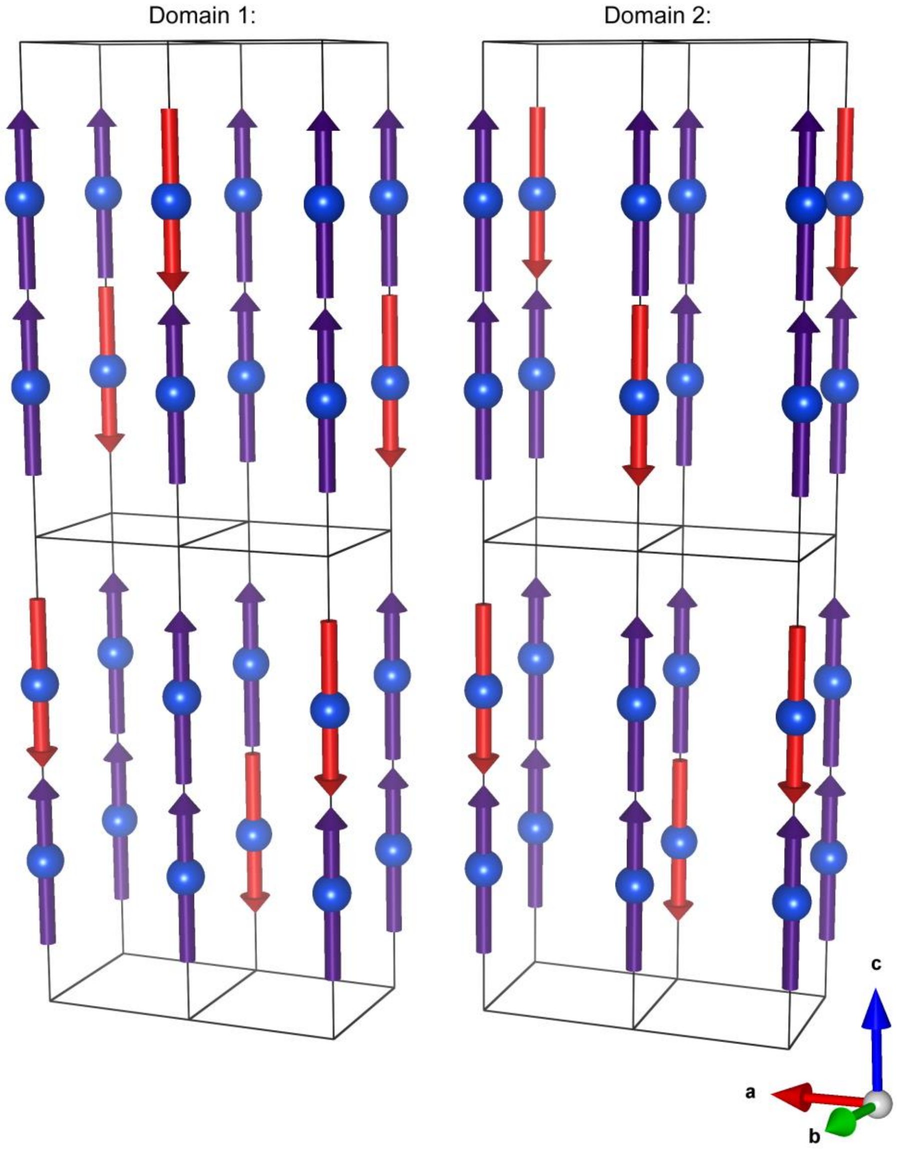

Figure 39 - Magnetic structure of Ho_2RhIn_8 in the AF2 phase. Domain 1 corresponds to $\boldsymbol{k_1} = \left(\boldsymbol{0}, \frac{\boldsymbol{1}}{\boldsymbol{2}}, \boldsymbol{0}\right), \boldsymbol{k_2} = \left(\frac{\boldsymbol{1}}{\boldsymbol{2}}, \boldsymbol{0}, \frac{\boldsymbol{1}}{\boldsymbol{2}}\right)$ and domain 2 corresponds to $\boldsymbol{k_1} = \left(\frac{\boldsymbol{1}}{\boldsymbol{2}}, \boldsymbol{0}, \boldsymbol{0}\right), \boldsymbol{k_2} = \left(\boldsymbol{0}, \frac{\boldsymbol{1}}{\boldsymbol{2}}, \frac{\boldsymbol{1}}{\boldsymbol{2}}\right)$. Both magnetic domains are equally populated.

All four determined amplitudes of magnetic moments satisfy equation (27) within the error. Therefore we can assume that our considerations were correct. Overall amplitude of magnetic moments is therefore $\mu_{AF2} = 7.5(5)\mu_B$, which is calculated from equation (28) taking $\mu_{\boldsymbol{k}_0}$ as mean of all four refined amplitudes of magnetic moments in Table 18. The value of μ_{AF2} is slightly bigger than μ_{AF1}. This increase is due to the impact of the 4 T external magnetic field and is in agreement with the measured magnetization curves (Figure 16).

To clarify the location of the phase boundaries and verify the consistency of the data from the vertical and horizontal magnet, several reflections were followed with the changing magnetic field (Figure 40). We have observed increase of the intensity of the nuclear peaks together with decrease of the peaks associated with $\boldsymbol{k}_1 = \left(\frac{1}{2}, 0, 0\right)$ propagation. Temperature dependence of 0.5 0 1 reflection in the fields of 0, 2 and 3 T is depicted in Figure 45. The shape of the curve in 0 T and 2 T corresponds to each other showing the same ordering mechanism as both are entering the AF1 phase. The crossing of the AF1 phase by the temperature scan in the constant field of 3 T, predicted by magnetic phase diagram (Figure 19) was not observed. This can be explained by the existence of no long-range order in the AF1 phase region at 3 T. Points from the measured temperature and the field dependencies are depicted to the newly constructed phase diagram in Figure 42.

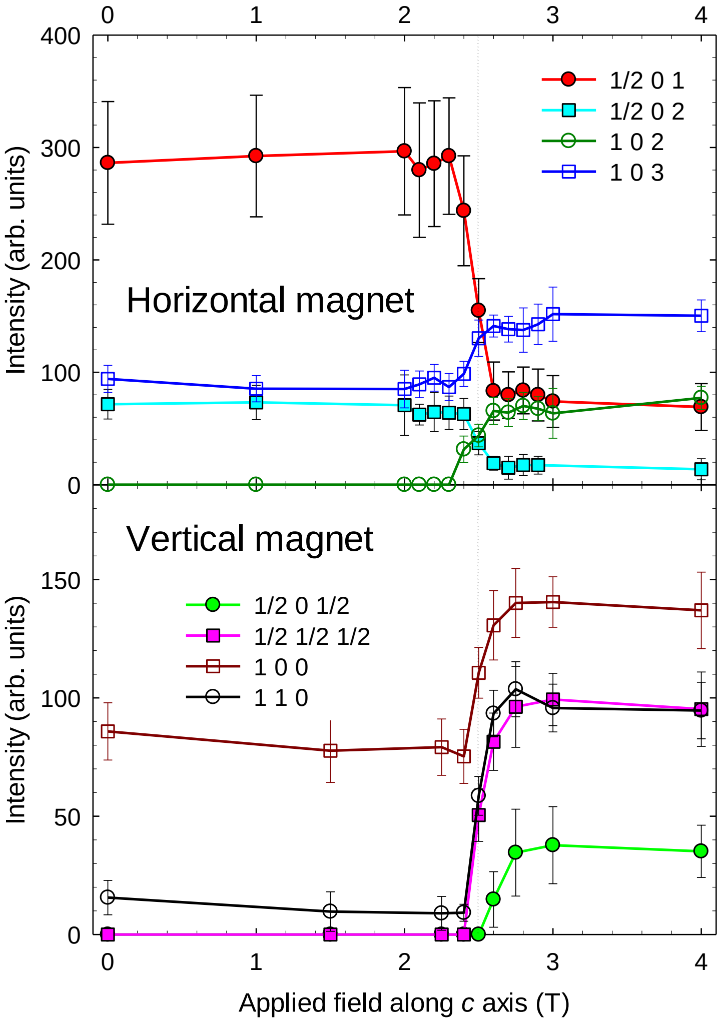

Figure 40 - Field dependence of selected Bragg reflections in horizontal and vertical magnet on E4. Dotted line marks phase transition from magnetization measurements.

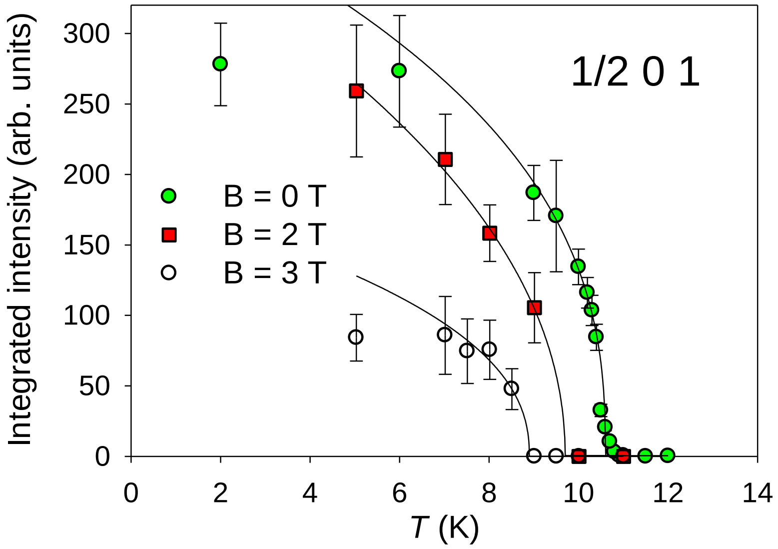

Figure 41 - Temperature dependence of integrated intensity of 1/2 0 1 reflections in different fields. Lines are only to guide the eye.

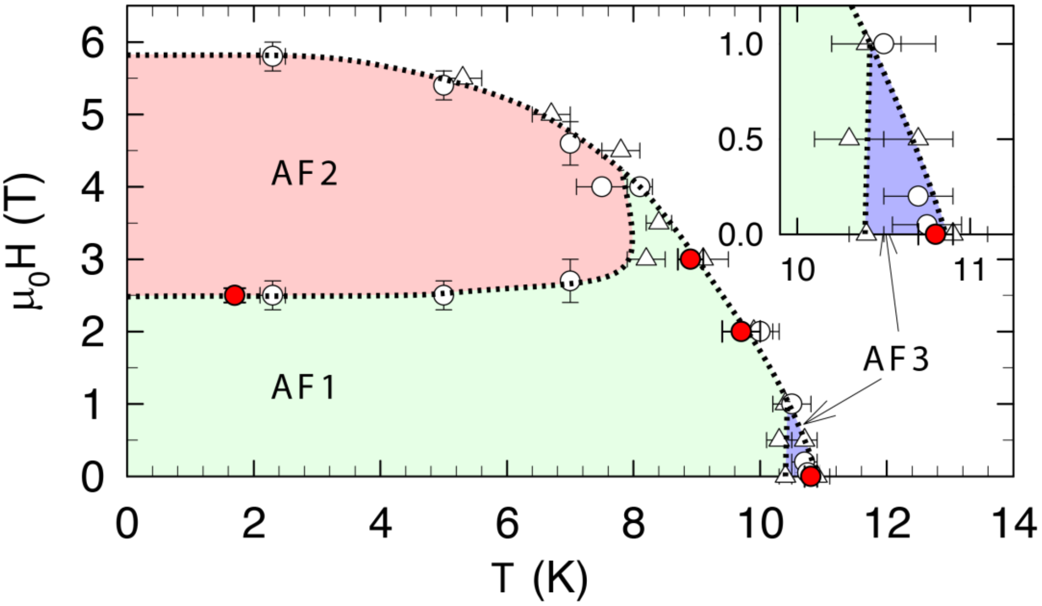

Figure 42 – Magnetic phase diagram of Ho_2RhIn_8 with points from neutron experiments

4.4.4.3 Incommensurate structure AF3

For the determination of the nature of possible AF3 phase, Laue diffractometer CYCLOPS was used. See chapter 4.4.1 for the technical details of the experiment. Ordering in AF3 phase is illustrated in Figure 43, which shows the same small portion of Laue diagrams taken at the same crystal orientation but different temperatures.

At 10.9 K, above the Néel temperature, there is no significant intensity observed. At 10.4 K two satellites appear at incommensurate positions together with a very weak trace of the further commensurate peak. Its intensity starts to grow and at 9.9 K there are clearly both commensurate and incommensurate reflections visible. At 9.4 K is AF3 phase completely vanished. Integrated cut along the curve going through all three reflections are shown in Figure 44. The same behavior was observed also around other strong magnetic reflections and the magnetic peaks on the incommensurate positions were indexed with the propagation vector $\boldsymbol{k}_{AF3} = \left(\frac{1}{2}, \delta, 0\right)$, where $\delta = 0.036(3)$ and is temperature independent.

A very small value of the δ parameter of the propagation vector implies a modulation period involving 27 holmium atoms. Such a long modulation can be explained by formation of a spin density wave phase.

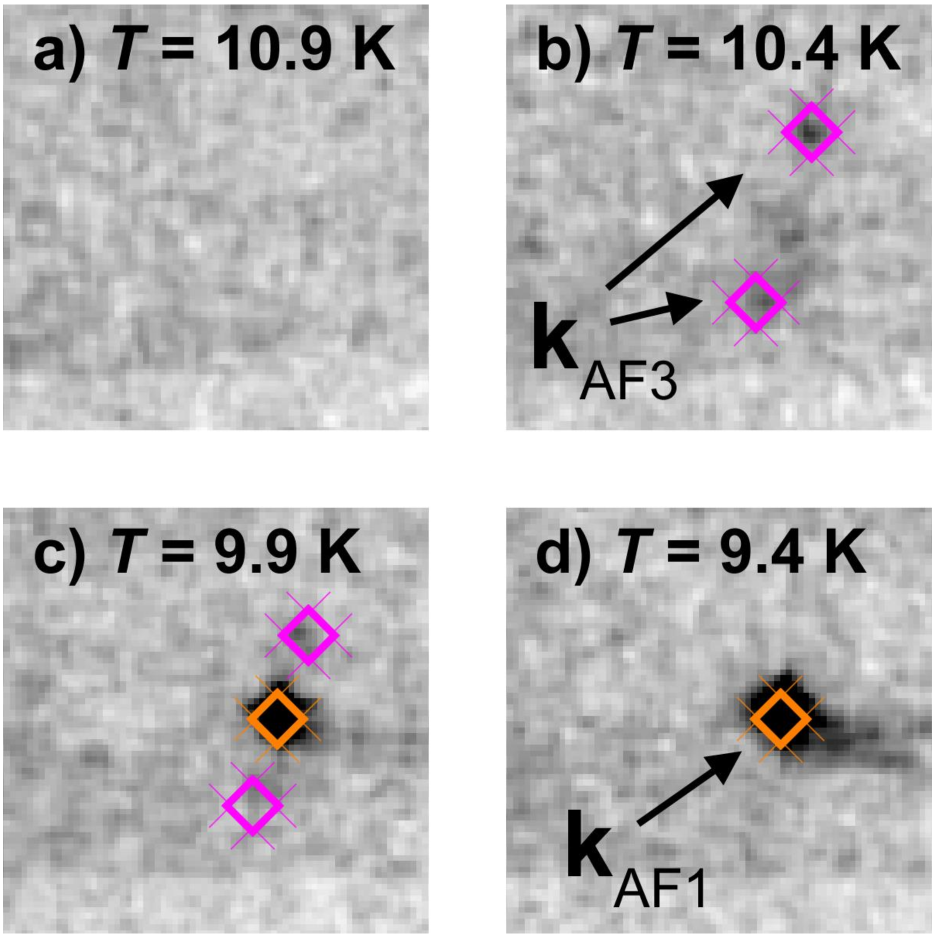

Figure 43 - Detail of the region around 0.5 0 1 reflection in the taken Laue pattern at different temperatures.

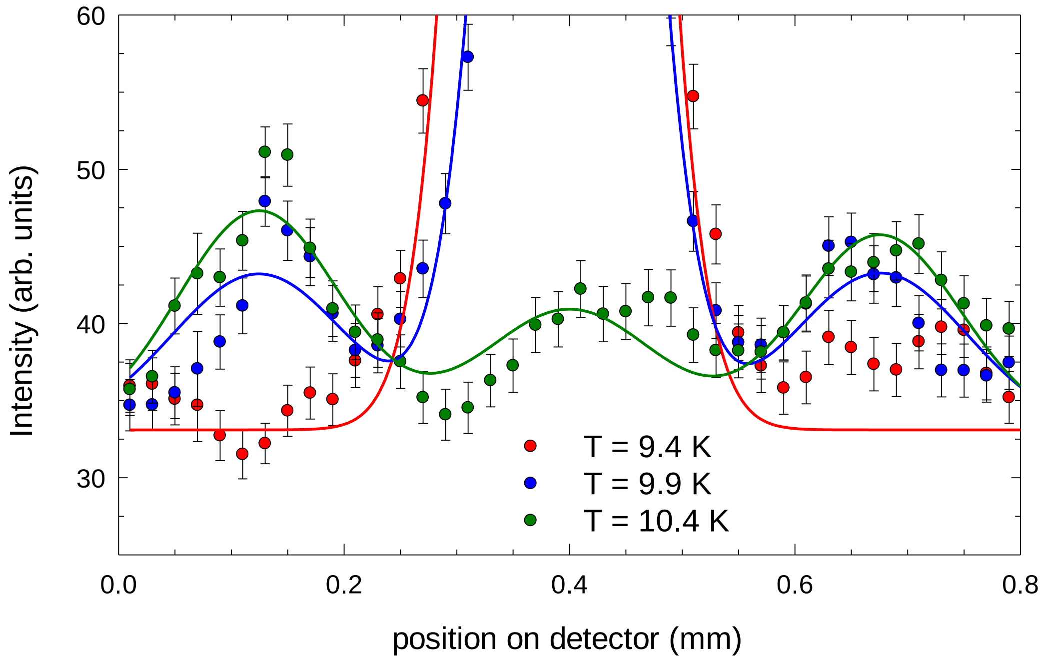

Figure 44 – Laue cuts along the 0h0 crystallographic direction in different temperatures.

4.4.5. Critical behaviour

The temperature dependence of the intensity of the $\left(\frac{1}{2}\ \frac{1}{2}\ \frac{1}{2}\right)$ magnetic reflection for each compound with $\boldsymbol{k} = \left(\frac{1}{2}, \frac{1}{2}, \frac{1}{2}\right)$ and temperature dependence of the intensity $\left(\frac{1}{2}\ 0\ 1\right)$ for Ho_2RhIn_8 is shown in Figure 45. The data were fitted to the power law (24). The determined transition temperatures T_N as well as the critical exponents β are listed in Table 19. These experimental results are incompatible neither with Ising prediction for the two-dimensional and the three-dimensional systems nor with the X-Y or Heisenberg models. However, all four compounds reveal qualitatively similar critical behavior pointing to the similar ordering mechanism with the value of $\beta \sim 0.2$. We are aware, that the determined critical exponents are fitted from the temperature ranges down to 0.8 of the reduced temperature $\frac{T}{T_N}$, which could also explain the deviation from the theoretical values.

Table 19 - Coefficients determined from the critical behavior

R	Nd	Dy	Ho	Er
T_N (K)	10.63(4)	24.24(8)	10.4(2)	3.70(6)
β	0.22(3)	0.20(1)	0.19(4)	0.16(2)

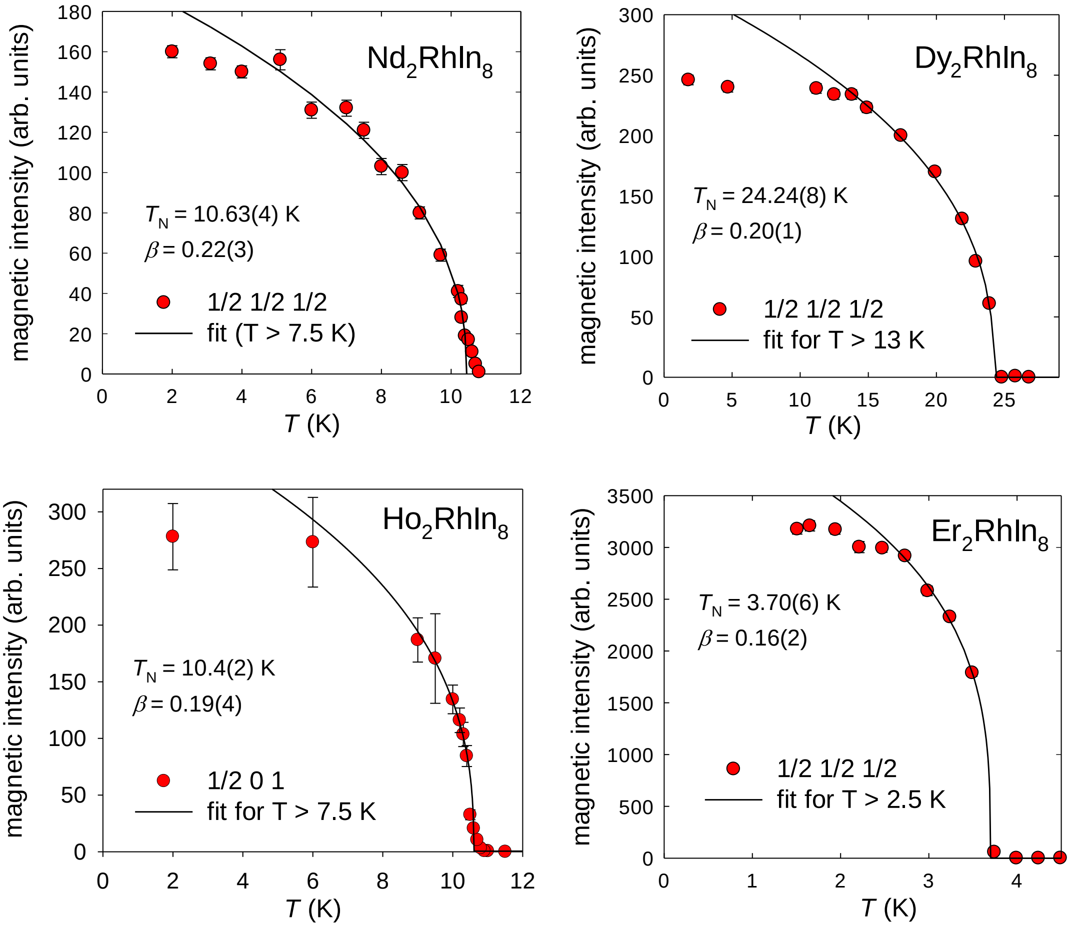

Figure 45 – Temperature dependences of the intensities of selected magnetic reflections. The full lines are fits to the equation (24).

4.4.6. Comparison to the related compounds

Let us now compare our results with the magnetic structures in related compounds. As mentioned in the introduction, the "218" compounds can be seen as transition from the nearly two-dimensional "115" towards the three-dimensional "13" compounds.

4.4.6.1 Nd$_2$RhIn$_8$

In the neodymium compounds the different "13" and "115" magnetic structures were ascribed to competing (NdIn$_3$) or matching (NdRhIn$_5$) crystal-field and exchange anisotropies [64]. The magnetic moments in both Nd$_2$RhIn$_8$ and NdRhIn$_5$ point along the *c*-axis, driven by the crystal-field anisotropy. The coupling between the neighbouring Nd moments is antiferromagnetic within the basal planes, although the moments propagate differently: $k_{\text{in-plane}} = \left(\frac{1}{2}, \frac{1}{2}\right)$ in Nd$_2$RhIn$_8$ and $k_{\text{in-plane}} = \left(\frac{1}{2}, 0\right)$ in NdRhIn$_5$.

The $NdIn_3$ layer (in $NdRhIn_5$) or bilayer (in Nd_2RhIn_8) is then separated by a $RhIn_2$ layer. The Nd-Nd coupling along the *c*-axis across this non-magnetic layer is in both cases also antiferromagnetic. The coupling along the *c*-axis within the cubic $NdIn_3$ blocks in Nd_2RhIn_8 is ferromagnetic, i.e. these cubic blocks form the same magnetic structure occurring in the ground state of $NdIn_3$. The magnetic structure can be viewed also in the following way: among the two nearest Nd layers it acts exactly as in $NdIn_3$ (diagonal propagation in the plane perpendicular to the moments) while another Nd bilayer, separated by $RhIn_2$ layer, is coupled antiferromagnetically creating the overall propagation vector $\boldsymbol{k} = \left(\frac{1}{2}, \frac{1}{2}, \frac{1}{2}\right)$.

4.4.6.2 Dy_2RhIn_8

Similar conclusions are valid for dysprosium compound, except the fact that in the cubic $DyIn_3$ the magnetic moments point out of the main crystallographic directions. The recently studied gallium analogue of the dysprosium compound, Dy_2CoGa_8, shows the same magnetic structure and stacking along the *c*-axis [83]. Stacking of moments along the c-axis $+ + - -$ in Dy_2RhIn_8 is different from the stacking $+ - + -$ revealed for Tb_2RhIn_8 [72]. This is then reflected in the qualitatively different magnetization curves in magnetic fields above 10 T applied along the a-axis [99].

4.4.6.3 Ho_2RhIn_8

Ho_2RhIn_8 is a first member of "218" compound with magnetic domains. Others have propagation $\boldsymbol{k} = \left(\frac{1}{2}, \frac{1}{2}, \frac{1}{2}\right)$, which excludes existence of magnetic moments. Its structure is much more similar to "115" compounds, having same stacking along *c*-axis and also same propagation within *ab*-plane. As this is the first solved AF2 structure in this family of compounds, we cannot compare results to the related ones.

We suppose, that due to the similar phase diagrams, related compounds from "218" family will perform the same flipping mechanism during metamagnetic transition from AF1 to AF2, consisting of the flip of 1/4 of the magnetic moments. Same could be applied with a small modification to "115" compounds, as the AF1 structure in Ho_2RhIn_8 is very similar to the known "115" magnetic structures. Magnetic structure suggested for AF2 phase in "115" compounds mentioned in Hieu's thesis [6], see Figure 46(c), corresponds to the model determined for the AF2 phase in Ho_2RhIn_8.

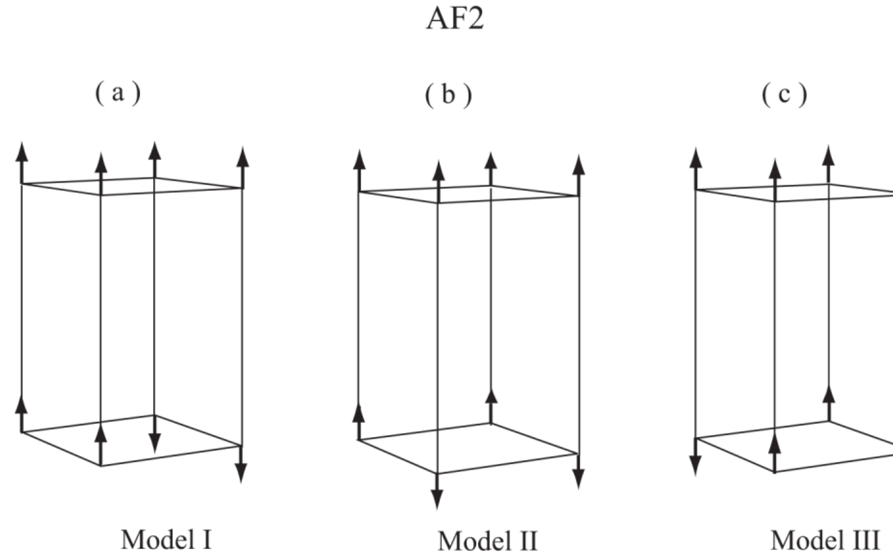

Figure 46 - Three types of magnetic structure in AF2 for *R*RhIn$_5$, figure taken from [6], where it is Fig. 5.69.

Formation of the incommensurate zero-field phase is also unique within "218" and "115" compounds, but can be found in other tetragonal compounds as UCu$_2$Si$_2$ [98].

4.4.6.4 Er$_2$RhIn$_8$

No magnetic structure is reported for any of the erbium 115 compounds. We can compare our results to the gallium analogue Er$_2$CoGa$_8$, which has $= \left(0, \frac{1}{2}, 0\right)$, i.e. it propagates only along the direction of the magnetic moments with $+-+-$ stacking along the c-axis. This qualitative change of stacking within the unit cell as well as different propagation vector is probably caused by the smaller distance between Er atoms in the gallium compound (4.2287 Å in Er$_2$CoGa$_8$ [61] compared to 4.5284 Å in Er$_2$RhIn$_8$). The determined amplitude of the magnetic moment in the gallium compound $4.7\mu_B$ is also significantly reduced in comparison with $6.4\ \mu_B$ for its indium relative.

The small value of $\beta = 0.16$ for Er$_2$RhIn$_8$ is rather different from the value $\beta = 0.33$ determined for isostructural Er$_2$CoGa$_8$ [61]. We observe a significantly steeper increase of the spontaneous magnetization compared to the gallium-based compound, although both materials share a similar magnetic structure. To illustrate this discrepancy, we have plotted temperature dependencies for both related compounds do the Figure 47. To allow compare compound with different intensities and transition temperatures, both axis were normalized to the same values.

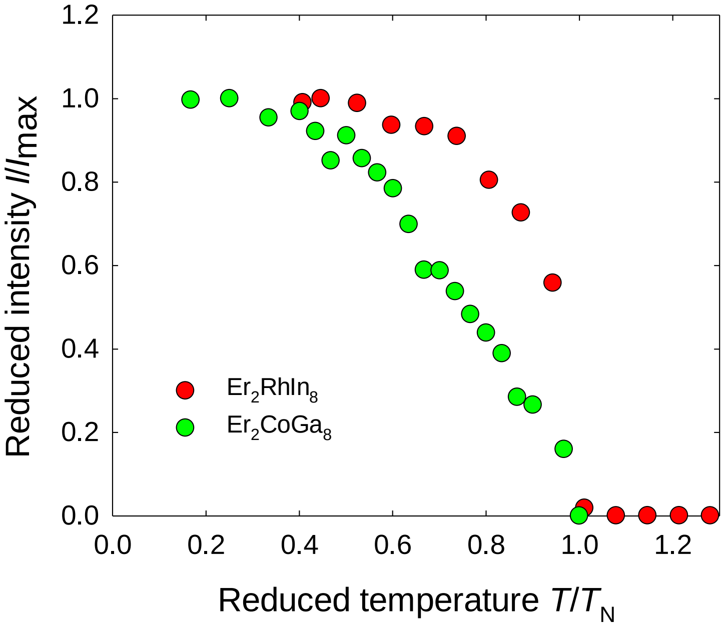

Figure 47 –Comparison of the critical behavior of gallium and indium compound. Data for Er_2CoGa_8 are taken from [61].

4.4.6.5 Tm_2RhIn_8

The incommensurate behavior is unique among non-cerium compounds and the only compound with incommensurate magnetic structure is $CeRhIn_5$ (see Table 2 and Table 4 for list of existing magnetic structures in the related compounds). It orders with propagation vector $\boldsymbol{k} = \left(\frac{1}{2}, \frac{1}{2}, 0.297\right)$ producing a magnetic structure with moments lying within an *ab*-plane, where they form a simple nearest-neighbor antiferromagnetic on a square lattice. Magnetic moments then spiral transversely along the *c*-axis with an incommensurate pitch $\delta = 0.297$ [49]. See Figure 48 for detailed picture of this magnetic structure.

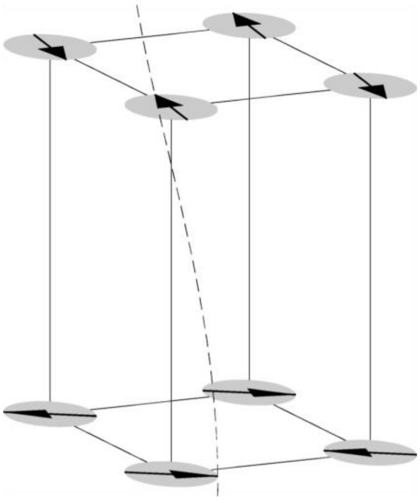

Figure 48 - Magnetic structure of $CeRhIn_5$. The disk denotes the moment rotating plane. The dashed line traces the spiral. Image taken from [49].

Tm_2RhIn_8 can adopt the similar magnetic structure as $CeRhIn_5$ with the incommensurate propagation along the c-axis, only with different propagation within ab-plane. The incommensurate character of $CeRhIn_5$ is ascribed to Fermi-surface nesting [103], which could be also possible in Tm_2RhIn_8. To continue with this discussion, further neutron experiments are needed to clarify exact propagation and also the details of the magnetic structure in Tm_2RhIn_8. Our experiment on the single crystal diffractometer on this compound was cancelled due to problems with cooling, so a detailed magnetic structure of Tm_2RhIn_8 remains unknown.

4.4.6.6 Overall comparison

In all four compounds where the amplitude of the magnetic moment was determined, this value is reduced from the expected values of the free ion. It is in agreement with other compounds from related series [61, 83, 6]. This is typical for tetragonal CEF driven magnetic structures [104], for example $DyCo_2Si_2$ [100]. Interpolating the measured magnetization curves along the c-axis to zero magnetic field for Nd_2RhIn_8, Dy_2RhIn_8 and Ho_2RhIn_8 gives the values of 2.2, 7.2 and 7.6 μ_B per R atom (see [99] and Figure 16), respectively, which are in good agreement with our experimental values.

Doing the same for Er_2RhIn_8 leads to the value of 7.8 μ_B per Er for the magnetic field applied along the [110] direction and to the value of 6.9 μ_B per Er for the magnetic field applied along the [100] direction (see Figure 17). From the representation analysis it is clear that $irrep$ Γ_{10} is always connected with lowering of the symmetry and creation of the magnetic domains. That is the reason, why the values from bulk magnetization measurements are bigger than the value of 6.4 μ_B obtained from the neutron diffraction.

The magnetic structures in the corresponding cerium compounds are more complex. An incommensurate spiral structure, with Ce moments within the ab-planes, is observed in $CeRhIn_5$ [49]. The magnetic structure of Ce_2RhIn_8 is described by the propagation vector $\boldsymbol{k} = \left(\frac{1}{2}, \frac{1}{2}, 0\right)$ and Ce moments pointing 38° out of the tetragonal c-axis. The coupling within the basal planes is the same as in Nd_2RhIn_8, but the coupling along the c-axis is different: it is antiferromagnetic across the non-magnetic $RhIn_2$ layer as well as within the cubic $CeIn_3$ blocks. The main difference is however the moment direction. Thus, the resulting structure lowers the symmetry by mixing two representations within the same exchange multiplet [105]. We assume that this is the consequence of stronger isotropic exchange interactions with respect to the anisotropy in the Ce compound.

Conclusion

We have measured the specific heat, magnetization and neutron diffraction in R_2RhIn$_8$ compounds. Based on these results we have constructed phase diagrams and we have determined their magnetic structures. We summarize our research as follows:

1. We have grown single crystals of R_2RhIn$_8$ (R = Nd, Tb, Dy, Ho, Er, Tm, La, Lu, Y) with good purity and without additional phases. Single crystal X-Ray diffraction experiments shown, that all crystallize in the tetragonal structure with Ho_2CoGa_8-structure type and space group P4/mmm. In view of that fact, they are isostructural relatives to Ce_2TIn$_8$ group of heavy fermion superconductors (T is transition metal).
2. We have confirmed predictions from related groups of compounds, that magnetism in these materials is driven by crystal field effects, which strongly influences easy magnetization axis in these materials. The compounds with Nd, Tb, Dy and Ho have negative second order Stevens constant α_j and reveal easy magnetization axis along tetragonal *c* direction. On the other hand, Tm and Er compounds have this coefficient positive and their easy magnetization axis lies within *ab*-plane.
3. We have constructed field vs. temperature phase diagrams of compounds with easy magnetization axis along tetragonal *c*-axis. Generally, these compounds reveal one zero-field commensurate antiferromagnetic phase, AF1. By applying magnetic field along c-axis, they pass sharp metamagnetic transition to commensurate ferrimagnetic phase AF2. During this transition, half of the ordered spins of AF1 is flipped into the direction of the magnetic field, forming additional propagations. With higher magnetic field, compounds undergo second metamagnetic transition to field-induced ferromagnetically ordered phase. Overall bulk magnetic moment in AF2 is always exactly half of the full ferromagnetic moment, confirming the spin flip scenario with the half of the spins flipped. Constructed phase diagrams are qualitatively similar as in related “115” and “218” compounds and also in compounds with the structure of $CeCu_2Si_2$.

4. In addition, Ho_2RhIn_8 reveals small region of zero field incommensurate spin density wave structure before forming commensurate ferromagnetic ground state. This behaviour is unique among the related compounds.
5. We have determined details of the magnetic structure of Nd_2RhIn_8, Dy_2RhIn_8, Ho_2RhIn_8, Er_2RhIn_8 and partially Tm_2RhIn_8. Nd, Dy and Er compounds have commensurate structure, with $\boldsymbol{k} = \left(\frac{1}{2}, \frac{1}{2}, \frac{1}{2}\right)$ and size of the magnetic moments $2.53(9)$, $6.9(3)$ and $6.4(1.4)$ μ_B respectively, in agreement with related "218" compounds. Ho_2RhIn_8 reveals magnetic structure with propagation vector $\boldsymbol{k} = \left(\frac{1}{2}, 0{,}0\right)$ and the ordered moments with amplitude of $6.9(2)$ μ_B.

   Tm_2RhIn_8 is unique from the series with incommensurate propagation along tetragonal axis, $\boldsymbol{k} = \left(\frac{1}{2}, 0, 0.42\right)$. Its magnetic structure could be similar to the structure found in $CeRhIn_5$.
6. We have determined magnetic structure in the field induced phase of Ho_2RhIn_8 with the ordered moment of $7.5(5)$ μ_B. Because of many similarities with related compounds, we predict that similar field induced magnetic structure will be also present in related compounds.

In conclusion, we summarize that detailed systematic study of the R_2RhIn_8 group of compounds showed important similarities with the related "115" and "218" compounds, but we even found the similar behaviours in "122" compounds related to $CeCu_2Si_2$. We hope that our research will help in revealing basic principles of heavy fermion superconductivity.

Bibliography

1. HEGGER, H. et al. Pressure-Induced Superconductivity in Quasi-2D CeRhIn5. *Phys. Rev. Lett*. 2000, **84**, 4986-89.
2. PETROVIC, C. et al. Heavy-fermion superconductivity in CeCoIn 5 at 2.3 K. *J. Phys.: Condens. Matter*. 2001, **13**, L337.
3. PETROVIC, C. et al. A new heavy-fermion superconductor CeIrIn 5 : A relative of the cuprates? *Europhys. Lett*. 2001, **53**, 354.
4. THOMPSON, J. D. and FISK, Z. Progress in Heavy-Fermion Superconductivity: Ce115 and Related Materials. *J. Phys. Soc. Jpn*. 2012, **81**, 011002.
5. OTT, H. R., RUDIGIER, H., RICE, T. M., UEDA, K., FISK, Z. and SMITH, J. L. p-Wave Superconductivity in UBe13. *Phys. Rev. Lett*. 1984, **52**, 1915-18.
6. HIEU, N. V. *Single Crystal Growth and Magnetic Properties of RRhIn5 Compounds (R: Rare Earths)*. 2007. PhD thesis.
7. FREEMAN, A. J. and WATSON, R. E. Theoretical Investigation of Some Magnetic and Spectroscopic Properties of Rare-Earth Ions. *Phys. Rev.*. 1962, **127**, 2058-75.
8. MACKINTOSH, A. R. and JENSEN, J. *Rare Earth Magnetism*. Oxford: Clarendon Press, 1991.
9. ANDRES, K., GRAEBNER, J. E. and OTT, H. R. 4f-Virtual-Bound-State Formation in CeAl3 at Low Temperatures. *Phys. Rev. Lett*. 1975, **35**, 1779-82.
10. STEGLICH, F. et al. Superconductivity in the Presence of Strong Pauli Paramagnetism: CeCu2Si2. *Phys. Rev. Lett*. 1979, **43**, 1892-96.
11. FEYERHERM, R. et al. Coexistence of Local Moment Magnetism and Heavy-Fermion Superconductivity in UPd2Al3. *Phys. Rev. Lett*. 1994, **73**, 1849-52.
12. FEYERHERM, R. et al. On the competition between superconductivity and magnetism in CeCu2Si2. *Physica B*. 1995, **206–207**, 596-99. Available online: http://www.sciencedirect.com/science/article/pii/0921452694005309
13. WILLS, A. Magnetic structures and their determination using group theory. *J. Phys. IV France*. 2001, **11**, Pr9-133-Pr9-158. Available online: http://dx.doi.org/10.1051/jp4:2001906
14. UHLÍŘOVÁ, K. *Single crystal studies of Novel Strongly Correlated Electron Compounds*. 2010. PhD thesis. Charles University.
15. MARTIN, C. A. Simple treatment of anharmonic effects on the specific heat. *J. Phys.: Condens. Matter*. 1991, **3**, 5967.
16. HWANG, J. S., LIN, K. J. and TIEN, C. Measurement of heat capacity by fitting the whole temperature response of a heat-pulse calorimeter. *Rev. Sci. Instrum*. 1997, **68**, 94 - 101.
17. ČERMÁK, P. *Magnetic properties of Ce compounds studied by specific heat*. 2010. Diploma thesis. Charles University.
18. WASEDA, Y., MATSUBARA, E. and SHINODA, K. *X-Ray Diffraction Crystallography: Introduction, Examples and Solved Problems*. 2011. ISBN 9783642166358.
19. MAEDA, K. and MIZUBAYASHI, H. Nanoscopic Architecture and

Microstructure. Springer Berlin Heidelberg. ISBN 978-3-540-20785-6.

20. WILKINSON, C., KHAMIS, H. W., STANSFIELD, R. F. D. and MCINTYRE, G. J. Integration of single-crystal reflections using area multidetectors. *J. Appl. Cryst*. 1988, **21**, 471-78. Software Argonne_Boxes is available on some instruments at ILL.
21. FILHOL, A. Program for the refinement of the UB-matrix, wavelength, cell parameters and instrument zero-shifts …. In: *ILL87FI19T*. ILL internal reports. 1987.
22. MCINTYRE, G. J. and STANSFIELD, R. F. D. A general Lorentz correction for single-crystal diffractometers. *Acta Cryst*. 1988, **44**, 257-62.
23. IIZUMI, M. Lorentz Factor in Single-Crystal Neutron Diffraction. *Jpn. J. Appl. Phys.*. 1973, **12**, 167-72.
24. PROKEŠ, K. *private communication*.
25. ZACHARIASEN, W. H. The secondary extinction correction. *Acta Cryst*. 1963, **16**, 1139-44.
26. ZACHARIASEN, W. H. A general theory of X-ray diffraction in crystals. *Acta Cryst*. 1967, **23**, 558-64.
27. COPPENS, P. et al. *Absorbtion correction program DATAP*. Available online: https://forge.epn-campus.eu/projects/sxtalsoft/wiki/Datap
28. BECKER, P. J. and COPPENS, P. Extinction within the limit of validity of the Darwin transfer equations. I. General formalism for …. *Acta Cryst*. 1974, **30**, 129-47.
29. RODRÍGUEZ-CARVAJAL, J. Recent advances in magnetic structure determination by neutron powder diffraction. *Physica B*. 1993, **192**, 55-69.
30. DIANOUX, A. J., LANDER, G. H., INSTITUT MAX VON LAUE, P. L. G. and LAUE-LANGEVIN, I. *Neutron Data Booklet*. Old City, 2001. Available online: http://books.google.de/books?id=HxAUHQAACAAJ
31. COPPENS, P. The Evaluation of Absorption and Extinction in Single Crystal Structure Analysis. Munksgaard, 1970. ISBN 9788716001795. Available online: http://books.google.de/books?id=fCS7WoChrfgC
32. ALDRED, A. T., PLESSIS, P. d. d. and LANDER, G. H. Critical exponents of uranium telluride. *J. Magn. Magn. Mater*. 1980, **20**, 236 - 242. Available online: http://www.sciencedirect.com/science/article/pii/0304885380904400
33. BRUSH, S. G. History of the Lenz-Ising Model. *Rev. Mod. Phys*. 1967, **39**, 883-93.
34. ECKERT, M. Max von Laue and the discovery of X-ray diffraction in 1912. *Ann. Phys*. 2012, **524**, A83-85.
35. MCINTYRE, G. J., LEMÉE-CAILLEAU, M.H. and WILKINSON, C. High-speed neutron Laue diffraction comes of age. *Physica B*. 2006, **385-386, Part 2**, 1055-58.
36. OULADDIAF, B., ARCHER, J., MCINTYRE, G. J., HEWAT, A. W., BRAU, D. and YORK, S. OrientExpress: A new system for Laue neutron diffraction. *Physica B*. 2006, **385-386, Part 2**, 1052-54.
37. OULADDIAF, B. et al. CYCLOPS - a reciprocal-space explorer based on CCD neutron detectors. *J. Appl. Cryst*. 2011, **44**, 392-97.
38. SWINNEA, S. Lecture ChE 386K [online]. 2001. Available online: http://

capsicum.me.utexas.edu/ChE386K/html/laue_geometry.htm

39. FUENTES-MONTERO, L., ČERMÁK, P. and RODRIGUEZ-CARVAJAL, J. Esmeralda. see http://forge.ill.fr/projects/sxtalsoft/ for source code.
40. WALKER, F. J. and ICE, G. E. Automatic Indexing of Laue Images by Pattern Recognition. Oak Ridge National Laboratory, 2000. MHATT-CAT Contributions to the 2000 APS Activity Report.
41. CHUNG, J.S. and ICE, G. E. Automated indexing for texture and strain measurement with broad-bandpass x-ray microbeams. *J. Appl. Phys*. 1999, **86**, 5249-55.
42. WALKER, I. R., GROSCHE, F. M., FREYE, D. M. and LONZARICH, G. G. The normal and superconducting states of CeIn3 near the border of antiferromagnetic order. *Physica C*. 1997, **282-287, Part 1**, 303 - 306.
43. KURENBAEVA, Z. M., MURASHOVA, E. V., SEROPEGIN, Y. D., NOËL, H. and TURSINA, A. I. The crystal structure of the new indide CePt2In7 from powder data. *Intermetallics*. 2008, **16**, 979 - 981.
44. TURSINA, A., NESTERENKO, S., SEROPEGIN, Y., NOËL, H. and KACZOROWSKI, D. Ce2PdIn8, Ce3PdIn11 and Ce5Pd2In19 - members of homological series based on AuCu3- and PtHg2-type …. *J. Solid State Chem*. 2013, **200**, 7-12. Available online: http://www.sciencedirect.com/science/article/pii/S0022459613000091
45. SARRAO, J. L. and THOMPSON, J. D. Superconductivity in Cerium- and Plutonium-Based 115 Materials. *J. Phys. Soc. Jpn*. 2007, **76**, 051013. Available online: http://jpsj.ipap.jp/link?JPSJ/76/051013/
46. BENOIT, A., BOUCHERLE, J., CONVERT, P., FLOUQUET, J., PALLEAU, J. and SCHWEIZER, J. Magnetic structure of the compound CeIn3. *Solid State Commun*. 1980, **34**, 293-95.
47. MATHUR, N. et al. Magnetically mediated superconductivity in heavy fermion compounds. *Nature*. Nature Publishing Group, 1998, **394**, 39-43.
48. MOVSHOVICH, R. et al. Unconventional Superconductivity in CeIrIn5 and CeCoIn5: Specific Heat and Thermal Conductivity …. *Phys. Rev. Lett*. 2001, **86**, 5152-55.
49. BAO, W. et al. Incommensurate magnetic structure of CeRhIn5. *Phys. Rev. B*. 2000, **62**, R14621-24.
50. BAO, W. et al. Erratum: Incommensurate magnetic structure of CeRhIn5 [Phys. Rev. B 62 , R14 621 (2000)]. *Phys. Rev. B*. 2003, **67**, 099903.
51. KENZELMANN, M. et al. Coupled Superconducting and Magnetic Order in CeCoIn5. *Science*. 2008, **321**, 1652-54.
52. RAYMOND, S., RAMOS, S. M., AOKI, D., KNEBEL, G., MINEEV, V. P. and LAPERTOT, G. Magnetic Order in Ce0.95Nd0.05CoIn5: The Q-Phase at Zero Magnetic Field. *J. Phys. Soc. Jpn*. 2014, **83**, 013707.
53. SCHENCK, A., GYGAX, F. N., UEDA, T. and ONUKI, Y. Magnetic structure of Ce2RhIn8: Evidence for ordered moments on the Rh sites. *Phys. Rev. B*. 2004, **70**, 054415.
54. CHEN, G. et al. Observation of Superconductivity in Heavy-Fermion Compounds of Ce2CoIn8. *J. Phys. Soc. Jpn*. 2002, **71**, 2836-38. Available online: http://jpsj.ipap.jp/link?JPSJ/71/2836/

55. THOMPSON, J. D. et al. Superconductivity and magnetism in a new class of heavy-fermion materials. *J. Magn. Magn. Mater*. 2001, **226–230, Part 1**, 5-10. Available online: http://www.sciencedirect.com/science/article/pii/S0304885300006028

56. KACZOROWSKI, D., GNIDA, D., PIKUL, A. P. and TRAN, V. H. Heavy-fermion superconductivity in Ce2PdIn8. *Solid State Commun.*. 2010, **150**, 411-14. Available online: http://www.sciencedirect.com/science/article/pii/S0038109809007522

57. UHLÍŘOVÁ, K., PROKLEŠKA, J., SECHOVSKÝ, V. and DANIŠ, S. Solution growth of Ce–Pd–In single crystals: Characterization of the heavy-fermion superconductor …. *Intermetallics*. 2010, **18**, 2025 - 2029. Available online: http://www.sciencedirect.com/science/article/pii/S0966979510001457

58. DONG, J. K. et al. Field-Induced Quantum Critical Point and Nodal Superconductivity in the Heavy-Fermion …. *Phys. Rev. X*. American Physical Society, 2011, **1**, 011010. Available online: http://link.aps.org/doi/10.1103/PhysRevX.1.011010

59. KRATOCHVÍLOVÁ, M. *private communication*.

60. BAUER, E. D. et al. Pressure-induced superconducting state and effective mass enhancement near the antiferromagnetic …. *Phys. Rev. B*. 2010, **81**, 180507.

61. JOHNSON, R. D. et al. Magnetic structures of the anisotropic intermetallic compounds Er2CoGa8 and Tm2CoGa8. *Phys. Rev. B*. 2010, **82**, 104407.

62. GÖRLICH, E. et al. Mössbauer effect studies in EuIn3 and EuPb3. *Phys. Status Solidi A*. 1975, **30**, K17-20. Available online: http://dx.doi.org/10.1002/pssa.2210300151

63. AMARA, M., GALÉRA, R., MORIN, P., VERES, T. and BURLET, P. Incommensurate antiferromagnetic structures in NdIn3. *J. Magn. Magn. Mater*. 1994, **130**, 127 - 132.

64. CHANG, S. et al. Magnetic structure of antiferromagnetic NdRhIn5. *Phys. Rev. B*. 2002, **66**, 132417.

65. PAGLIUSO, P. G., THOMPSON, J. D., HUNDLEY, M. F. and SARRAO, J. L. Crystal-field-induced magnetic frustration in NdMIn5 and Nd2MIn8 (M=Rh, Ir) antiferromagnets. *Phys. Rev. B*. American Physical Society, 2000, **62**, 12266-70. Available online: http://link.aps.org/doi/10.1103/PhysRevB.62.12266

66. BUSCHOW, K. H. J., WIJN, H. W. d. and DIEPEN, A. M. v. Magnetic Susceptibilities of Rare-Earth-Indium Compounds: RIn3. *J. Chem. Phys.* AIP, 1969, **50**, 137-41. Available online: http://link.aip.org/link/?JCP/50/137/1

67. PAGLIUSO, P. G., THOMPSON, J. D., HUNDLEY, M. F., SARRAO, J. L. and FISK, Z. Crystal structure and low-temperature magnetic properties of R(m)MIn(3m+2) compounds (M=Rh or Ir; …. *Phys. Rev. B*. American Physical Society, 2001, **63**, 054426. Available online: http://link.aps.org/doi/10.1103/PhysRevB.63.054426

68. MALACHIAS, A., GRANADO, E., LORA-SERRANO, R., PAGLIUSO, P. G. and PÉREZ, C. A. Spin structure and first-order transition of GdIn3: Near-surface magnetism, buried …. *Phys. Rev. B*. 2008, **77**, 094425.

69. GRANADO, E., UCHOA, B., MALACHIAS, A., LORA-SERRANO, R., PAGLIUSO, P. G. and WESTFAHL, H. Magnetic structure and critical

behavior of GdRhIn5: Resonant x-ray diffraction and renormalization …. *Phys. Rev. B*. 2006, **74**, 214428.

70. NERESON, N. and ARNOLD, G. Magnetic Properties of TbIn3, TbPt3 and HoIn3. *J. Chem. Phys*. 1970, **53**, 2818-23.
71. LORA-SERRANO, R. et al. Magnetic structure and enhanced T_N of the rare-earth intermetallic compound TbRhIn5: Experiments …. *Phys. Rev. B*. American Physical Society, 2006, **74**, 214404.
72. LORA-SERRANO, R. et al. Structurally tuned magnetic properties of TbmRhnIn3m+2n (m=1,2; n=0,1) intermetallic …. *Physica B*. 2006, **384**, 326-28.
73. ARNOLD, G. and NERESON, N. Magnetic Properties of DyPt3 and DyIn3. *J. Chem. Phys.* AIP, 1969, **51**, 1495-99.
74. CZOPNIK, A., MÄDGE, H. and STALIńSKI, B. Anomalous strong divergence of the specific heat of ErIn3 at the antiferromagnetic transition. *Phys. Status Solidi A*. 1988, **107**, K151-55.
75. MURASIK, A., CZOPNIK, A., KELLER, L. and KONTER, T. Low Temperature Magnetic Behaviour of TmIn3. *Phys. Status Solidi A*. 2002, **189**, R7-R9.
76. HIEU, N. V. et al. Fermi Surface and Magnetic Properties of PrTIn5 (T: Co, Rh, and Ir). *J. Phys. Soc. Jpn*. 2005, **74**, 3320-28. Available online: http://jpsj.ipap.jp/link?JPSJ/74/3320/
77. DUQUE, J. et al. Field induced phase transitions on NdRhIn5 and Nd2RhIn8 antiferromagnetic compounds. *J. Magn. Magn. Mater*. 2011, **323**, 954 - 956.
78. ADRIANO, C., GILES, C., COELHO, L., FARIA, G. and PAGLIUSO, P. Magnetic structure of Ho2CoGa8 determined by X-ray resonant magnetic scattering. *Physica B*. 2009, **404**, 3289 - 3292.
79. TOKUNAGA, Y. et al. NMR determination of noncollinear antiferromagnetic structure in TbCoGa5. *Phys. Rev. B*. 2011, **84**, 214403.
80. GILES, C., ADRIANO, C., FARIA, G. A., MARDEGAN, J. R. and PAGLIUSO, P. G. Multiple Antiferromagnetic structures in HoCoGa5 studied by X-ray resonant magnetic scattering. poster at SCES 2011 conference. 2011.
81. GRANADO, E., PAGLIUSO, P. G., GILES, C., LORA-SERRANO, R., YOKAICHIYA, F. and SARRAO, J. L. Magnetic structure and fluctuations of Gd2IrIn8: A resonant x-ray diffraction study. *Phys. Rev. B*. American Physical Society, 2004, **69**, 144411.
82. ADRIANO, C. et al. Magnetic structure of Sm2IrIn8 determined by x-ray resonant magnetic scattering. *American Physical Society*. 2007, **76**, 104515.
83. MARDEGAN, J. R. L., ADRIANO, C., VESCOVI, R. F. C., FARIA, G. A., PAGLIUSO, P. G. and GILES, C. Magnetic structure of R2CoGa8 (R = Gd, Tb, and Dy): Structural tuning of magnetic properties in …. *Phys. Rev. B*. American Physical Society, 2014, **89**, 115103. Available online: http://link.aps.org/doi/10.1103/PhysRevB.89.115103
84. METOKI, N. et al. Phonons in UCoGa5. *Physica B*. 2006, **378–380**, 1003-04. Available online: http://www.sciencedirect.com/science/article/pii/S0921452606004662
85. PIEKARZ, P., PARLINSKI, K., JOCHYM, P. T., OLES, A. M., SANCHEZ, J.P. and REBIZANT, J. First-principles study of phonon modes in PuCoGa5

superconductor. *Phys. Rev. B*. 2005, **72**, 014521. Available online: http://link.aps.org/doi/10.1103/PhysRevB.72.014521

86. MALINOWSKI, A., HUNDLEY, M. F., MORENO, N. O., PAGLIUSO, P. G., SARRAO, J. L. and THOMPSON, J. D. Thermal expansion and magnetovolume effects in the heavy-fermion system Ce2RhIn8. *Phys. Rev. B*. 2003, **68**, 184419. Available online: http://link.aps.org/doi/10.1103/PhysRevB.68.184419
87. KACZOROWSKI, D., PIKUL, A., BELAN, B., SOJKA, L. and KALYCHAK, Y. Non-Fermi liquid behavior in polycrystalline Ce2PdIn8. *Physica B*. 2009, **404**, 2975 - 2977. Available online: http://www.sciencedirect.com/science/article/pii/S0921452609005195
88. LASHLEY, J. C. et al. Critical examination of heat capacity measurements made on a Quantum Design physical property …. *Cryogenics*. 2003, **43**, 369 - 378. Available online: http://www.sciencedirect.com/science/article/pii/S0011227503000924
89. MACALUSO, R. T. et al. Single-Crystal Growth of Ln2MIn8 (Ln = La, Ce; M = Rh, Ir): Implications for the Heavy-Fermion …. *Chem. Mater*. 2003, **15**, 1394-98.
90. OHARA, S., SAKAMOTO, I., SHOMI, T. and CHEN, G. Magnetic and Transport Properties of R2MIn8 (R=La,Ce Pr; M=Rh, Ir). *Acta Phys. Pol. B*. 2003, **34**, 1243.
91. SKOURSKI, Y., KUZMIN, M. D., SKOKOV, K. P., ANDREEV, A. V. and WOSNITZA, J. High-field magnetization of Ho2Fe17. *Phys. Rev. B*. 2011, **83**, 214420. Available online: http://link.aps.org/doi/10.1103/PhysRevB.83.214420
92. JOSHI, D. A., NAGALAKSHMI, R., DHAR, S. K. and THAMIZHAVEL, A. Anisotropic magnetization studies of R2CoGa8 single crystals (R=Gd, Tb, Dy, Ho, Er, Tm, Y, and Lu). *Phys. Rev. B*. 2008, **77**, 174420.
93. HIEU, N. V. et al. Magnetic Properties and Crystalline Electric Field Scheme in RRhIn5 (R: Rare Earth). *J. Phys. Soc. Jpn.* The Physical Society of Japan, 2007, **76**, 064702.
94. HIEU, N. V. et al. Unique Magnetic Properties of NdRhIn5, TbRhIn5, DyRhIn5, and HoRhIn5. *J. Phys. Soc. Jpn*. 2006, **75**, 074708.
95. UHLÍŘOVÁ, K., PROKLEŠKA, J. and SECHOVSKÝ, V. Comment on 'Emergence of a Superconducting State from an Antiferromagnetic Phase in Single Crystals …. *Phys. Rev. Lett*. 2010, **104**, 059701. Available online: http://link.aps.org/doi/10.1103/PhysRevLett.104.059701
96. CZOPNIK, A., MÄDGE, H. and STALIńSKI, B. Specific Heat of HoIn3, and ErIn3 Compounds. *Phys. Status Solidi A*. 1986, **94**, K13-16. Available online: http://dx.doi.org/10.1002/pssa.2210940161
97. LIN, H., REBELSKY, L., COLLINS, M. F., GARRETT, J. D. and BUYERS, W. J. L. Magnetic structure of UNi2Si2. *Phys. Rev. B*. 1991, **43**, 13232-39. Available online: http://link.aps.org/doi/10.1103/PhysRevB.43.13232
98. HONDA, F., METOKI, N., MATSUDA, T. D., HAGA, Y. and ĹŚNUKI, Y. Long-period, longitudinal spin density modulation in an itinerant 5f magnetic compound UCu2Si2. *J. Phys.: Condens. Matter*. 2006, **18**, 479. Available online: http://stacks.iop.org/0953-8984/18/i=2/a=010
99. JAVORSKÝ, P., PAJSKR, K., KLICPERA, M., ČERMÁK, P., SKOURSKI,

Y. and ANDREEV, A. V. High-field magnetization and magnetic phase diagrams in Nd2RhIn8 and Tb2RhIn8. *J. Alloys Compd*. 2014, **598**, 278 - 281. Available online: http://www.sciencedirect.com/science/article/pii/S0925838814003703

100. IWATA, N., HONDA, K., SHIGEOKA, T., HASHIMOTO, Y. and FUJII, H. Metamagnetism in DyCo2Si2. *J. Magn. Magn. Mater*. 1990, **90â€“91**, 63-64. Available online: http://www.sciencedirect.com/science/article/pii/S0304885310800228
101. VINOKUROVA, L., IVANOV, V. and SZYTULA, A. Magnetic phase diagrams of TbCo2Si2, DyCo2Si2, TbCo2Ge2 and DyCo2Ge2. *J. Alloys Compd*. 1992, **190**, L23 - L24. Available online: http://www.sciencedirect.com/science/article/pii/0925838892901623
102. BERTAUT, E. F. Representation analysis of magnetic structures. *Acta Cryst*. 1968, **24**, 217-31.
103. BJÖRKMAN, T. et al. Theoretical studies of the incommensurate magnetic structure of a heavy fermion system: CeRhIn5. *Phys. Rev. B*. 2010, **81**, 094433. Available online: http://link.aps.org/doi/10.1103/PhysRevB.81.094433
104. SZYTULA, A. and LECIEJEWICZ, J. *Handbook of Crystal Structures and Magnetic Properties of Rare Earth Intermetallics*. Taylor & Francis, 1994. ISBN 9780849342615. Available online: http://books.google.de/books?id=-tgM8oAQcdcC
105. IZYUMOV, Y. A., NAISH, V. E. and PETROV, S. B. Symmetry analysis in neutron diffraction studies of magnetic structures. 4: Theoretical group …. *J. Magn. Magn. Mater*. 1979, **13**, 275-82.

List of Tables

List of Abbreviations

“13”	compounds with $R\mathrm{In}_3$ structure
“115”	compounds with RTX_5 structure
“218”	compounds with R_2TX_8 structure
AF	antiferromagnetic
a, b, c	crystallographic directions
C	commensurate
F	structure factor
G	de Gennes factor
g_L	Landé factor
h,k,l	crystallographic indices in reciprocal space
IC	incommensurate
$irrep$	irreducible representation
J	total angular momentum
L	total orbital momentum
n	number of atoms in unit cell
PSD	position sensitive detector
$\mathbb{Q}$	set of rational numbers
$\mathbb{R}$	set of real numbers
R	rare-earth element
S	total spin momentum
T	transition metal
X	In or Ga
Z	atomic number
α	linear absorption coefficient
λ	wavelength of used neutron beam
μ_{ORD}	ordered moment
μ_{eff}	effective moment

Appendices

1. Python script for refinement of Er$_2$RhIn$_8$ compound

```
# -*- coding: utf-8 -*-
"""
Created on Tue Nov 12 16:10:08 2013

@author: Petr Cermak
"""

from ufit.lab import *
import matplotlib.pyplot as plt
from ufit.gui import start_fitter
from ufit.plotting import DataPlotter
#input datafiles
numors_nuclear = '71139-71200'
hklList_nuclear = [
['-2 -2 -4', -174.719, ''],
['-2 -2 -3', -163.24, ''],
#...
]

numors_magnetic = '71082-71138'
hklList_magnetic = [
['-1.5 -1.5 -4.5', -174.051, ''],
['-1.5 -1.5 -3.5', -162.736, ''],
#...
]

set_datatemplate('..\data\%06d')

def fitPeaks(nazev, d, hklList, intIndexes = False, offset = 0, ident='peak'):
    # fit the model, then print and plot all the results
    print nazev
    print "h\tk\tl\tstt\tint\tcorint\tTemp"
    i = 0
    results = []
    for dset in d:
        ax = subplot(1,1,1)
        #parse reflection list
        ok = False
        if isinstance(hklList[i], basestring):
            center_peak = float(dset.meta['info'].split()[2].strip(','))
            stt = - dset.meta['A4']
            Q = hklList[i].split(' ')
            option = ''
        else:
            Q = hklList[i][0].split(' ')
            center_peak = float(dset.meta['info'].split()[2])
            stt =- dset.meta['A4']
            option = hklList[i][2]
            try:
                ok = hklList[i][2] == 'ok'
            except:
                pass

        #set starting fitting values
        mainampl = max(dset['y'])
        model = Background(bkgd=0)
        all_fwhm = limited(0.2, 0.5, 0.3) #0.3
        if option == 'p':
            model = Parabola(x0=0, y0=0, stretch=1)
        if option == 'l':
            model = SlopingBackground(bkgd=0, slope=0)
        if option == 'low':  #low intensity
            all_fwhm = limited(0.2, 0.4, 0.3)
        model += \
            Gauss('peak1', pos=limited(center_peak-2,center_peak+1.5,center_peak+offset),
ampl=mainampl, fwhm=all_fwhm)
        #fit
        result = model.fit(dset)
```

```
        intensity = 0
        e = 0
        for peak in ['peak1']:
            intnow = result.paramvalues[peak + '_ampl'] * result.paramvalues[peak + '_fwhm']
            e1 = result.paramerrors[peak + '_ampl'] / result.paramvalues[peak + '_ampl']
            e2 = result.paramerrors[peak + '_fwhm'] / result.paramvalues[peak + '_fwhm']
            e += intnow * sqrt(e1**2 + e2**2)
            intensity += intnow

        while '' in Q:
            Q.remove('')
        #Lorentz correction
        icor = intensity * sin(radians(stt)) * 100000
        e *= 100000
        avgtemp = average(dset.meta['col_TRT'])
        #save results
        results.append([Q[0],Q[1],Q[2], stt,intensity,icor,e,avgtemp])
        i+=1
    return np.array(results)

#datared format
drformat = ['%6.2f','%6.2f','%6.2f','%10.4f','%10.4f']

#nuclear
res = fitPeaks('NUCLEAR REFLECTIONS',
         read_numors(numors_nuclear,0.05,ncol='M1'),
         hklList_nuclear,ident='nuc')
np.savetxt('datared/nuclear.col', res[:, [0,1,2,5,6]],
         fmt=drformat)
##magnetic
res = fitPeaks('MAGNETIC REFLECTIONS',
         read_numors(numors_magnetic,0.05,ncol='M1'),
         hklList_magnetic,ident='mag')
np.savetxt('datared/magnetic.col', res[:, [0,1,2,5,6]],
         fmt=drformat)
```

2. Python script for refinement of Ho_2RhIn_8 compound

```
from h5py import h5f
import h5py
print('Ho2RhIn8 evaluation start')

import os
import numpy as np
import matplotlib as ml
import matplotlib.pyplot as plt
import collections

from ufit.lab import *
from ufit.gui import start_fitter
from ufit.plotting import DataPlotter

dir = os.path.join(os.path.dirname(__file__), '..\..\data')
from nexpy.api import nexus

#datared format
drformat = ['%6.2f','%6.2f','%6.2f','%10.4f','%10.4f']

#read peaklist
pl = np.loadtxt(os.path.join(dir, "peaklist.txt"))
peaklist = {}
for p in pl:
    peaklist[p[0]] = [p[1], p[2], p[3]]

opt = { 65244: 's', 65255: 's', 65266: 's'}

def LoadFile(numor, subdir = "horizontal"):
    path = os.path.join(dir, subdir, '%06d.nxs' % numor)
    a=nexus.load(path)
    #print a.tree
    d = E4Data()
    d.params = a.entry1.data1.PARAMETERS.nxdata
    d.data     = a.entry1.data1.DATA.nxdata
```

```
    if a.entry1.data1.Z.nxdata.ndim > 1:
        d.MON      = a.entry1.data1.Z.nxdata[:,2]
        d.OMEGA    = a.entry1.data1.Z.nxdata[:,3]
        d.TT       = a.entry1.data1.Z.nxdata[:,4]
        d.T_REG    = a.entry1.data1.Z.nxdata[:,5]
        d.T_SAMPLE = a.entry1.data1.Z.nxdata[:,6]
        d.TIME     = a.entry1.data1.Z.nxdata[:,10]
        d.CTS      = a.entry1.data1.Z.nxdata[:,11]
    else:
        zdata = np.loadtxt(os.path.join(dir, subdir, '%06d.as_' % numor))
        d.MON      = zdata[:,2]
        d.OMEGA    = zdata[:,1]
        d.TT       = zdata[:,3]
        d.T_REG    = zdata[:,4]
        d.T_SAMPLE = zdata[:,5]
        d.TIME     = zdata[:,10]
        d.CTS      = zdata[:,11]
    return d

def ShowMap(plotdata,title = 'test',fname = 'tmp.png'):
    fig = plt.figure(figsize=(6, 3.2))
    ax = fig.add_subplot(111)
    ax.set_title(title)
    plt.imshow(plotdata)
    ax.set_aspect('equal')
    cax = fig.add_axes([0.12, 0.1, 0.78, 0.8])
    cax.get_xaxis().set_visible(False)
    cax.get_yaxis().set_visible(False)
    cax.patch.set_alpha(0)
    cax.set_frame_on(False)
    plt.colorbar(orientation='vertical')
    fig1 = plt.gcf()
    if showplots:
        plt.show()
    if savefigs:
        fig1.savefig(fname, dpi=300)
    plt.close()

def SimplyShowMyPlot(plotdata, xaxis = '', yaxis = '', title = 'test', fname = 'tmp.png', xmin = 0,
xmax = None):
    if xmax == None:
        xmax = len(plotdata) - 1
    plt.plot(plotdata)
    plt.ylabel(yaxis)
    plt.xlabel(xaxis)
    plt.title(title)
    plt.axis([xmin,xmax,0,np.max(plotdata)])
    fig1 = plt.gcf()
    if showplots:
        plt.show()
    if savefigs:
        fig1.savefig(fname)
    plt.close()

def FitPeak(numor, ydata, xdata, yerr = None, stt = None, t_sample = 0, intIndexes = False, pre = '',
center_peak = None):
    print "fitting #%06d with pre = %s" % (numor, pre)
    warning = 0
    if stt == None:
        assert("two theta must be passed")
    if yerr == None:
        yerr = sqrt(ydata)
    try:
        Q = peaklist[numor]
    except:
        print "WARNING, Q values for numor %06d not found" % numor
        Q = [0,0,0]
    try:
        option = opt[numor]
    except:
        option = ''
    if center_peak == None:
        center_peak = np.average(xdata)
```

```
    dset = as_data(xdata,ydata,yerr)

    mainampl = max(dset['y'])
    model = Background('bg', bkgd=0)
    all_fwhm = limited(0.2, 1.5, 0.3) #0.3
    if option == 'p':
        model = Parabola(x0=0, y0=0, stretch=1)
    if option == 's':
        model = SlopingBackground('bg',bkgd=0, slope=0)
    if option == 'low':  #low intensity
        all_fwhm = limited(0.2, 0.4, 0.3)
    ppos = limited(center_peak-2.5,center_peak+2.5,center_peak)
    #all_fwhm = 0.2
    #ppos = center_peak
    model += \
        Gauss('peak1', pos=ppos,
             ampl=mainampl, fwhm=all_fwhm)
    result = model.fit(dset)
    if any(result.paramerrors.values()) == 0:
        model = Background('bg', bkgd=0)
        all_fwhm = 0.2
        ppos = center_peak
        model += \
            Gauss('peak1', pos=ppos,
                 ampl=mainampl, fwhm=all_fwhm)
        result = model.fit(dset)
        print "fitting again # %06d without limits" % numor
        warning += 1
    intensity = 0
    e = 0
    for peak in ['peak1']:
        intnow = result.paramvalues[peak + '_ampl'] * result.paramvalues[peak + '_fwhm']
        e1 = result.paramerrors[peak + '_ampl'] / result.paramvalues[peak + '_ampl']
        e2 = result.paramerrors[peak + '_fwhm'] / result.paramvalues[peak + '_fwhm']
        e += intnow * sqrt(e1**2 + e2**2)
        intensity += intnow

    coeff = 1 # coefficient to multiply intensity to have nice numbers
    # lorent factor correction
    icor = intensity * sin(radians(stt)) * coeff
    e *= coeff
    avgtemp = t_sample

    #print out fit
    if intIndexes:
        Q = [ int(x) for x in Q ]
    else:
        Q = [ float(x) for x in Q ]

    if showplots or savefigs:
        ax = subplot(1,1,1)
        ax.set_title(Q)
        result.plotfull(ax)
        fig1 = plt.gcf()
        if showplots:
            plt.show()
        if savefigs:
            fig1.savefig('fits/%s%06d.png' % (pre, i), dpi=300)
        plt.close()

    return [numor,Q[0],Q[1],Q[2], stt,intensity,icor,e,avgtemp,
            result.paramvalues['peak1_ampl'], result.paramerrors['peak1_ampl'],
            result.paramvalues['peak1_fwhm'], result.paramerrors['peak1_fwhm'],
            center_peak - result.paramvalues['peak1_pos'], result.paramerrors['peak1_pos'],
            result.paramvalues['bg_bkgd'],result.paramerrors['bg_bkgd'],warning]

def doSumation(myrange, typeext = "all", typdir = "HOR", mydirection = 'horizontal', xfromto = None,
yfromto = None):
    summed = np.zeros([256,256])
    for i in myrange:
        d = LoadFile(i, subdir = mydirection)
        print "%06d summed" % i
        summed += np.sum(d.data,0)
```

```
    if xfromto != None:
        summed = summed[:,xfromto[0]:xfromto[1]]
    if yfromto != None:
        summed = summed[yfromto[0]:yfromto[1],:]
    datashow1 = np.sum(summed,0)
    datashow2 = np.sum(summed,1)

    np.savetxt("B-%s-%s-detectors-summed.dat" % (typdir, typeext), summed)
    np.savetxt("B-%s-%s-detectors-summed-xmerge.dat" % (typdir, typeext), datashow1)
    np.savetxt("B-%s-%s-detectors-summed-ymerge.dat" % (typdir, typeext), datashow2)

class E4Data:
    params = ""
    data = []

    OMEGA = []
    TT = []
    MON = []
    TIME = []
    CTS = []
    T_REG = []
    T_SAMPLE = []


first_sum = True
fit_horizontal = True

#             xfrom,xt,yfrom,yto
hor_r =           ( 90,166, 80,166)
ver_r_sp =        ( 90,180, 80,160)
ver_r_sp_magdep = (110,156, 80,150)
ver_r_out =       (110,156,180,250)

horizontal_range = [65156] + range(65158, 65195) + range(65198, 65351) + range(65355, 65413)
if first_sum:
    doSumation(horizontal_range)

if fit_horizontal:
    results = []
    for i in horizontal_range:
        d = LoadFile(i)
        toplot = d.data[:,hor_r[2]:hor_r[3],hor_r[0]:hor_r[1]]
        #show projection of the peak for summation
        ShowMap(np.sum(toplot,0),'test','fits\\HOR\\PREV-%d06.png' % i)
        if np.max(d.TT) != np.min(d.TT):
            assert("different two theta during scan!")

        res = FitPeak(i, np.sum(np.sum(toplot,1),1), d.OMEGA, stt = np.max(d.TT), t_sample =
np.average(d.T_SAMPLE), pre="HOR\\")
        results.append(res)

    results = np.array(results)
    #save all info
    np.savetxt('fitting_output_horizontal.txt', results,
header="numor\th\tk\tl\tstt\tint\tcorint\tdint\ttemp\tampl\tdampl\tfwhm\tdfwhm\toffset\tdoffset\tbg\tdb
g\tremark", delimiter="\t", comments = "")
    #export for datared
    aa = results[:, [1,2,3,6,7]]
    np.savetxt('datared/test.col', aa, fmt=drformat)

nucrange_nofield = range(67850, 67853) + [67854,
    67855,67857,67858,67860,67862,67863,67866,67867,67871,
    67873,67875,67876,67878,67880,67882]
magrange_nofield = range(67886, 67947)
magrange_field = range(67947, 67965)
nucrange_field = [67965,67966,67967,67969,
    67970,67972,67973,67975,67977,67978,67981,67982,
    67986,67988,67990,67991,67993,67995,67997]
magdeprange = range(68001,68043)
```